Final Technical Report

Award Number	:	DE-FC03-02SF22636
Research Title	:	Energy Partitioning for Seismic Events in Fennoscandia and NW Russia
Submitted by	:	Stiftelsen NORSAR
Principal Investigator	:	Hilmar Bungum
Reporting Period	:	30 September 2002 - 31 January 2006
Date of Report	:	31 January 2006

NORSAR Contribution No. 967

Table of Contents

Contributors

The contributors to this report are:

Hilmar Bungum, NORSAR
Tormod Kværna, NORSAR
Shawn Larsen, LLNL
Nils Maercklin, NORSAR
Michael Roth, NORSAR
Volker Oye, NORSAR
Johannes Schweitzer, NORSAR
Svein Mykkeltveit, NORSAR
David B. Harris, LLNL

We thank Katja Sahala, Ilpo Mäkinen, and Timo Mäki, INMET Mining, and Errol de Kock, Integrated Seismic Systems (ISS), for access to Pyhäsalmi mine data and for generous support and assistance in this connection.

Executive Summary

In this project we have addressed the problem of energy partitioning at distances ranging from very local to regional for various kinds of seismic sources. On the local and regional scale (20-220 km) we have targeted events from the region offshore Western Norway where we have both natural earthquake activity as well as frequent occurrence of underwater explosions carried out by the Norwegian Navy.

On the small scale we have focused on analysis of observations from an in-mine network of 16-18 sensors in the Pyhäsalmi mine in central Finland. This analysis has been supplemented with 3-D finite difference wave propagation simulations in a realistic mine model to investigate the physical mechanisms that partition seismic energy in the near source region in and around the underground mine.

The results from modeling and analysis of local and regional data show that mean S/P amplitude ratios for explosions and natural events differ at individual stations and are in general higher for natural events and frequency bands above 3 Hz. However, the distributions of S/P ratios for explosions and natural events overlap in all analyzed frequency bands. Thus, for individual events in our study area, S/P amplitude ratios can only assist the discrimination between an explosion or a natural event.

This observation is supported by synthetic seismograms calculated for simple 1-D models which demonstrate that explosions also generate shear-wave energy if they are fired close to an interface with a strong material contrast (as is the case for most explosions), e.g., free surface or the ocean bottom. The larger difference in S/P ratios between earthquakes and explosions for higher frequencies can be explained by the fact that at low frequencies (larger wavelengths), discontinuities and structural heterogeneities in the explosion source region are stronger generators of converted S energy. The S*-phase, for example, is most efficiently generated whenever an explosion source is located close (within one wavelength) to a strong discontinuity.

Source parameters of mining induced events in the Pyhäsalmi mine follow generally the $M_0 \sim f_c^{-3}$ source scaling relation. Stress drops related to the Brune source model range from about 0.01 to 1.0 MPa. Q estimates from the data vary between about 200 and 800, what is most likely related to the complexity of the mine (voids and tunnels). Analyzing the data with the Multiple Empirical Greens Function (MEGF) approach, attenuation corrections suggest increasing Q with increasing frequency. Energy-to-moment ratios based on the MEGF approach seem constant compared to slightly increasing energy-to-moment ratios based on constant Q models. Comparing our results with results from other studies, covering seismic moments over 11 orders of magnitude, the energy-to-moment ratios seem to increase with increasing magnitudes, i.e. following a modified $M_0 \sim f_c^{-(3+\varepsilon)}$ scaling relation with ε about 0.5.

High-frequency (50-400 Hz) S/P ratios for mine blasts (explosions) and rockbursts recorded at the Pyhäsalmi in-mine network do not show any significant dependency on the distance to the events. However, we have been unable to obtain information on the distance dependency of the S/P ratios within the first tens of meters from the source.

The Pyhäsalmi explosions have generally lower S/P ratios than the rockbursts for all frequencies, but the difference is far too small to be significant for classification purposes. The maxima for the explosion distributions are all below 2, whereas they are all above 2 for the rockbursts. The rockbursts also have a wider distribution of S/P ratios, which can be explained by the variability of the radiation patterns from the rockburst sources. S/P ratios for explosions and rockbursts located in the same small area of the mine show results very similar to those for the full data set. This indicates that the observed differences in S/P ratios between explosions and rockbursts are due to differences in the source characteristics, and not due to propagation effects along paths in the mine.

3-D finite-difference simulations were used to model seismic events within the Pyhäsalmi mine. In particular, a January 26, 2003 rockburst was modeled at frequencies of 50 Hz (4 meter grid) and 100 Hz (2 meter grid). We were able to match the characteristics of the observed data at 50 Hz particularly well, and the characteristics of the 100 Hz data reasonably well. These results help validate the 3-D geologic mine model and the reliability of our simulations.

The simulations showed that significant shear-energy can be produced due to the geologic and structural heterogeneities within the mine. In fact, mode-converted shear-energy generated from mine heterogeneity can dominate the compressional energy from an explosive source. A strong correlation is observed between the distance of a source from a mine heterogeneity and the magnitude of generated shear-energy. The ratio of shear to compressional energy is about a factor of two larger when the source is located within one wavelength from a mine heterogeneity. The simulations also suggest that excavated mine volumes are significantly stronger contributors to shear-energy generation than geologic heterogeneities. However, the simulations reveal that the magnitude of shear-energy generated as part of a shear-producing source mechanism (e.g., rockburst, mine collapse) can be as large or larger than that caused by heterogeneity within the mine.

1 Introduction

The main objective of this project has been to increase the (nuclear) explosion monitoring effectiveness through improved understanding of basic earthquake and explosion phenomenology. What this entails is detailed characterization and understanding of how the seismic energy is generated from these phenomena (including simple and complex explosions, rockbursts, i.e. stress release in mines, and ordinary tectonic earthquakes, all at different depths and in different geological environments) and how this energy is partitioned between P and S waves. Specific questions are:

- How is the generation and partitioning of seismic energy affected by properties such as source region medium and overburden, the local structure, and the surrounding tectonic structure?
- What are the significant measurable effects of the partitioning of the seismic energy into various regional P and S phases, especially at higher frequencies?
- What is the physical basis for a measurable property, such as magnitude, that can be directly related to the yield of a fully coupled explosion, and how can emplacement conditions affect the observations?

Generally, explosions occur very close to the Earth’s surface which is characterized by sharp discontinuities (free surface, ground water table, transition between unconsolidated sediments to solid rock, etc.). The interaction of a seismic source with such discontinuities can generate unexpected source radiation patterns and partitioning between P- and S-wave energy. Even in the simplest case of a homogeneous medium bounded by a free surface, an explosive source can generate different types of shear-wave energy if it is close (within one wavelength) to an interface with a strong impedance contrast, like the free surface or the ocean bottom (e.g., Roth and Holliger, 2000).

There is an ongoing discussion about the dominant P- to S- transfer mechanism. It is generally agreed that significant S-wave energy from explosions is generated in the near-source region; several such near-source energy excitation mechanisms have been investigated, including P-to-Lg scattering, pS-to-Lg conversion at the free surface, Rg-to-Lg coupling, S*-to-Lg conversion, spall excitation of S, tectonic release and rock damage. S* is a non-geometric wave generated by P-to-S conversion whenever an explosion source is located close (within one wavelength) to the free surface (Fertig, 1984).

Recently, Myers at al. (2005) analyzed recordings from the 1993 non-proliferation experiment (NPE) at the Nevada Test Site (NTS), accompanied with wavefield simulation in a detailed geological model of the area. They found that near-source topography and geological complexity in the upper crust strongly contributed to the S-waves from the NPE shot.

Xie et al. (2005) conducted numerical wavefield simulations for shallow explosions in media with 3-7% random velocity fluctuations. Their results show that S*-Lg scattering is stronger for low frequencies and shallow depths, whereas P-Lg scattering is stronger for high frequencies. 3D simulations showed considerable P-pS-SH or SV-SH generation with a 7% velocity and density perturbations. Tangential Lg energy from explosions are often observed as large as those observed on the vertical components (Stevens et al., 2003).

The so-called Arizona source phenomenology experiment (Bonner et al., 2005) showed that the designed test shots and mining explosions are good surrogates for nuclear explosions as the magnitude-and distance-corrected Pg/Lg amplitude ratios fall in the range of those for nuclear explosions at NTS. Differences in depth of burial and single versus multiple shots have only a small effect on the amplitude ratios.

Source array analysis of Semipalatinsk underground nuclear explosions (UNEs) recorded at the Borovoye station at a distance of 680 km show that Rg-to-S scattering does not appear to be a dominant mechanism for the Lg excitation from Semipalatinsk UNEs (Hong and Xie, 2005). The geology of the source region appears to play an important role on the strength of mantle shear-waves in the expected Sn window, where slower near-surface velocities in the source region seem to enhance shear-waves. Less dependency on source region geology is found for the Lg waves, which also have lower frequencies than Sn. The results from this study imply that the source region geology tends to make strong influence on the strength of higher-frequency shear-waves.

Scaling analysis of Sn/Pn and Lg/Pn spectral ratios at Borovoye for Semipalatinsk explosions (Murphy et al., 2005) indicate an Sn/Lg source generation mechanism compatible with a linear frequency independent conversion of direct P-wave energy from the explosions.

In order to estimate the effect of strong scatterers in the near-source region, Toksöz et al. (2005) conducted 3-D wavefield modeling in media with well-defined tunnels, chambers, shafts or surface topography. Their simulations show that a tunnel near an explosion acts as an amazingly strong scatterer, where P-to-S scattering is much stronger than P-to-P, and some energy is scattered into SH. A hill or a mesa above the explosion source causes strong scattering of the surface waves.

In this project we have further addressed the problem of energy partitioning at distances ranging from very local to regional for various kinds of seismic sources. On the local and regional scale (20-220 km) we have targeted events from the region offshore Western Norway where we have both natural earthquake activity as well as frequent occurrence of underwater explosions carried out by the Norwegian Navy. These results are presented in Section 2 of this report.

On the small scale we have focused on analysis of observations from an in-mine network of 16-18 sensors in the Pyhäsalmi mine in central Finland. This analysis has been supplemented with 3-D finite-difference wave propagation simulations in a realistic mine model to investigate the physical mechanisms that partition seismic energy in the near source region in and around the underground mine. Analysis of the in-mine data and modeling of the effects of the in-mine structures are presented in Sections 3 and 4.

2 Analysis and Modeling of Local and Regional Data

We have addressed the question of how seismic energy is partitioned between P and S waves at regional distances between 20 and 220 km. We have chosen to target events from the region offshore Western Norway where we have both natural earthquake activity and frequent occurrence of underwater explosions carried out by the Norwegian Navy. We show results from S/P amplitude ratio analysis of recordings in the distance range 20 to 200 km. Wavefield modeling of explosive and earthquake sources in different models with layered structures are conducted to form a basis for the discussion of the obtained results.

2.1 Energy Partitioning for Seismic Events near the Coast of Western Norway

Data Base

The data base for this study are seismic phase arrival times, source locations, and waveform data of natural events and underwater explosions recorded at seven selected three-component stations in Western Norway between 1997 and 2004 (Figure 1). The seismic stations are part of the permanent National Norwegian Seismic Network (NNSN), and the data were provided by the University of Bergen (UiB). The selected source region is located around 60N, 5E, where both event types, earthquakes and explosions, occur.

During the routine analysis at UiB all events are classified as one of four main classes: explosions (E), probable explosions (P), natural events (N), and unspecified events. Typically, the explosions are detonations in water and confirmed by or related to the Norwegian Navy (Haakonsvern). Coda magnitudes of all events are mainly in the range 1.0 < Mc < 2.3. Explosions usually occur at day time. A peak at day time in the temporal distribution of unspecified events suggests that many of these events are also explosions.

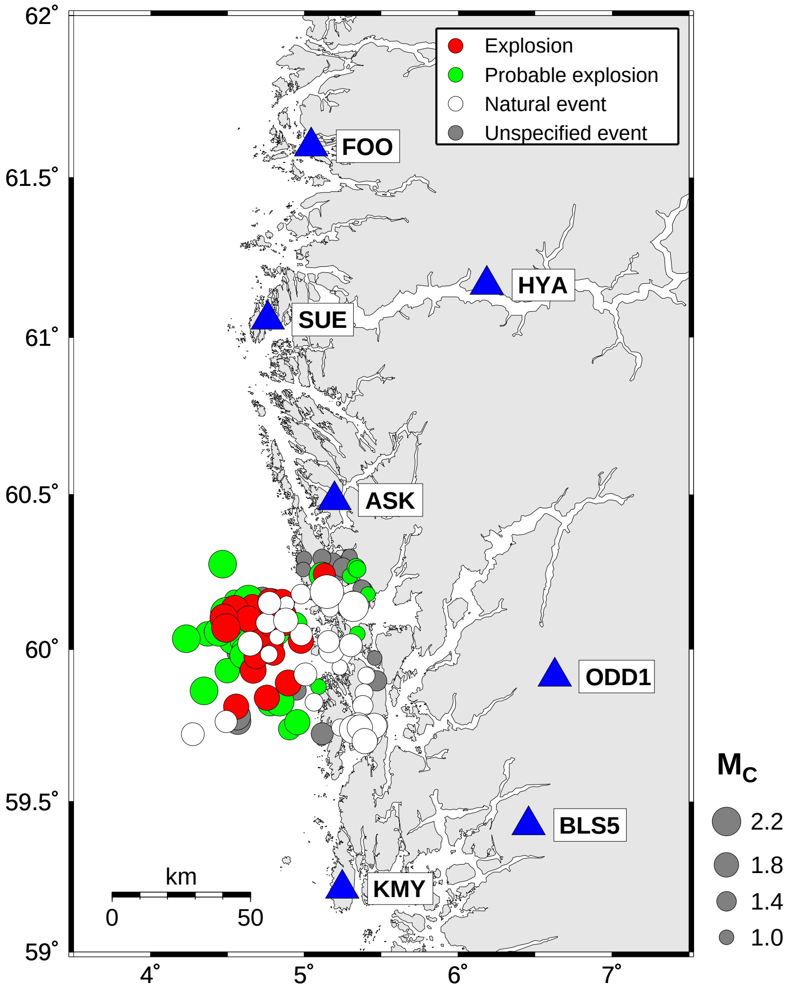

Figure 1. Seismic three-component short-period stations (triangles) and events used for this study: ASK = Askøy, BLS5 = Blåsjø, FOO = Florø, HYA = Høyanger, KMY = Karmøy, ODD1 = Odda, and SUE = Sulen.

Whereas the initial data base contains many confirmed explosions, only a few events in our source region are classified as natural earthquakes. Therefore, we analyzed signals and amplitude spectra of previously unspecified events in order to find more natural events for our study. The judgement was based on the fact that explosions in the water column are typically characterized by reverberations, which appear in amplitude spectra as distinct notches. Figure 2 shows vertical-component seismograms and spectra of four events, two explosions (left) and two known natural events (right). The more continuous shape of the spectra of the natural events is clearly visible. For our study we added the originally unspecified events to the set of natural ones if they showed a similar spectral behavior and no evidence of reverberations as seen in the examples on the left.

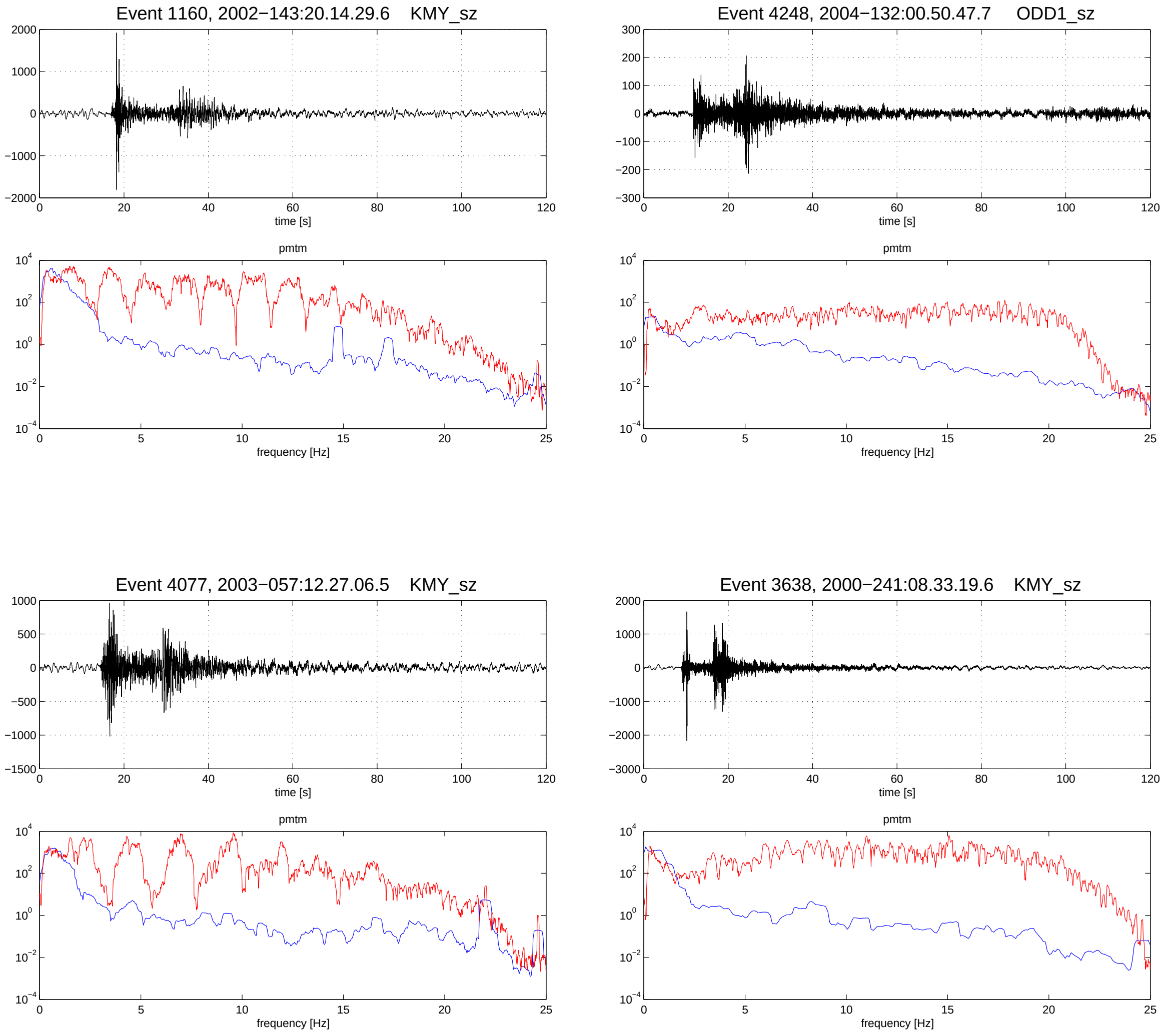

Figure 2. Vertical component seismograms and amplitude spectra of two explosions (left) and two natural events (right). Signal spectra (red) are calculated in a 60 s time window starting at the P onset and using the Thomson multitaper method, and for noise spectra (blue) the time windows covered the time period from the origin time to 2 s before P, which were the noise data segments available in the UiB database.

Explosions usually occur at day time, whereas the occurrence of natural events is not related to the time of the day. Figure 3 shows the time-of-day distribution for natural and unspecified events from the original UiB catalogue (a) and from our revised event list (b). The distribution for unspecified events in the revised list (b) has a peak at day time compared with the more uniform distribution for natural events. This suggests that at least some of the unspecified events are in fact explosions. The high occurrence rate of natural events in the early afternoon is caused by aftershocks of an earthquake on 12 August 2000 (see the event list in Appendix 1). For completeness, Figure 3c compares the time-of-day distribution of (confirmed) explosions and probable explosions from our revised event list, also given in Appendix 1.

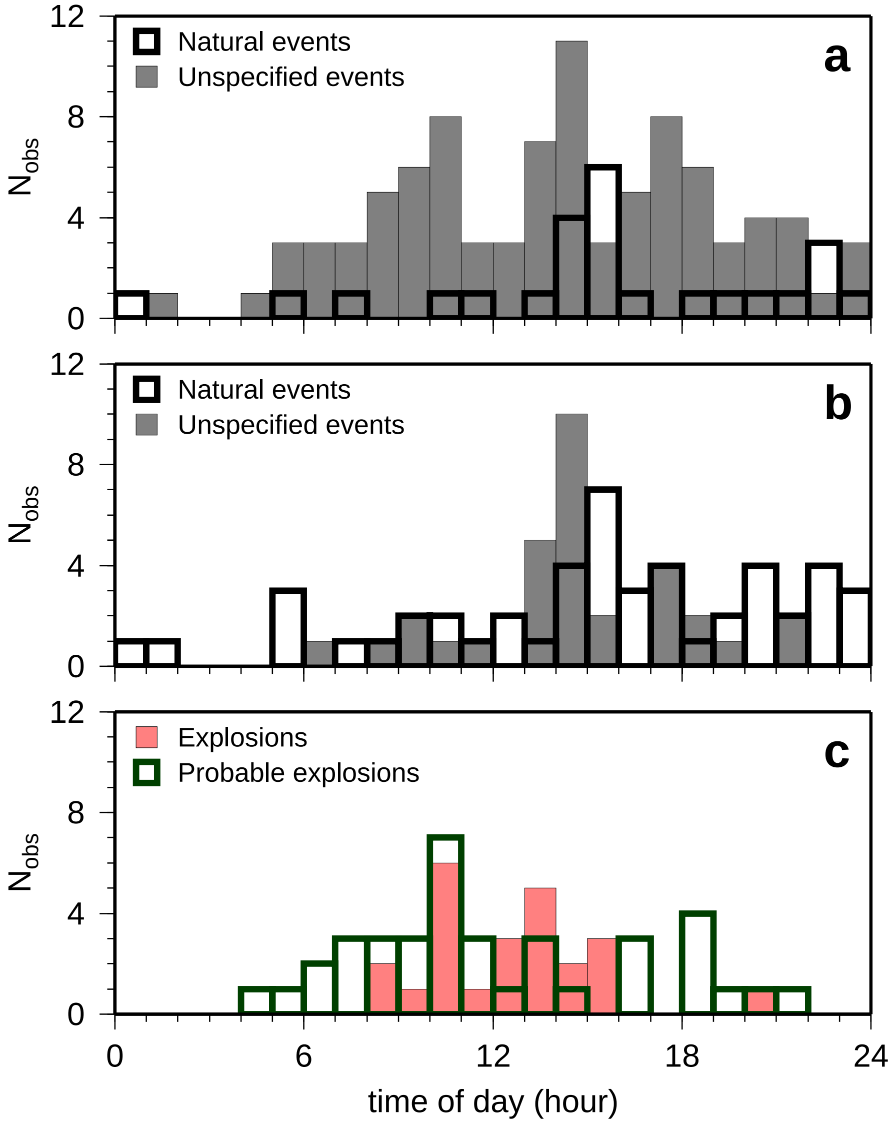

Figure 3. Time-of-day distribution of events. **a:** Natural and unspecified events from the original UiB catalogue, **b:** the same events after revision, and **c:** explosions and probable explosions (revised catalogue).

Data Analysis

The original three components recorded are vertical (Z), North-South (N), and East-West (E). To determine back-azimuth and incident angle of an incoming wave we applied a polarization analysis on data bandpass-filtered between 2 and 8 Hz. The analysis time window was always 3 s long starting at the P arrival time determined by UiB. In general, calculated back-azimuths deviate from theoretical (geometric) values by just a few degrees. With the calculated back-azimuths and incident angles the data are rotated into the ray coordinate system (L, Q, T) for subsequent processing and analysis. The incidence angles and back-azimuths calculated from the P phases may not be optimal for the S-waves, but we do not consider this to have any significant effect on the estimates of the S/P ratios.

Figure 4 shows bandpass-filtered (2-8 Hz) seismograms for two events recorded at two different stations, KMY (top) and SUE (bottom). The panels on the left show a confirmed explosion and those on the right a natural event. At the bottom of each panel are the original traces in the ZNE system, and on top the rotated ones (LQT). Here, differences in S/P amplitude ratios are clearly visible. Figure 5 shows seismograms for the same explosion as above in different frequency bands ranging from 1-2 Hz to 12-24 Hz. Each band is one octave wide. A trend to lower S/P amplitude ratios (higher P energy) can be observed for the higher frequency bands (top panels).

We measured S/P amplitude ratios for all four sets of events separately. In addition, noise amplitudes were measured in a time window preceding the P-phase. Only those events were analyzed that had signal-to-noise ratios larger than 3 for both P and S phases. A data set of 143 events remained after this quality control: 24 explosions, 38 probable explosions, 53 natural, and 28 unspecified events.

We chose nine 1 octave passbands to measure the S/P amplitudes. The passbands range from 0.5-1.0 to 12-24 Hz (see e.g. Figure 5). The P amplitude was taken to be the maximum amplitude on the L component in the time window from the P onset to 0.5 s before the S onset. The S amplitude was taken to be the maximum in the orthogonal QT plane (vector sum of the Q and T components) in a 10 s time window starting at the S onset.

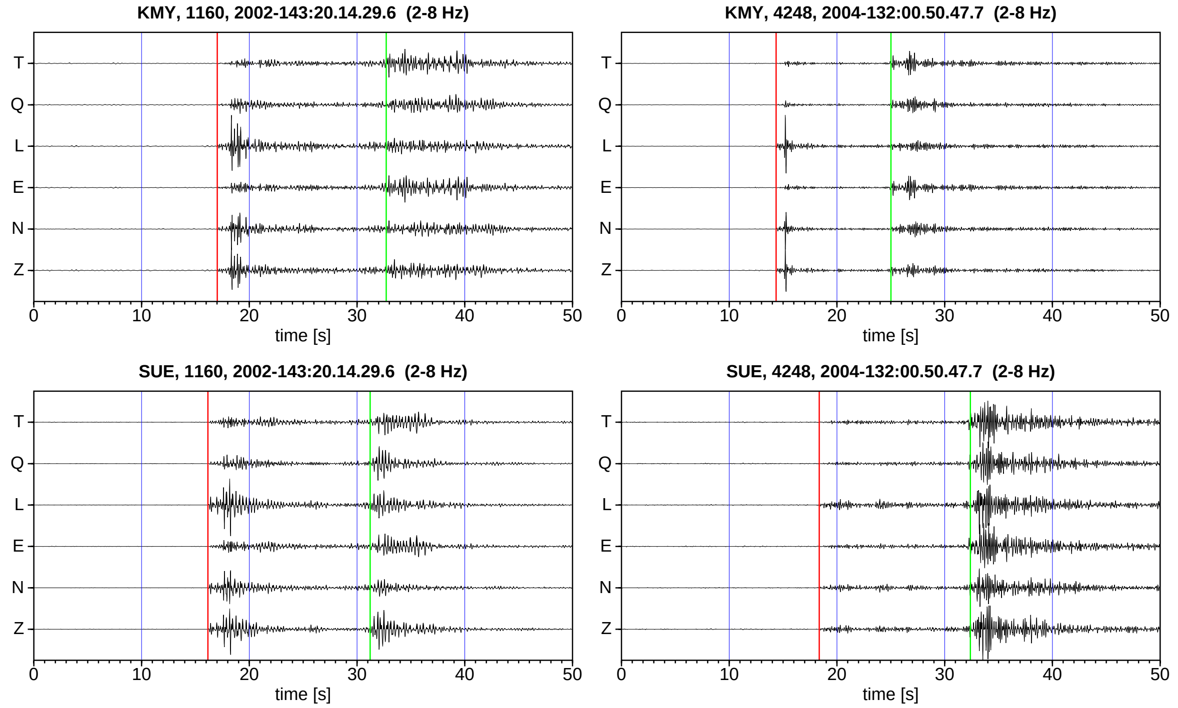

Figure 4. Three-component seismograms (2-8 Hz) recorded at the two stations KMY and SUE (see Figure 1). The time axis is relative to the origin time given on top of each panel, and red and green lines indicate the P and S onsets, respectively. Left: confirmed navy explosion (Haakonsvern), and right: natural event. The traces are scaled relative to the maximum amplitude of each panel, respectively

Results

Figure 6 shows the distribution (histograms) of S/P amplitude ratios for all the explosions (red) and natural events (black outline) recorded at all seven stations. The abscissa (S/P ratios) is logarithmic, i.e. positive values indicate higher S than P amplitudes. The histograms for explosions exhibit a clear trend to lower S/P amplitude ratios (higher P energy) with increasing frequency, whereas the values for natural events cover a wider range and do not show such a trend.

Examples for S/P amplitude ratios as a function of source-receiver distance are given in Figure 7 for all events recorded at selected stations (ASK, KMY, ODD1, and FOO; see Figure 1). At station ASK, the closest station to the source region, S/P ratios for natural events (open circles) generally seems to be lower than those for explosions (red). In contrast to this observation, at all other, more distant stations differences in (average) S/P ratios are visible only in selected frequency bands. Additionally, in case of significant differences between the two event types, S/P ratios for natural events are often higher than for explosions, e.g. at KMY (3-6 and 4-8 Hz) and ODD1 (6-12 Hz and higher). However, the scatter of observed S/P ratios at a certain distance is large for both types of events, and a general relationship between S/P ratios and distance cannot be established from these plots.

Figure 8 illustrates S/P ratio variations with distance for individual events, two explosions (top panels) and two natural events (bottom panels). Again, the average S/P ratios for explosions are generally lower than for natural events, but the ratios for both event classes exhibit a large variance.

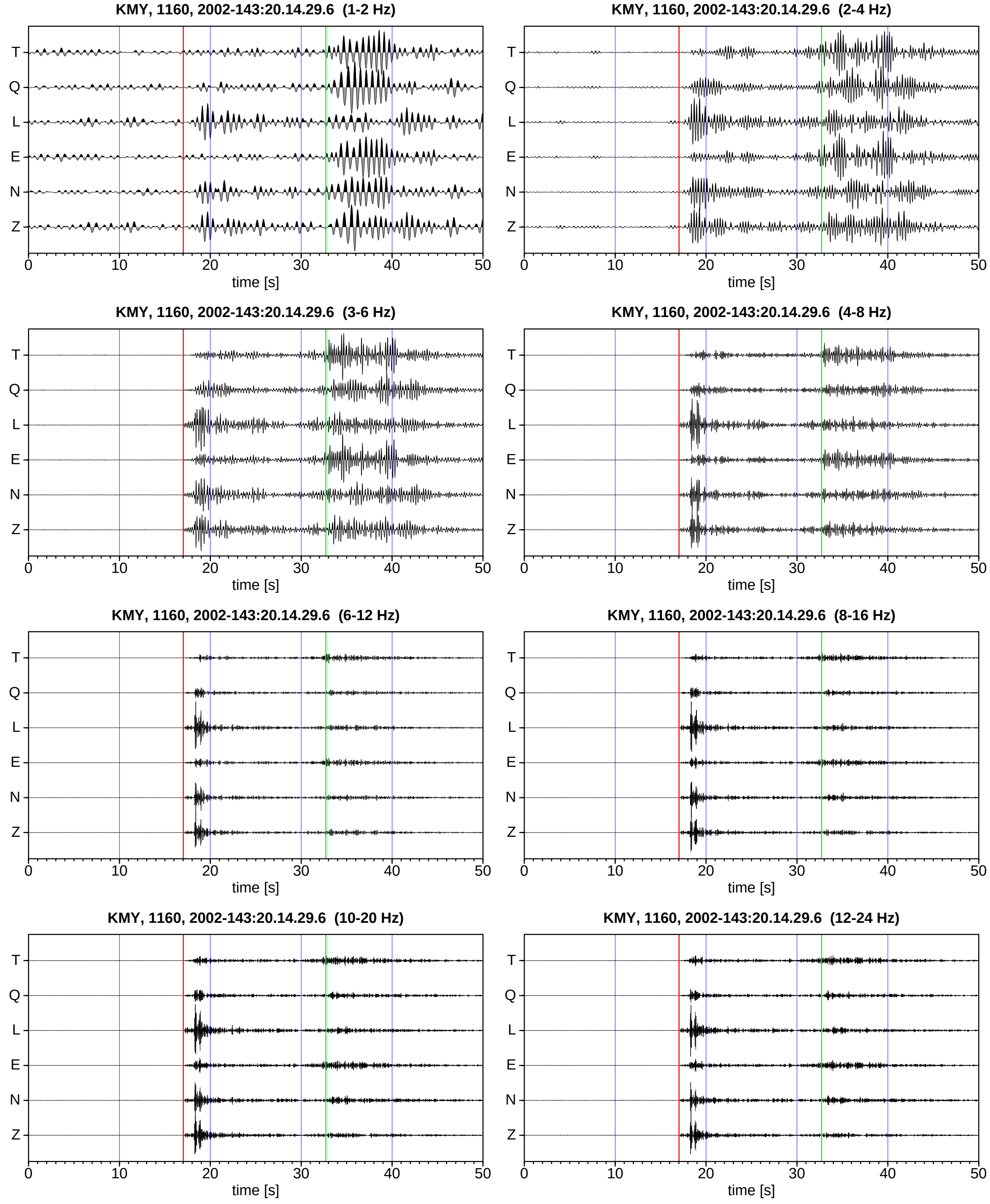
KMY, 1160, 2002-143:20.14.29.6 (1-2 Hz)

KMY, 1160, 2002-143:20.14.29.6 (2-4 Hz)

KMY, 1160, 2002-143:20.14.29.6 (3-6 Hz)

KMY, 1160, 2002-143:20.14.29.6 (4-8 Hz)

KMY, 1160, 2002-143:20.14.29.6 (6-12 Hz)

KMY, 1160, 2002-143:20.14.29.6 (8-16 Hz)

KMY, 1160, 2002-143:20.14.29.6 (10-20 Hz)

KMY, 1160, 2002-143:20.14.29.6 (12-24 Hz)

Figure 5. Three-component seismograms in different frequency bands of a confirmed explosion recorded at the station KMY (see Figure 1). The time axis is relative to the origin time given on top of each panel, and red and green lines. The traces are scaled relative to the maximum amplitude of each panel, respectively

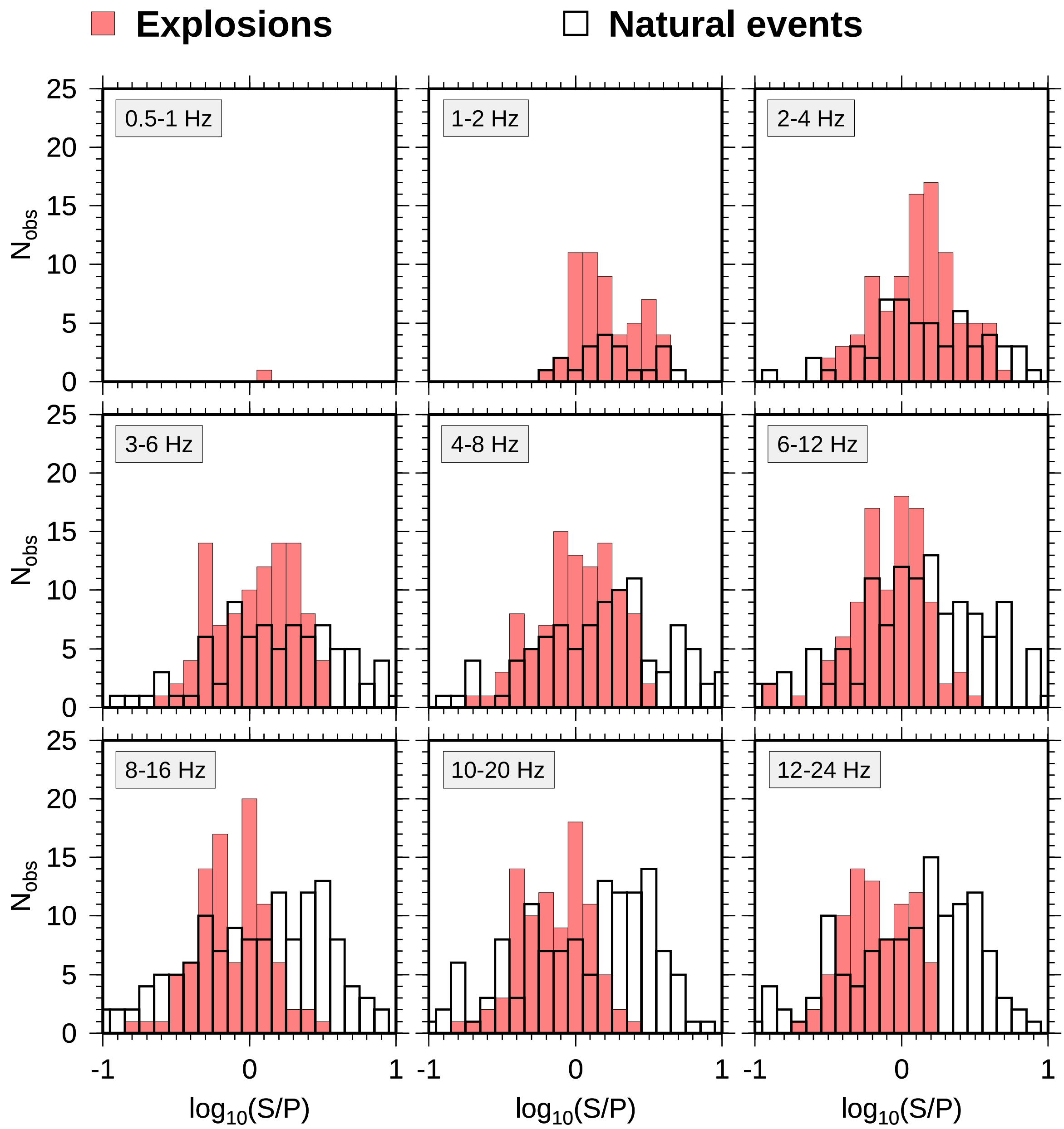

Figure 6. Histograms of S/P amplitude ratios (logarithm) for all explosions (red) and natural events (black outline).

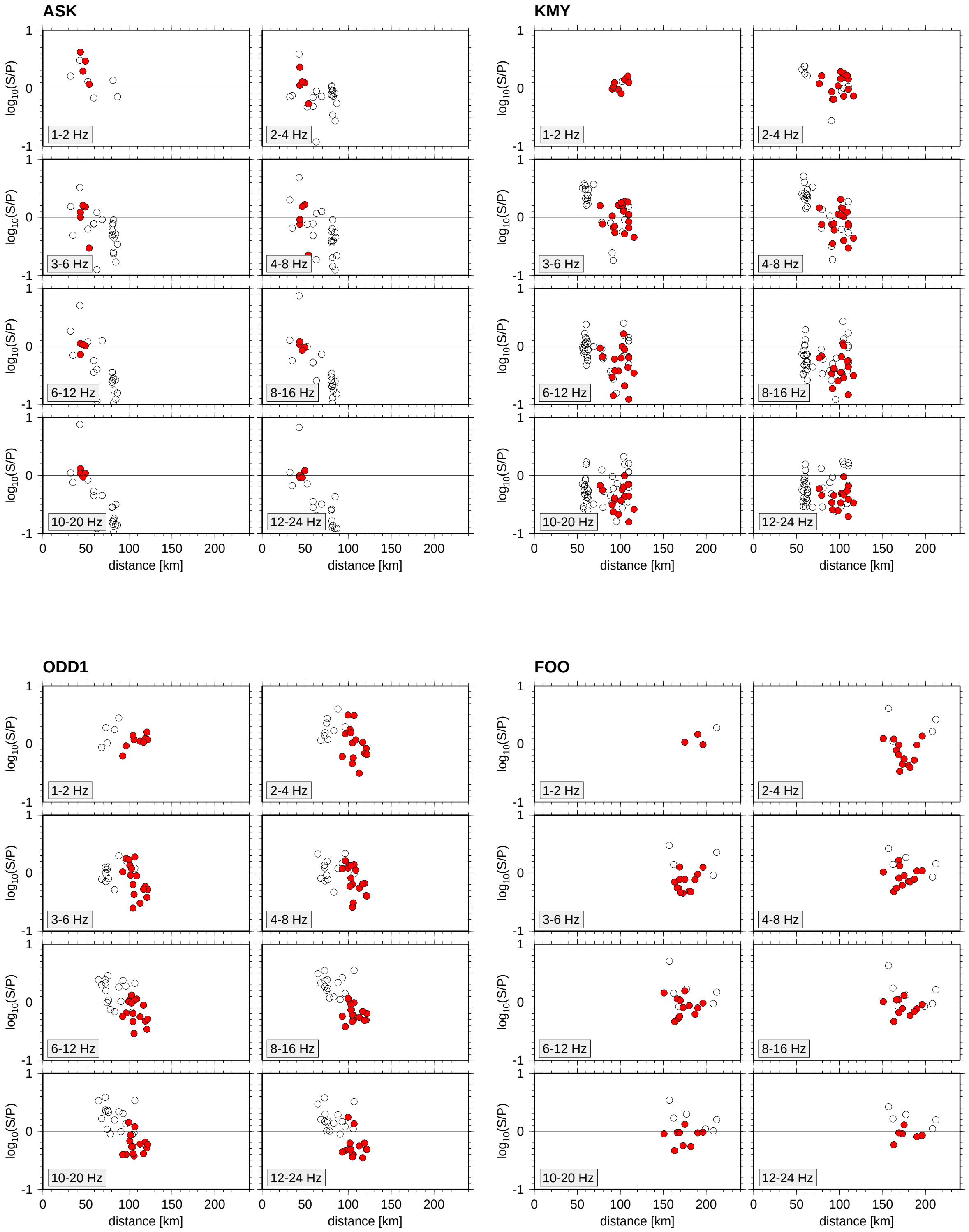

Figure 7. S/P amplitude ratios (logarithm) as a function of source-receiver distance and frequency band for all events recorded at four selected stations. Symbol colors and station locations are shown in Figure 1 (red: explosions, open circles: natural events).

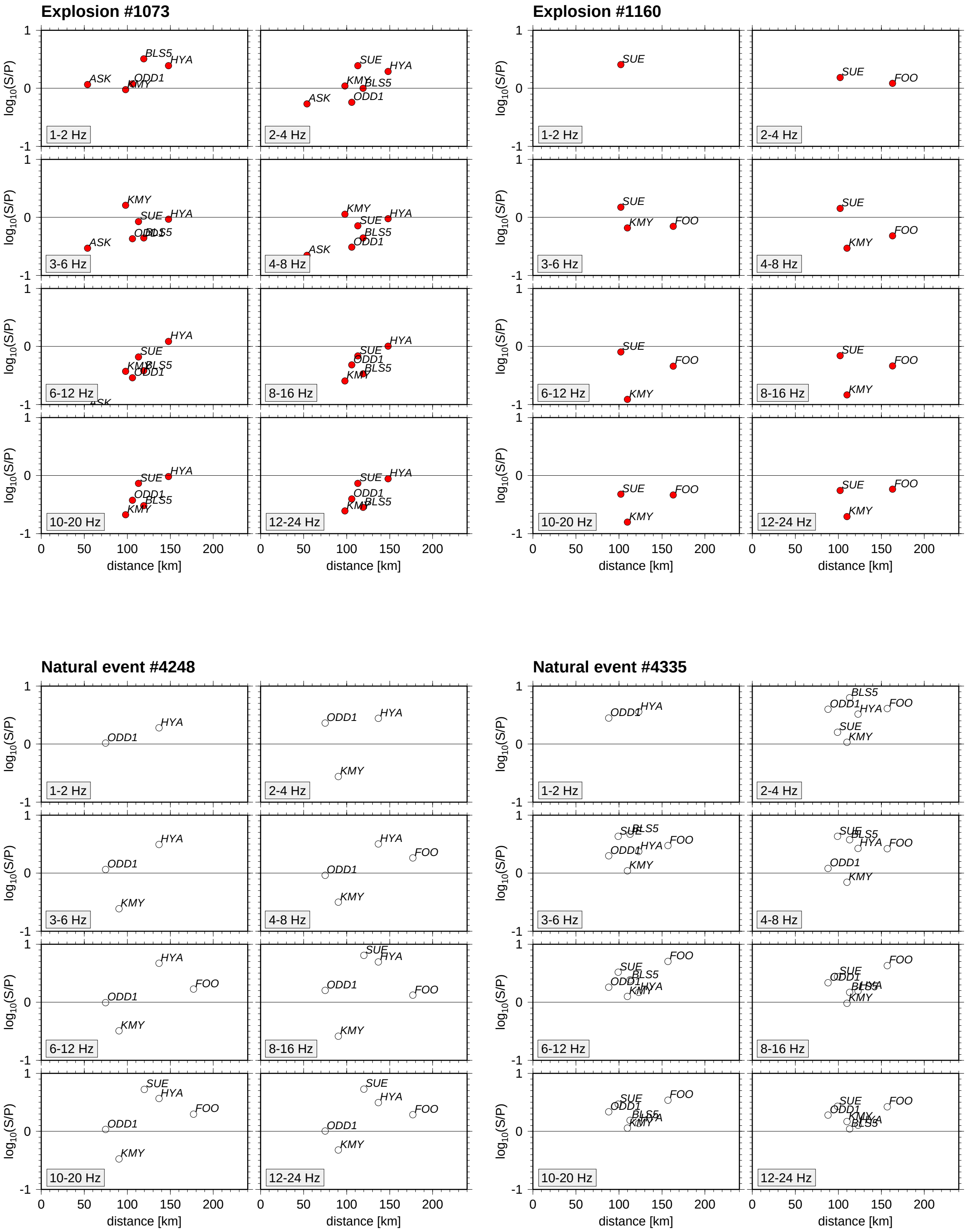

Figure 8. S/P amplitude ratios (logarithm) as a function of source-receiver distance and frequency band for selected events and all analyzed stations. The top two panels show explosions and the two bottom panels natural events. Symbol colors and station locations are shown in Figure 1.

Discussion

S/P amplitude ratios were measured at regional distances (20-220 km) for explosions and natural events in a series of 1 octave frequency bands. Figure 9 summarizes the mean and median S/P amplitude ratios for each set of events and frequency band. Explosions show decreasing mean and median S/P amplitude ratios with increasing frequency, which means that explosions are characterized by higher P-wave energy relative to S-wave energy at high frequencies. Mean and median S/P ratios are higher for natural events than for explosions above about 3 Hz. However, the distributions of S/P ratios for explosions and natural events overlap significantly in all analyzed frequency bands. This may be partly related to path and/or site effects at different stations as evidenced in Figure 8.

To illustrate these path effects, Figure 10 shows measured S/P ratios and corresponding mean values for explosions and natural events recorded at four selected stations. Both absolute S/P ratios and the shape of S/P as a function of frequency differs from station to station. But at an individual station, e.g. BLS5 (bottom panels), S/P ratios for natural events seem to be better separated from those for explosions than in a combined analysis for all stations.

In conclusion, mean S/P amplitude ratios for explosions and natural events differ at individual stations and are in general higher for natural events and frequency bands above 3 Hz. However, the distributions of S/P ratios for explosions and natural events overlap in all analyzed frequency bands. Thus, for individual events in our study area, S/P amplitude ratios can assist the discrimination between an explosion or a natural event, but other measures, such as more refined spectral analysis, should also be included in the interpretation.

Even though we have tried to reduce the difference in path effects for the two event populations by considering events located in the same geographical region recorded at the same stations, there are still differences left that cannot be resolved from the data.

The fact that the earthquakes are located at depth in the crust, imply that they experience different path effects than the explosions carried out in water. Another issue is how explosions in water can give rise to S energy by P-S conversions at the sea bottom and the free surface, or by scattering caused by the topography of a fjord or nearby mountain. We will in the next section provide some wavefield simulations illustrating the effect of such mechanisms.

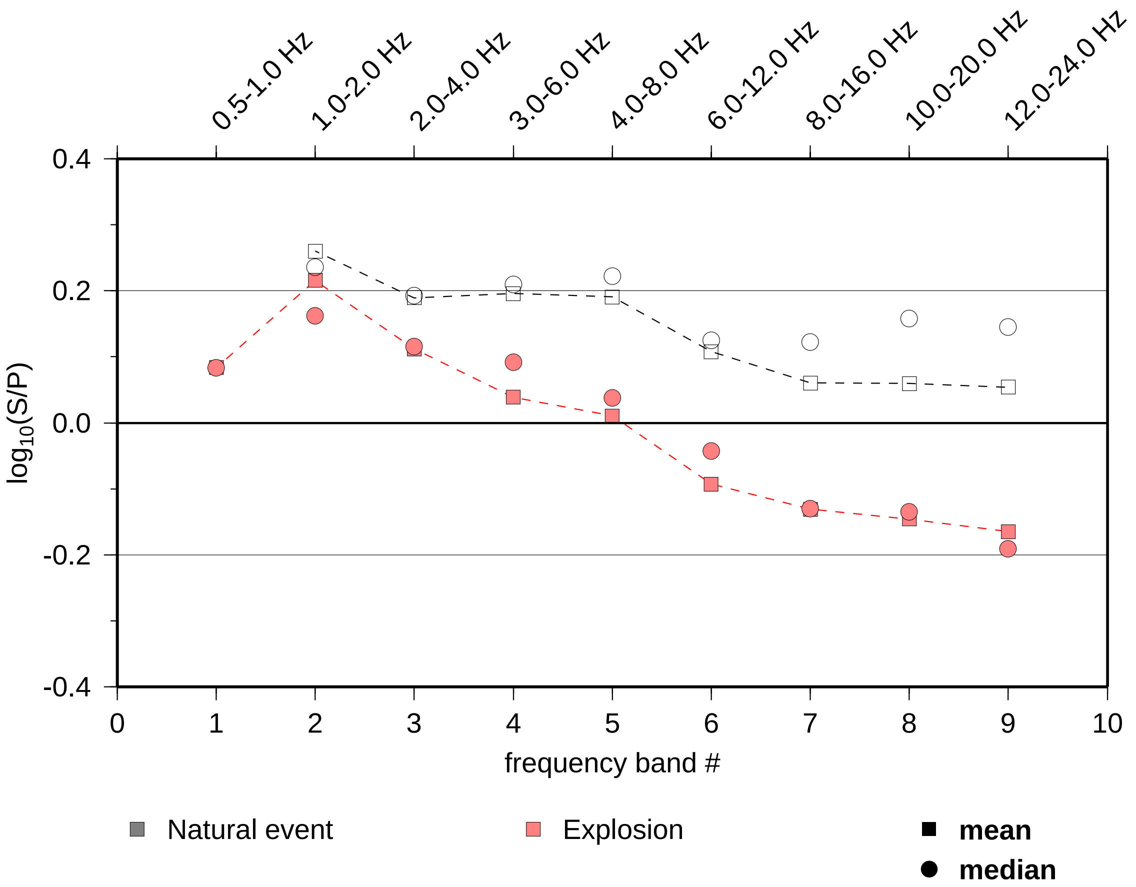

Figure 9. Mean and median S/P amplitude ratios (logarithm) for different event sets as a function of the frequency band.

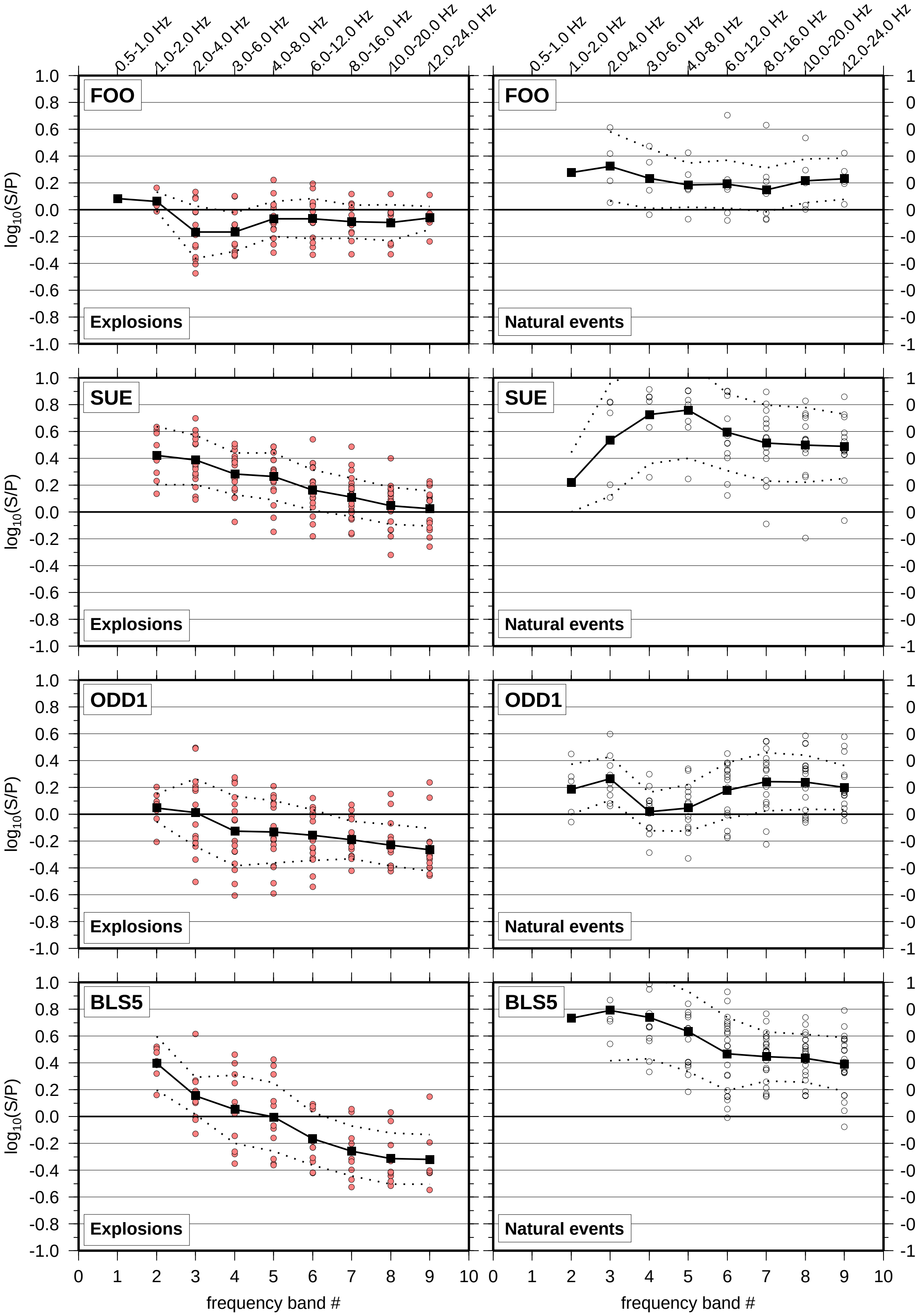

Figure 10. S/P amplitude ratios (logarithm) for explosions (left) and natural events (right) recorded at individual stations. Mean values are plotted as black squares and solid lines, and dashed lines indicate one standard deviation.

2.2 Shear-Waves from Explosive Sources in Layered Structures

We have conducted a series of 1-D modeling experiments to illustrate the generation of shear-waves in an average crustal model for Fennoscandia (see Figure 11).

The four panels of Figure 12 show snapshots of the amplitudes of the seismic subsurface wavefield for an explosion located at 400 meter depth, calculated using the finite difference code of Robertsson et al. (1994). Besides shear-wave energy converted from P-waves, a non-geometric S-wave is generated by the immediate interaction of the source with the free surface. Once generated, this non-geometric shear-wave propagates as a regular shear-wave (Sg, Sb and Sn).

Figure 12 shows that even for this simple model the wavefield becomes quite complex.

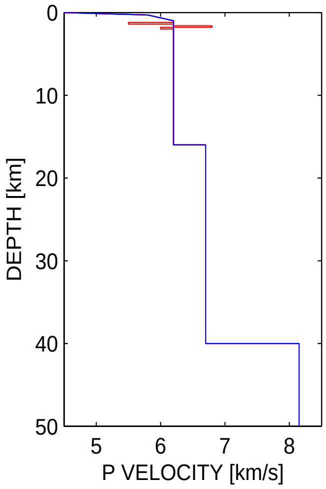

Figure 11. Average crustal P-velocity model for Fennoscandia (blue). A perturbation for the upper crust is shown in red

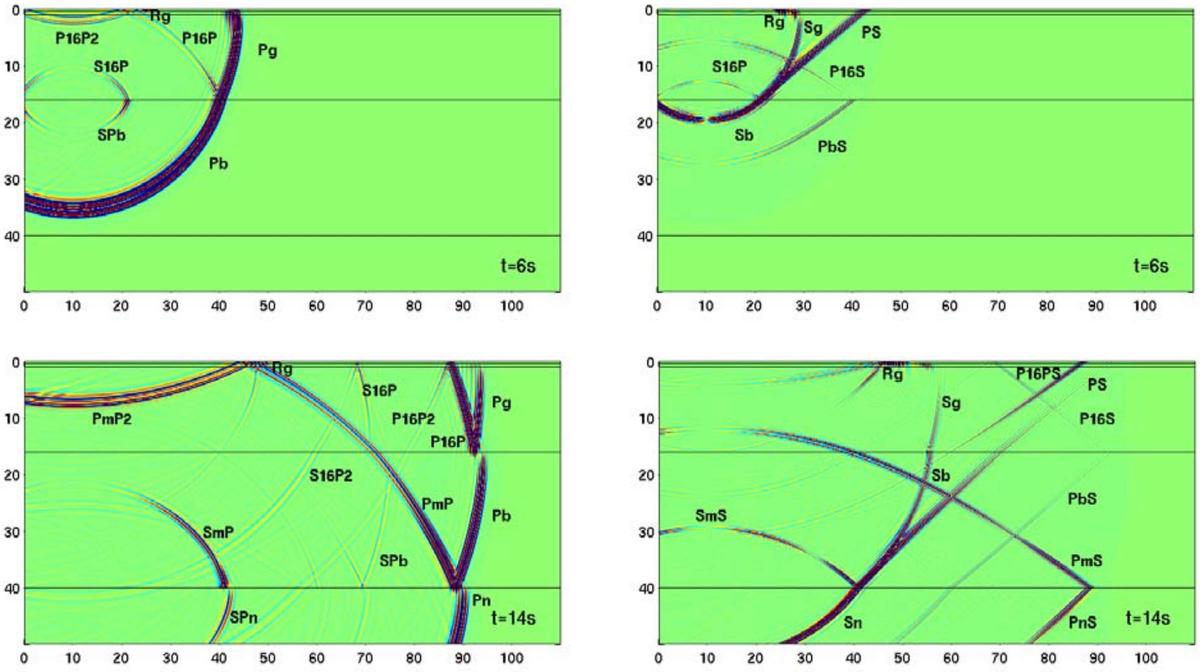

Figure 12. Results from finite-difference calculations of the wavefield in an average crustal model for Fennoscandia (blue curve of Figure 11) for an explosive source located at 400 m depth. The two left-hand panels show snapshots of the amplitudes of the compressional component at 6 and 14 seconds after the origin time. The two right-hand panels show snapshots of the amplitudes of the shear component at the same time instances.

Synthetic seismograms with receivers at the surface for distances up to 250 km are shown in Figures 13-16, calculated using both the average Fennoscandia model (drawn in blue in Figure 11) and a model with a perturbed upper crust (drawn in red in Figure 11). Details about the different scenarios are given in the figure captions. The synthetic seismograms were calculated with the reflectivity method (Müller, 1985), using a dominant frequency of 2 Hz.

Figures 13-16 show the vertical component of the velocity, plotted with a reduction velocity of 3.9 km/s.

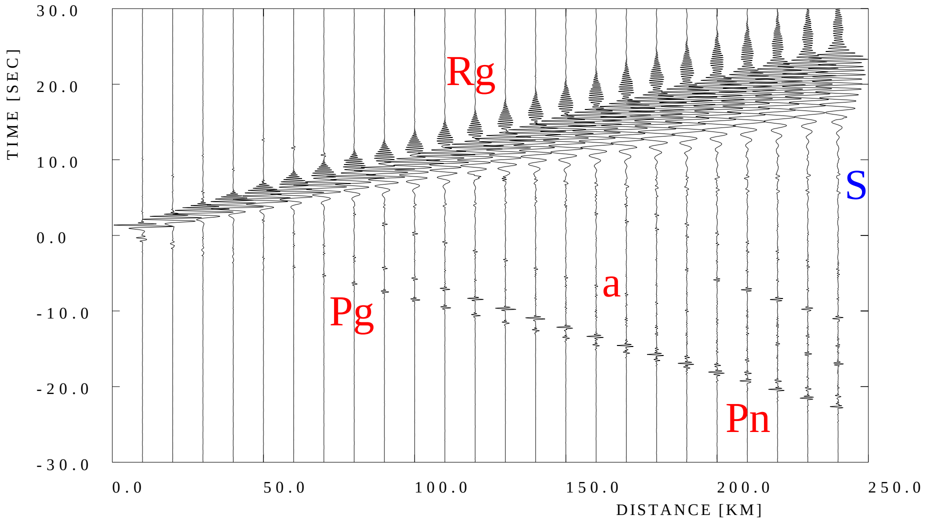

Figure 13. Seismogram section for an explosion source in the simple model at a depth of 0.5 km. Rg is the dominant phase. Some energy is traveling with S velocities, generated by interaction between the source and the free surface. The local and regional onsets Pg and Pn are clearly seen. The wavefield contains clear phases (a) in an approximately 30 s long time window after the first P onsets. Amplitudes are trace normalized.

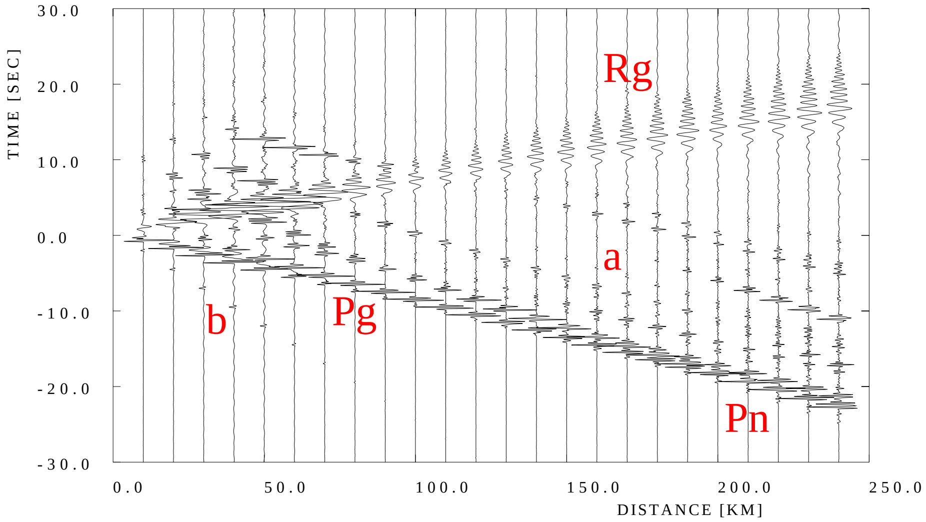

Figure 14. Seismogram section for an explosion source in the simple model at a depth of 1.5 km. The body-wave phases are more pronounced than Rg. The wavefield contains many phases (a) in an approximately 30 s long time window after the first P onsets. The phase (b) is a numerical artifact. Amplitudes are trace normalized.

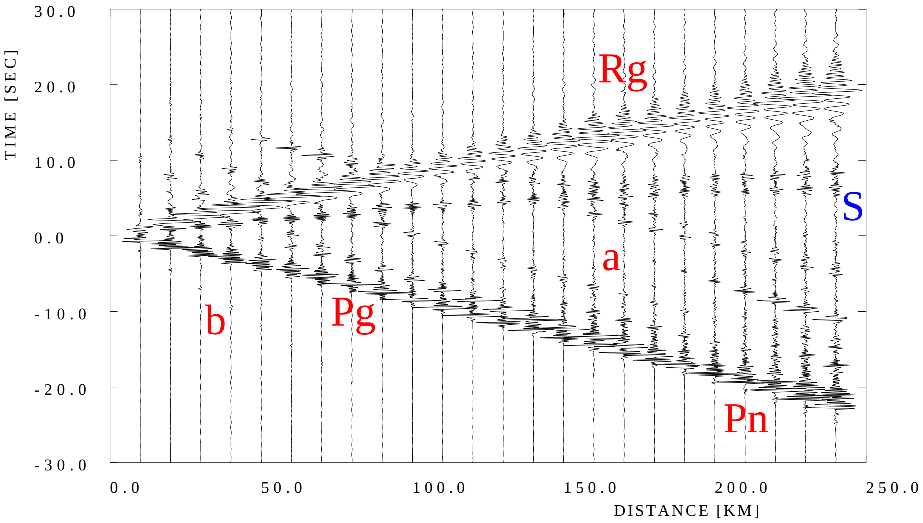

Figure 15. Seismograms for an explosion source at 1.5 km depth in the model with a perturbed upper crust (red curve of Figure 11). The impedance contrasts in the source area produce much P-to-SV converted energy, which in turn result in clear S onsets. The wavefield contains many phases (a) in an approximately 30 s long time window after the first P onsets. The phase (b) is a numerical artifact. Amplitudes are trace normalized.

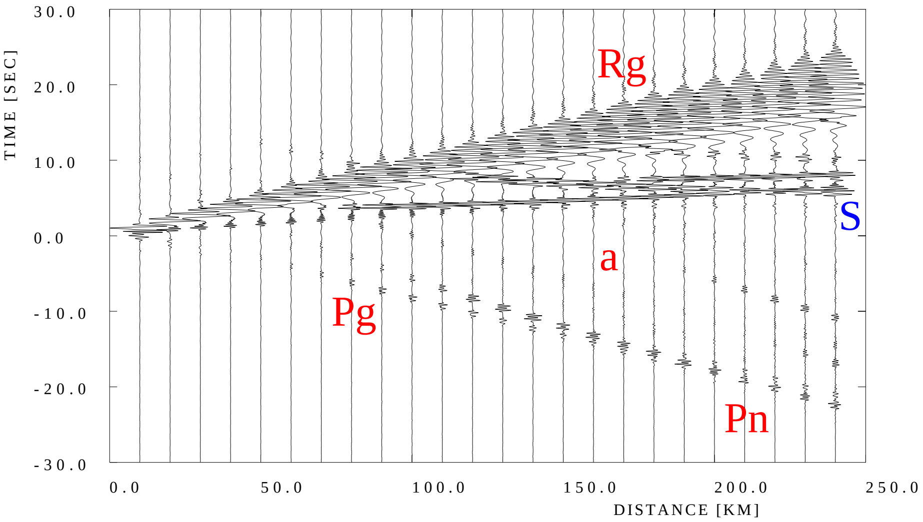

Figure 16. Seismogram section for a single vertical force source a depth of 1.5 km in the average Fennoscandian model (blue curve of Figure 11). This source type directly radiates S energy which is clearly visible in the seismograms. The wavefield contains less pronounced phases (a) in an approximately 30 s long time window after the first P onsets. Amplitudes are trace normalized.

These case studies indicate that S phases in a horizontally layered model can only be generated by either non-isotropic sources or by interaction with heterogeneities nearby the source. All conversions along the ray path from the source to the receivers contribute only to the coda of the regular phases (Pn/Pg, Sn/Sg).

2.3 Modeling of Shear-Waves from Explosions in Water

In order to investigate S-waves generated from explosions in water, we have conducted additional calculations using a frequency-wavenumber code (Wang, 1999) allowing both the source and the receivers to be located at depth. We have replaced the uppermost 200 m of the Fennoscandian crustal model with water, shown in Figure 11, and put the sensors at a depth of 210 meter, i.e. 10 m below the sea bottom. Figure 17 shows the vertical component synthetic seismograms for an explosion source in water at a depth of 10 m. The dominant frequency of the signal pulse is about 2 Hz.

The large Rg phase and the resonance effect of the water layer on Rg is not very interesting in our context, as the continuous water waveguide carrying the Rg phase is generally absent for the propagation paths discussed in Section 2.1 (see Figure 1). However, the modeled amplitudes of the P and S body wave phases provide useful insight into the degree of S-wave energy generated from explosion sources, and shows that similar mechanisms also are in effect for more realistic complex media. It can be seen from Figure 17 that the first-arriving S-phase has a comparable amplitude to the P-phase, at least for distances greater than 100 km. The effect of reverberations in the water layer are seen as coda energy related to the different arrivals.

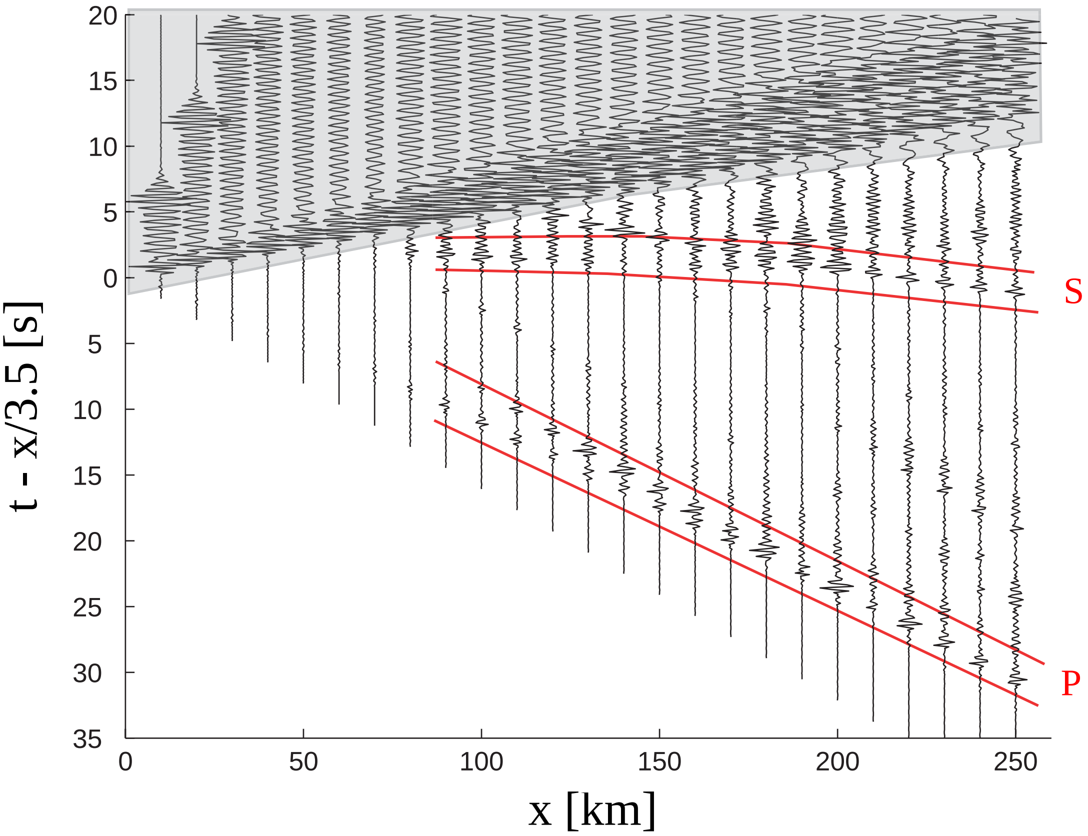

Figure 17. Trace normalized vertical component seismogram section for an explosion in water at a depth of 10 m, as described in the text above. Rg is the dominant phase (shaded area), but is not important in this discussion of shear-waves. Significant energy is traveling with S-wave velocities, generated by interaction between the source and the sea bottom. The S-wave amplitudes are comparable to those of the P phase.

For comparison, we show in Figure 18 a similar wavefield simulation, but now without the 200 m water layer. Rg still has the largest amplitudes, now propagating with higher velocity than in the case shown in Figure 17. Also in this case some shear-energy can be observed, but with an amplitude 2-3 times smaller than P.

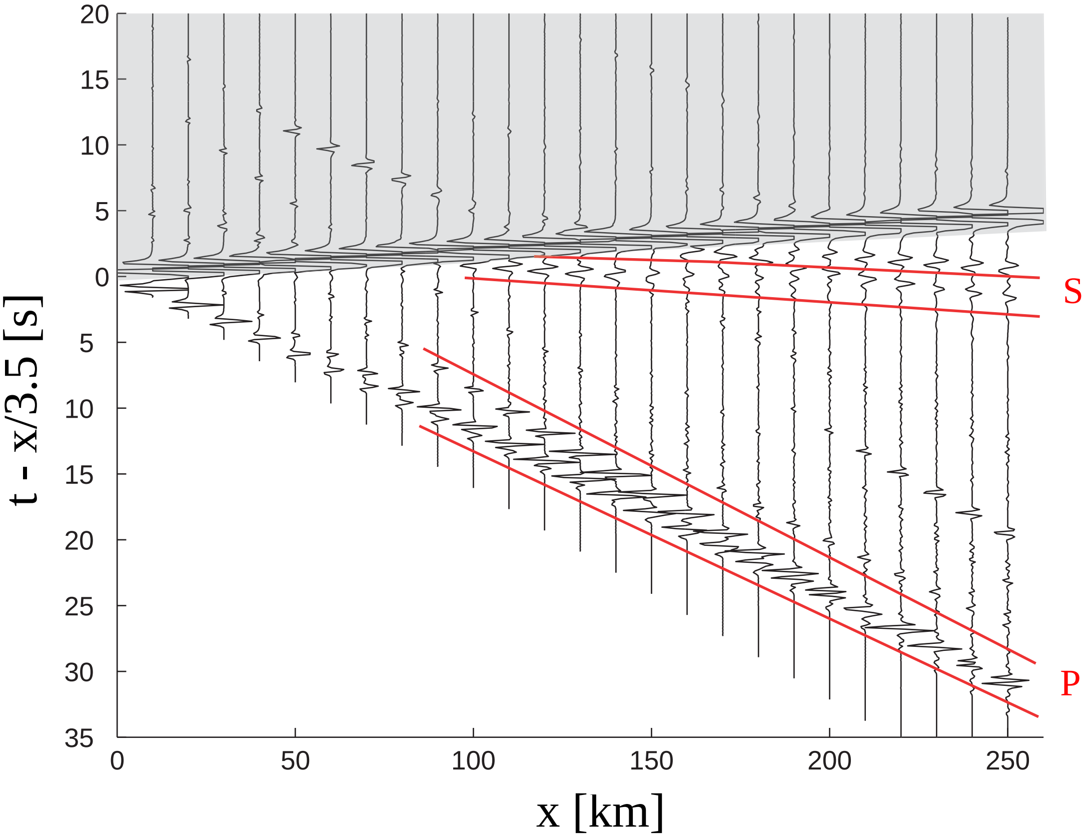

Figure 18. Trace normalized vertical component seismogram section for an explosion at a depth of 10 m into the crust, as described in the text above. Rg is the dominant phase (shaded area), but is not important in this discussion of shear-waves. Some energy is traveling with S-wave velocities, generated by interaction between the source and the free surface. The S-wave amplitudes are 2-3 times smaller than those of the P phase.

2.4 Summary

The results presented in the preceding sections can be summarized as follows:

- The synthetic seismograms calculated for simple 1-D models demonstrate that explosions also generate shear-wave energy if they are fired close to an interface with a strong material contrast (as is the case for most explosions), such as the free surface or the ocean bottom.
- The single force source generates much stronger S-waves than the explosion. The same is assumed to hold for double-couple sources averaged over the radiation pattern.
- Synthetic seismogram calculations confirm that the generation of S-type energy at impedance contrasts later along the ray paths contribute essentially only to the seismic coda of the direct P and S arrivals. This coda energy does not dominate the amplitude behavior of the seismograms. Therefore, in simple 1-D modes S/P-ratios can be used as a discrimination criterion.
- The S/P ratios of the analyzed data sets only give an indication of the source type. Variation of layer topography and 3-D heterogeneities can focus and defocus P- as well as S-wave amplitudes in different ways. This variation in S/P ratio is one reason for the width of the observed distributions and the overlap between the data sets.
- As seen from Figure 6 and 9 in Section 2.1, there is a larger difference in S/P ratios between earthquakes and explosions for higher frequencies. This can be explained by the fact that at low frequencies (larger wavelengths), discontinuities and structural heterogeneities in the explosion source region are stronger generators of converted S energy.
  The S*-phase, for example, is most efficiently generated whenever an explosion source is located close (within one wavelength) to a strong discontinuity.
- The path dependence of the observed S/P amplitude ratios, as seen in Figure 10, may also get a significant contribution from lateral heterogeneities in the source region, producing variable levels of P-to-S conversion in different directions from the source.
- Mean S/P amplitude ratios for explosions and natural events differ at individual stations and are in general higher for natural events and frequency bands above 3 Hz. However, the distributions of S/P ratios for explosions and natural events overlap in all analyzed frequency bands. Thus, for individual events in our study area, S/P amplitude ratios can only assist the discrimination between an explosion or a natural event.

3 Analysis of In-Mine Data

The Pyhäsalmi mine in central Finland has been a key element in the research associated with this project. Through cooperation with representatives of the mining company we have obtained detailed information about the geology of the mine, the mining infrastructure and the mining practice. In addition, we have been provided with all data from the in-mine seismic monitoring system that became operational in late 2002. This data set consisted by the end of 2005 of more than 30 000 seismic events, including the mine blasts. An interesting observation from most of the mine blast is the occurrence of shear-wave energy at the in-mine seismic stations, with an example shown in Figure 19. The analysis and modeling of this phenomenon is one of the most important tasks that will be addressed in the subsequent sections.

In this section we first describe the Pyhäsalmi ore mine in terms of geology, tunneling, and the in-mine network. The next sub-section is associated with estimation of source parameters and source scaling for the natural seismic events, and the final data analysis topic concerns differences in S/P ratios between mine blasts and natural seismic events.

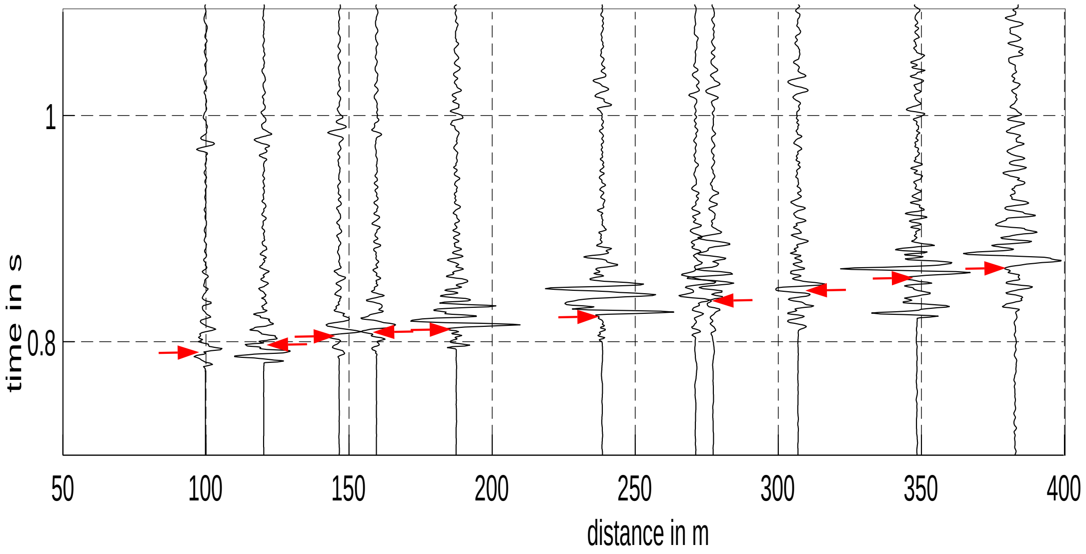

Figure 19. Record section in the Pyhäsalmi in-mine network for a single detonation of a ripple-fired production shot. For each of the three-component sensors we have chosen the component having the largest S-phase. We have not included vertical-component observations where the rays approach the sensors at steep angles, as the S-arrivals on these sensors have very small amplitudes. The S arrivals are indicated with red arrows.

3.1 The Pyhäsalmi Ore Mine

The Pyhäsalmi ore mine in central Finland extends to a depth of 1.4 km and is the deepest of its kind in western Europe. Massive sulfide ores form a potato-shaped body, which seems to be located in the hinge of a large synform fold (Puustjärvi, 1999). The ore body is medium-to-coarse grained and consists of sphalerite-pyrite with some zinc (2-10%) in the outer rim and in an inner rim of chalcopyrite-pyrite with a copper content of 1-6%, while the innermost part of the ore body is uneconomical pyrite. The ore body is surrounded mainly by quartz-rich felsic volcanics (80-90%) with amphibolite bands that vary in width from millimeters up to meters. The whole fold hinge is defined by distinct schistosity. Cracks are most prominent in the schistosity/banding direction. There are numerous pegmatite veins, varying in size and orientation.

The veins are common near the ore contacts. There are no distinct faults in the active mining area between 1100 and 1450 m depth that could have been activated by mining. However, pegmatites might play a role for the stability of the mining area, as pegmatite veins have been identified as fault planes. Furthermore, severe shearing has occurred in the geological past in Pyhäsalmi, and there are active faults outside the current mining area and near the surface.

The complete mining infrastructure with its tunnels, stopes and passes has been surveyed by laser scanning and a model was built using a mine design software. This software allows to update the model in response to successive mining. The mine is quarried by sublevel and bench stoping, achieving an annual production of about 1.3 Megatons of ore.

Prior to the start of the mining below 1000 m, stresses were measured at a depth of 1225 m. The main principal stress is horizontal compression at N310^{o}E, with vertical stress σ_V =33 MPa, maximum horizontal stress σ_H =65 MPa, and minimum horizontal stress σ_h =41 MPa (Ledger, 1999). A stress balance like this will normally produce reverse faulting. This is largely in agreement with tectonic stress directions from the world stress map (Reinecker et al., 2004), even though secondary effects of mining might have disturbed the stress field as compared to intact rock conditions.

The in-mine network in the Pyhäsalmi mine is provided by ISS International Ltd., and initially comprised 4 three-component and 12 vertical-component sensors (see Figure 20). In May 2004 two additional three-component sensors were installed in the lower part of the mine. The geophones are cemented in 10.5 m long boreholes (76 mm in diameter) that were drilled vertically into the roof of the tunnels. The natural frequency of the geophones is at 4.5 Hz, and the instrument response is flat for frequencies above 10 Hz. Sampling rates are generally at 3000 Hz, in a few cases, however, downsampling to 1000 Hz or 500 Hz was carried out to save storage space. This network has been operational in a continuous mode since January 2003, and up to March 2004, about 18,000 events were detected and recorded. About two thirds of these events were identified as blasts related to the mining operations while the remaining ~6000 were natural seismic events (microearthquakes; likely mining induced).

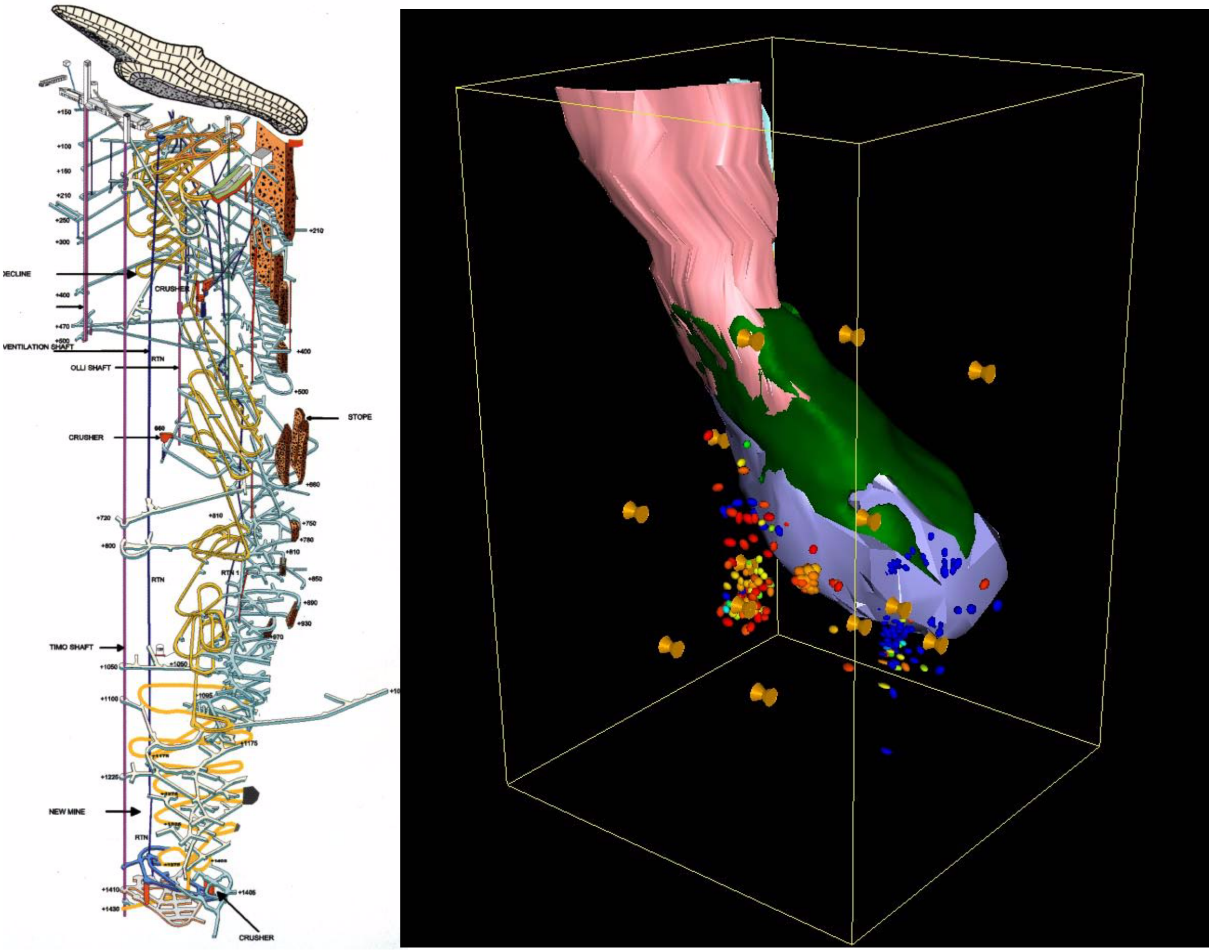

Figure 20. The left-hand part of the figure shows the shafts and access tunnels of the Pyhäsalmi mine from the surface down to a depth of 1500 meters. The right-hand part of the figure shows a three-dimensional model of the mine, for the depth range 800 - 1500 meters. Green represents copper ore, blue represents zinc ore, and pink represent backfilled material. The locations of the initial 16 in-mine monitoring stations are indicated by yellow symbols. Events comprise mine blasts and microearthquakes during September 2003. Material properties assigned to the different rock types are given in Table 1.

Table 1: Initial material properties assigned to the Pyhäsalmi mine

Rock type	Density (g/cm^3)	P-velocity (km/s)	S-velocity (km/s)
Copper ore (green)	4.6	7.39	4.59
Zinc ore (blue)	4.2	5.54	2.89
Backfill (pink)	1.8	2.66	1.54
Surrounding rocks (Gneiss, transparent)	2.8	6.00	3.46
Voids, represented as water	1.0	1.48	0.00

3.2 Estimation of Source Parameters (source scaling)

This section contains a brief summary of the results from the study on the estimation of source parameters and source scaling. A full BSSA paper describing this research is included as an appendix to this report (Appendix 2).

We have studied scaling relations for about 1500 visually checked natural seismic events in the Pyhäsalmi mine occurring over a time period of 15 months, selected on the basis on signal-to-noise ratio (>3), number of channels (>12), location error (<10 m) and rms time residual (<5 ms). The resulting frequency-magnitude distribution indicates a 50% detectability at M_w=-1.6 and a slope (b-value) between about 1 and 1.3, see Figure 21.

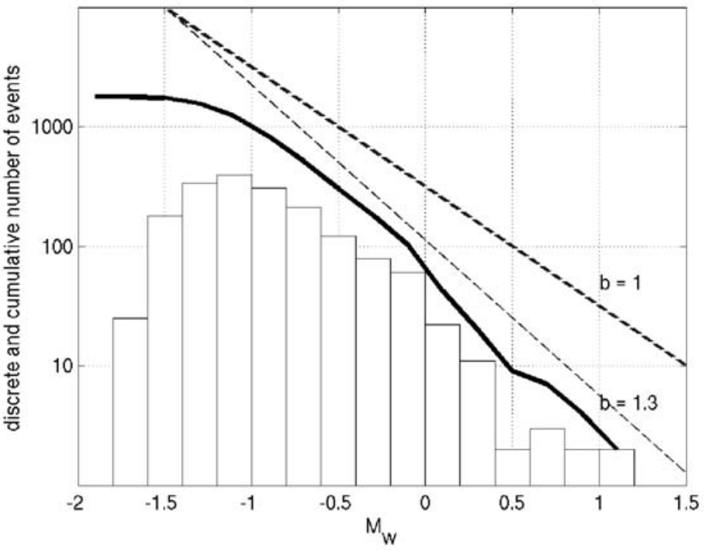

Figure 21. Discrete and cumulative number of visually checked natural seismic events from January 2003 to March 2004. *b*-values are close to one for moment magnitudes M_w -1 to 0

Source parameters for the events in this data base of 1500 events have been extracted using an ω^{-2}-model and a Q-value of 350. As seen from Figure 22, the data satisfy more or less the general $M_0 \sim f_c^{-3}$ scaling relation, with stress drop in the range from 0.01 to 1.0 MPa, increasing slightly with M_0.

We have found a strong variation in Q that most likely is related to the complexity of the mine (voids and tunnels). Values between 200 and 800 are found, however without major influence on source parameters. We have also studied Q using a spectral ratio (multiple-empirical Green's function, MEGF) technique, finding an increasing Q with increasing frequency.

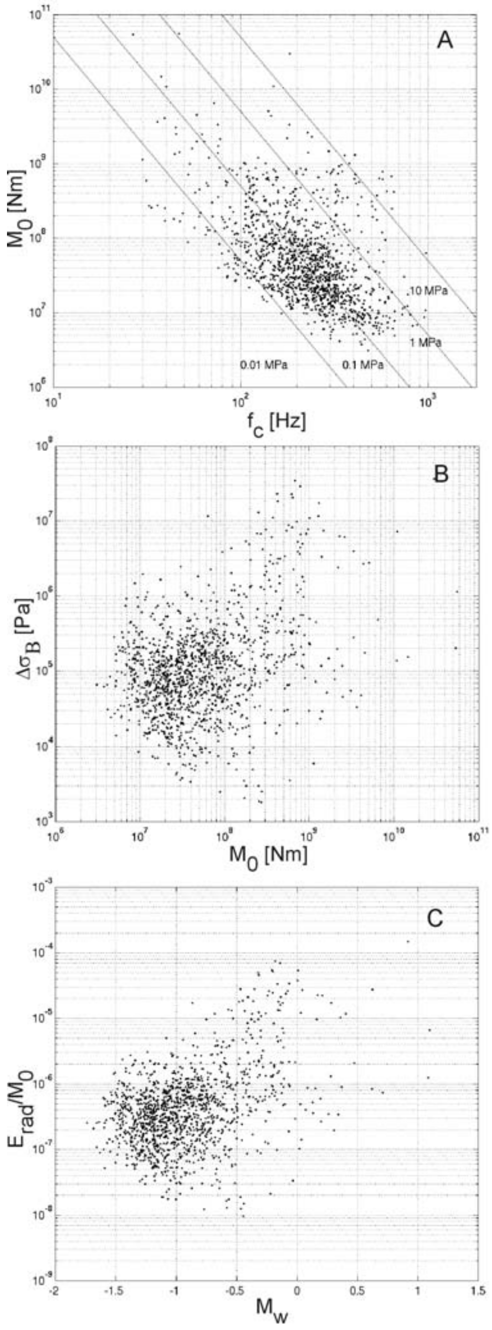

Figure 22. Data points shown are determined by using a constant Q = 350 and fitting an ω^{-2} spectral model.
(A) Data fit the general $M_0 \sim f_c^{-3}$ relation, where lines indicate constant stress drops.
(B) Brune stress drops varies from about 0.01 to 1 MPa, slightly increasing with M_0.
(C) Energy-to-moment ratio seems to increase with M_W.

Seismic energy-to-moment ratios are almost constant when using Q values based on MEGF, while the ratios are slightly increasing with M_0 when we assume constant Q models. When connected to a larger data base (see Figure 23), over 11 orders of magnitude, the ratios seem to satisfy the scaling relation $M_o \sim f_c^{-(3+\varepsilon)}$ with an ε of slightly above 0.5, indicating increasing apparent stress with increasing magnitude (cf. Kanamori and Rivera, 2004).

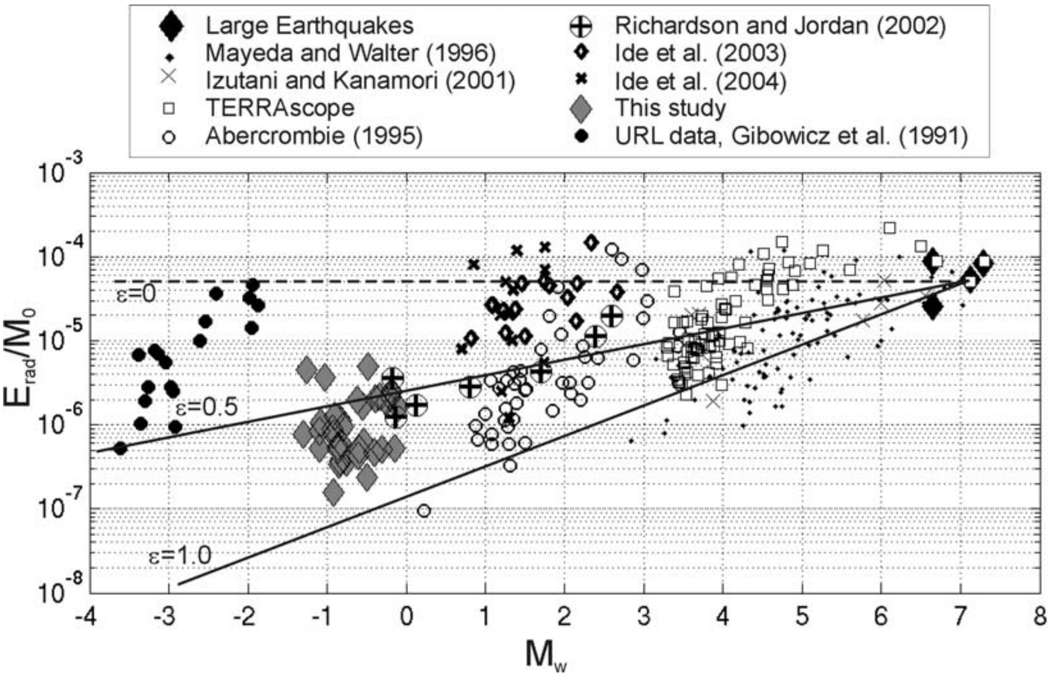

Figure 23. Energy-to-moment ratios for a number of different data sets, showing a variation of about 3 orders of magnitude over a range of 11 moment magnitudes. The results from the present study include events from clusters C1 and C2, assuming Q(f) based on the MEGF method (gray diamonds). Black lines indicate trends for E_{rad}/M_0 for the scaling relation $M_o \sim f_c^{-(3+\varepsilon)}$, with ε=0, 0.5 and 1. Results from other studies include deep South African gold mines (Richardson and Jordan, 2002), the Long Valley Caldera, California (Ide et al., 2003), the Hi-net, Japan (Ide et al., 2004), 18 events that are representative for the Underground Research Laboratory data (Gibowicz et al., 1991) and shallow crustal earthquakes in California and Japan (compiled by Kanamori and Rivera (2004)). Details about the references given in this figure are included in the BSSA paper of Appendix 2.

3.3 S/P Ratios for In-Mine Data

We have investigated the problem of estimating the S/P ratios for events in the Pyhäsalmi mine. The S/P ratios are obtained in the time domain using different bandpass filters. We will in the following demonstrate a reanalysis of a ripple-fired blast in one of the mine stopes from 14 January 2003 using this approach. The blast consisted of about 20 individual detonations within a small region (20-30 m). The corresponding seismic onsets were automatically picked (P- and S-phases) and, from the polarization analysis of the P-wave signal, the direction of the incoming wavefield was determined. Using these event parameters, the shots were located assuming a homogeneous velocity model. With the exception of a few locations, most of the automatically determined hypocenters cluster nicely, see Figure 24.

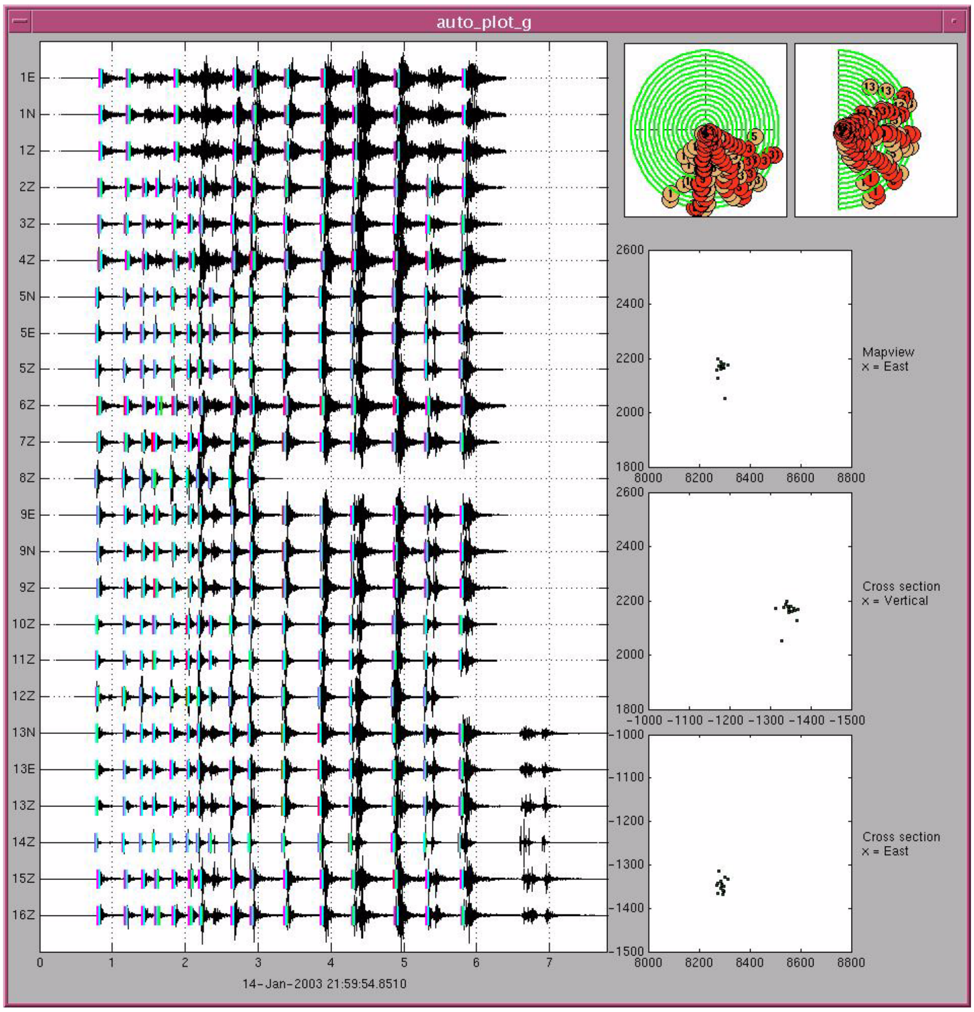

Figure 24. Waveforms and automatic processing results for a ripple-fired explosion in the Pyhäsalmi mine. The left panel shows a time segment of about 8 seconds automatically stored by the ISS system. Signal detections and onset estimates of the P- and S-phases are marked by vertical bars. The results from polarization analysis of the P-phases are displayed in the two uppermost right plots (backazimuths and incidence angles). The three plots below show the automatically located hypocenters in a map view and two cross-sections.

The P- and S-phases of 16 of the ripple-fired detonations were then manually picked at each of the 4 three-component sensors of the Pyhäsalmi in-mine seismic network, and appropriate time windows were positioned around these onsets. Figure 25 shows the LTQ rotated record of sensor PS05 located about 198 meters from the estimated location. As can be seen, the size and duration of the different detonations vary significantly within the time interval of the ripple-fired blast, and some of the latest signals in fact consist of 2 detonations fired within a short time.

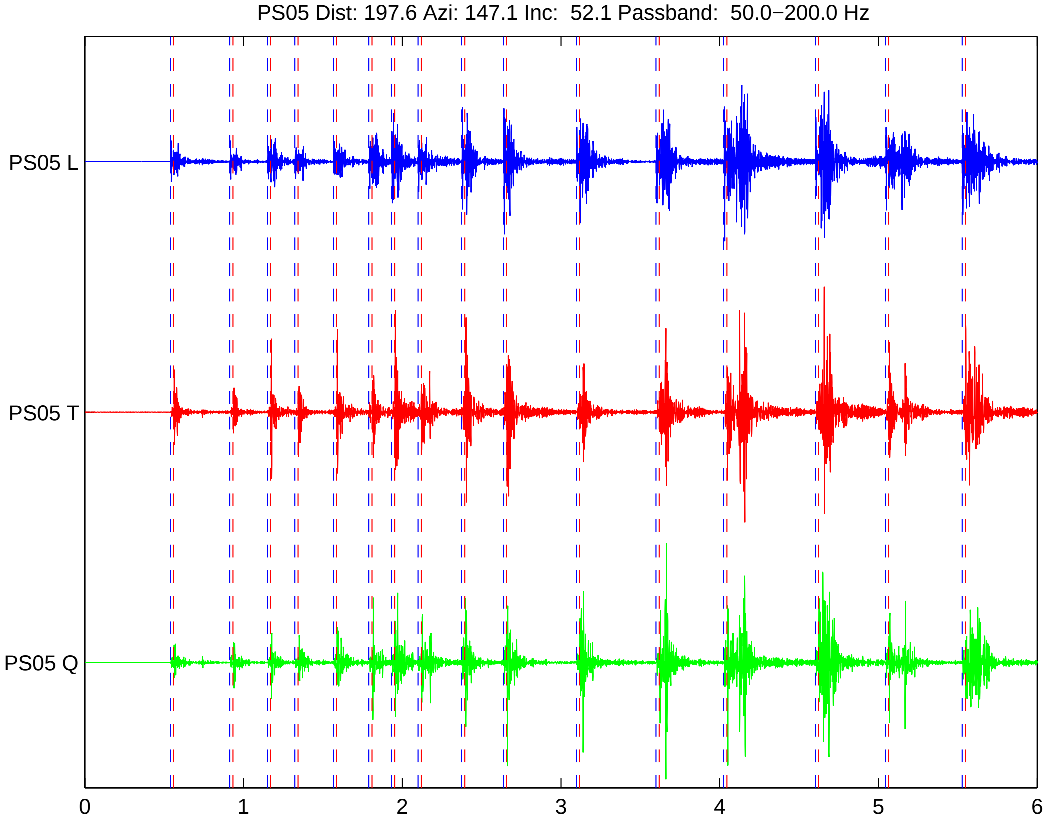

Figure 25. LTQ rotated waveforms of the three-component sensor PS05, filtered in the passband 50-200 Hz. The station is located 198 meters from the estimated location. The blue and red vertical dashed lines show the P- and S-phase onsets of from the different detonations. The azimuth and incidence angle used for rotation into the LTQ coordinate system was taken from polarization analysis of the first P-arrival in the sequence.

The measurement of the maximum P and S amplitudes were done for passbands with 1 octave bandwidth, and the filtering was done with a 3rd order Butterworth filter. The list of passbands are listed in Table 2.

Table 2: Passbands (in Hz) used for measurement of P and S amplitudes

20-40	30-60	40-80	50-100	60-120
70-140	80-160	90-180	100-200	120-240
140-280	160-320	180-360	200-400	250-500
300-600	350-700			

The LTQ rotated traces of the sensor closest to the event (PS13) is shown in Figure 26 for the first detonation if the ripple-fired blast.

The time difference between the S- and P-phases are in this case only 0.0204 seconds, corresponding to a cycle with a frequency of 49 Hz. From inspection of the data filtered in the passbands given in Table 2, we have found that P and S do not separate sufficiently unless the lower cutoff of the passband is approximately greater than 1.5/($S_{arrtime}$-$P_{arrtime}$), which in this case is 73.5 Hz. This implies that we cannot obtain interpretable P and S amplitudes for the six lowest passbands given in Table 2. However, the lowest passbands provide interpretable P and S amplitudes at more distant stations where P and S have longer time separation.

A 50-200 Hz passband is used to display the data in Figures 25 to 29. Due to the dominance of frequencies close the higher cutoff of 200 Hz, the P and S-phases can clearly be separated at all stations, but for the 50-100 Hz passband this is not the situation at all stations.

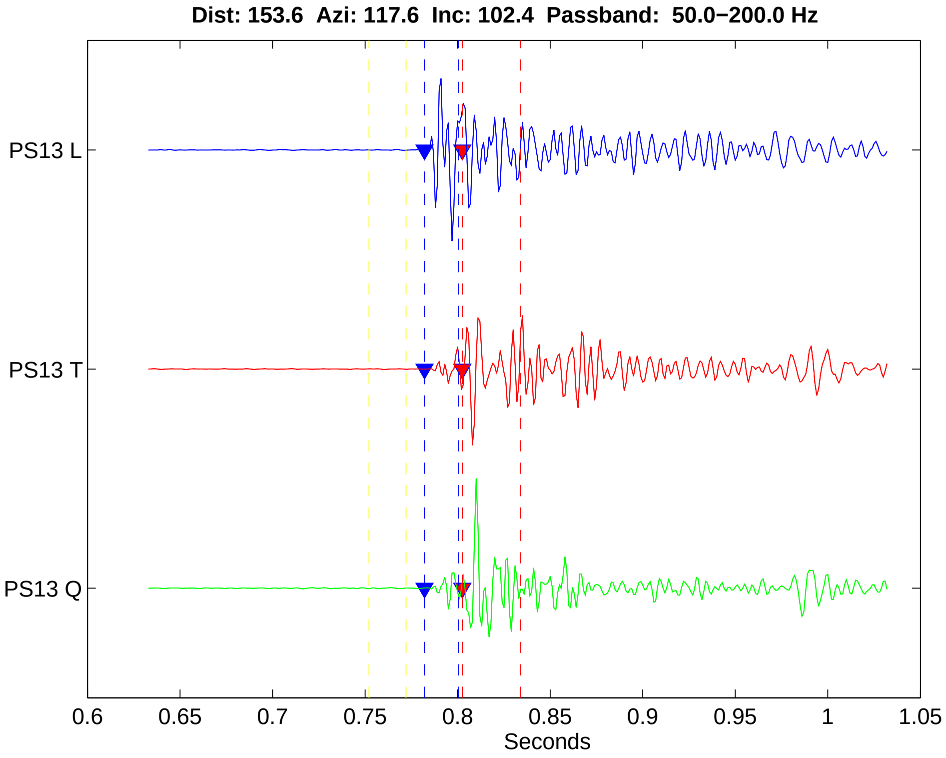

Figure 26. LTQ rotated waveforms of the three-component sensor PS13, filtered in the passband 50-200 Hz. The station is located 154 meters from the estimated location. The P and S arrival times are shown by blue and red triangles, respectively. The P and S analysis windows are shown by the blue, and red dashed lines. The azimuth and incidence angle used for rotation into the LTQ coordinate system was taken from polarization analysis of the P-arrival.

Figure 27 shows the LTQ rotated traces for the first detonation recorded at PS05, located at a distance of 198 meters from the event. For measurement of the S/P ratios the P amplitude is taken to be the maximum amplitude on the L-component within the P window. For measurement of the maximum S amplitude we calculate the total S-wave amplitude in the TQ plane from the amplitudes on the T and Q components. These amplitudes are shown by the black envelope plotted on top of the T and Q traces of Figure 27. The S amplitude is taken to be the maximum of this envelope within the S-window.

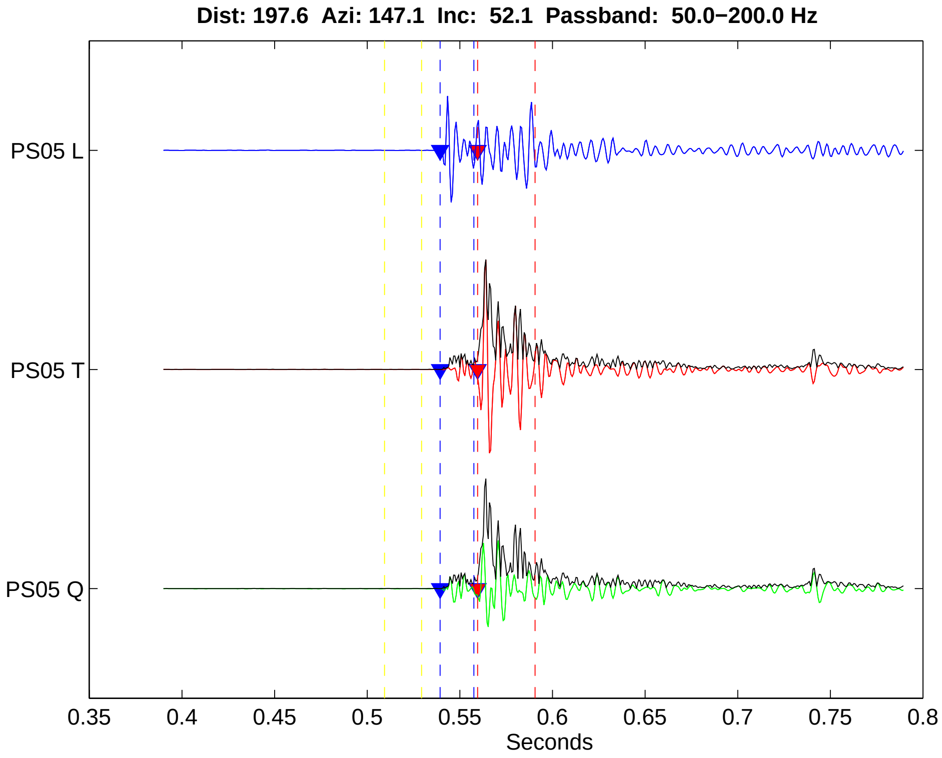

Figure 27. LTQ rotated waveforms of the three-component sensor PS05, filtered in the passband 50-200 Hz. The station is located 198 meters from the estimated location. The amplitude in the TQ plane is shown by the black envelope plotted on top of the T and Q components. See caption of Figure 26 for details.

The observations of the first detonation of the ripple-fired blast at PS09 and PS01 are given in Figures 28 and 29.

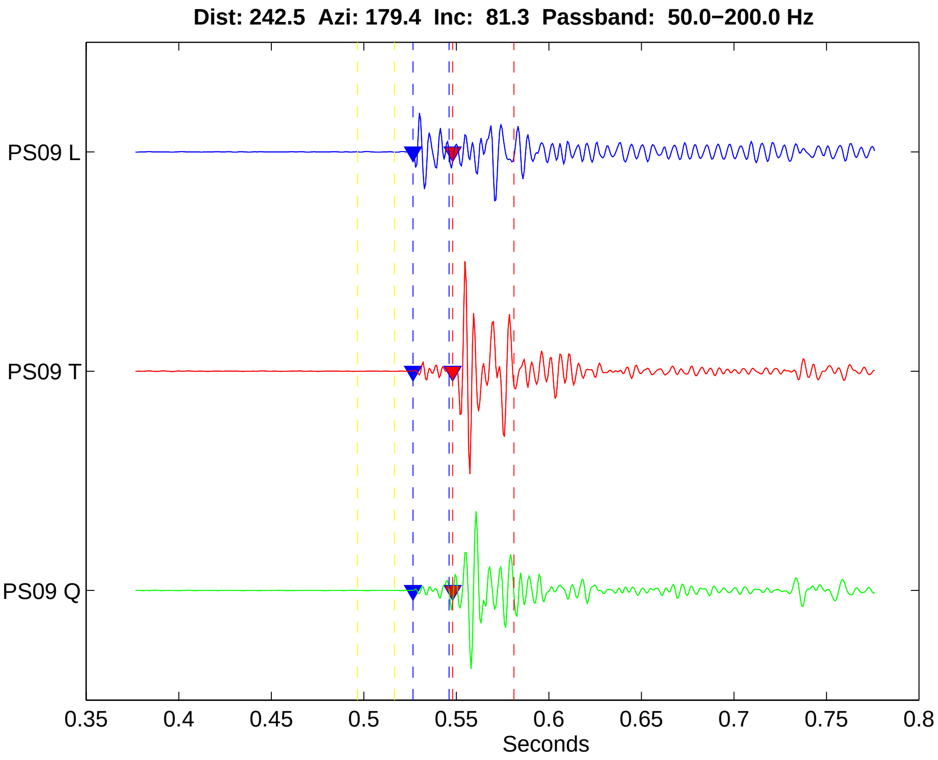

Figure 28. LTQ rotated waveforms of the three-component sensor PS09, filtered in the passband 50-200 Hz. The station is located 243 meters from the estimated location. See caption of Figure 26 for details.

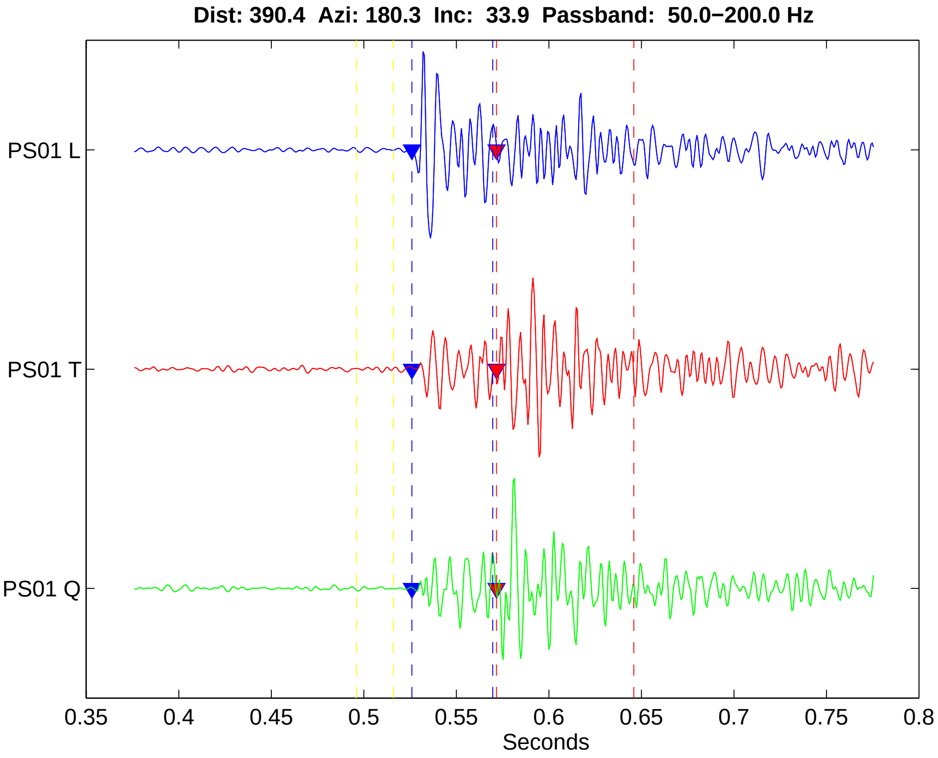

Figure 29. LTQ rotated waveforms of the three-component sensor PS01, filtered in the passband 50-200 Hz. The station is located 390 meters from the estimated location. See caption of Figure 26 for details.

Figure 30 shows the calculated S/P ratios for the different events in the ripple-fired blast in the 80 to 160 Hz frequency band. Only events where the SNR of the P-phase exceeds 2.5 are plotted, and events with S/P ratios exceeding 10 are indicated by triangles. A relatively large variability in S/P ratio can be observed among the different sensors, and also among the different detonations. The later part of the ripple-fired blast is also complicated by double detonations (e.g., no. 11). A similar overview for the 160 to 320 Hz band is shown in Figure 31, and again a large variability in the S/P ratios are observed.

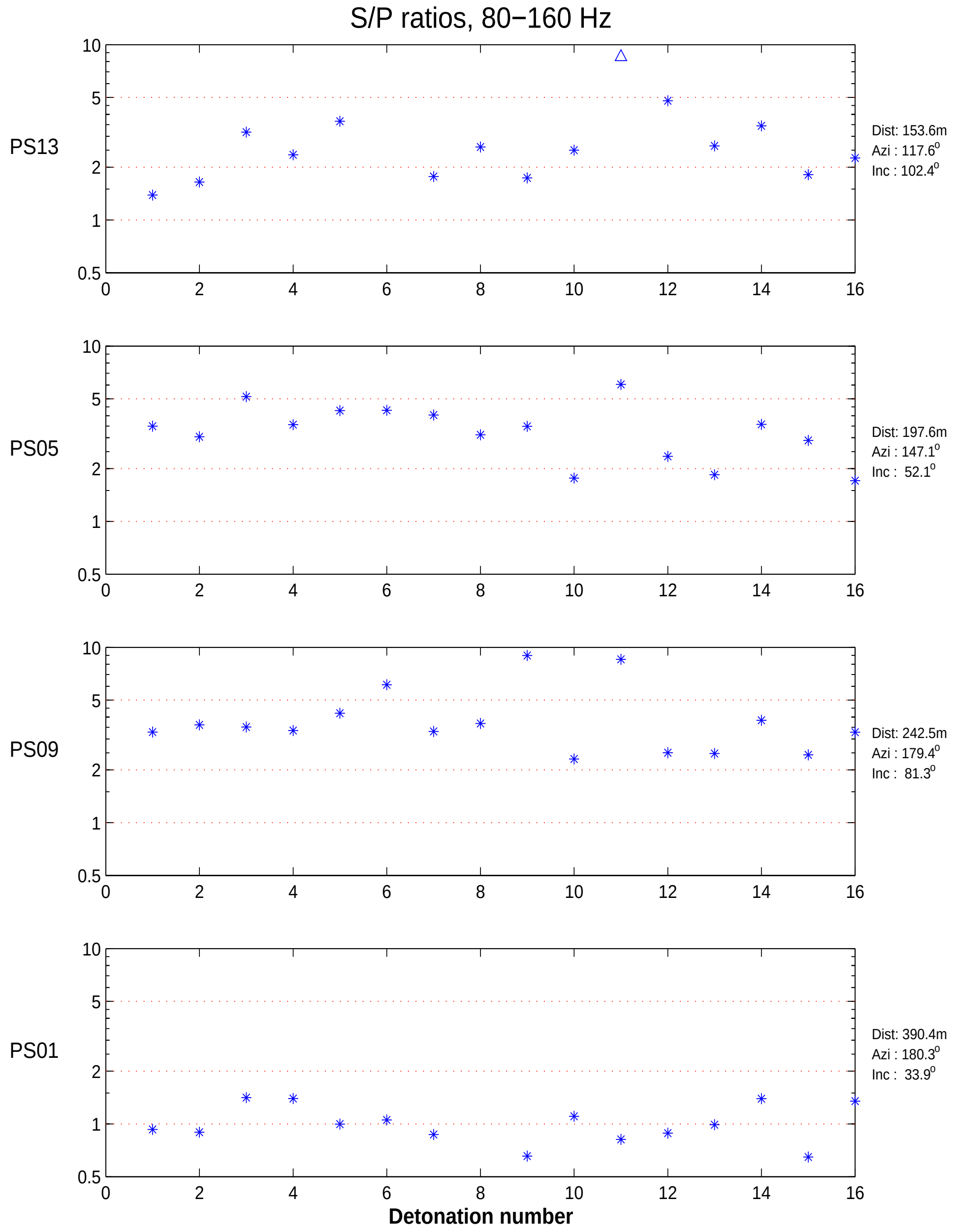

Figure 30. S/P ratios for the different events in the ripple-fired blast in the 80 to 160 Hz frequency band. Only events where the SNR of the P-phase exceeds 2.5 are plotted, and events with S/P ratios exceeding 10 are indicated by triangles. The theoretical distances, azimuths and incidence angles from the estimated location to the three-component sensor are given to the right of each panel.

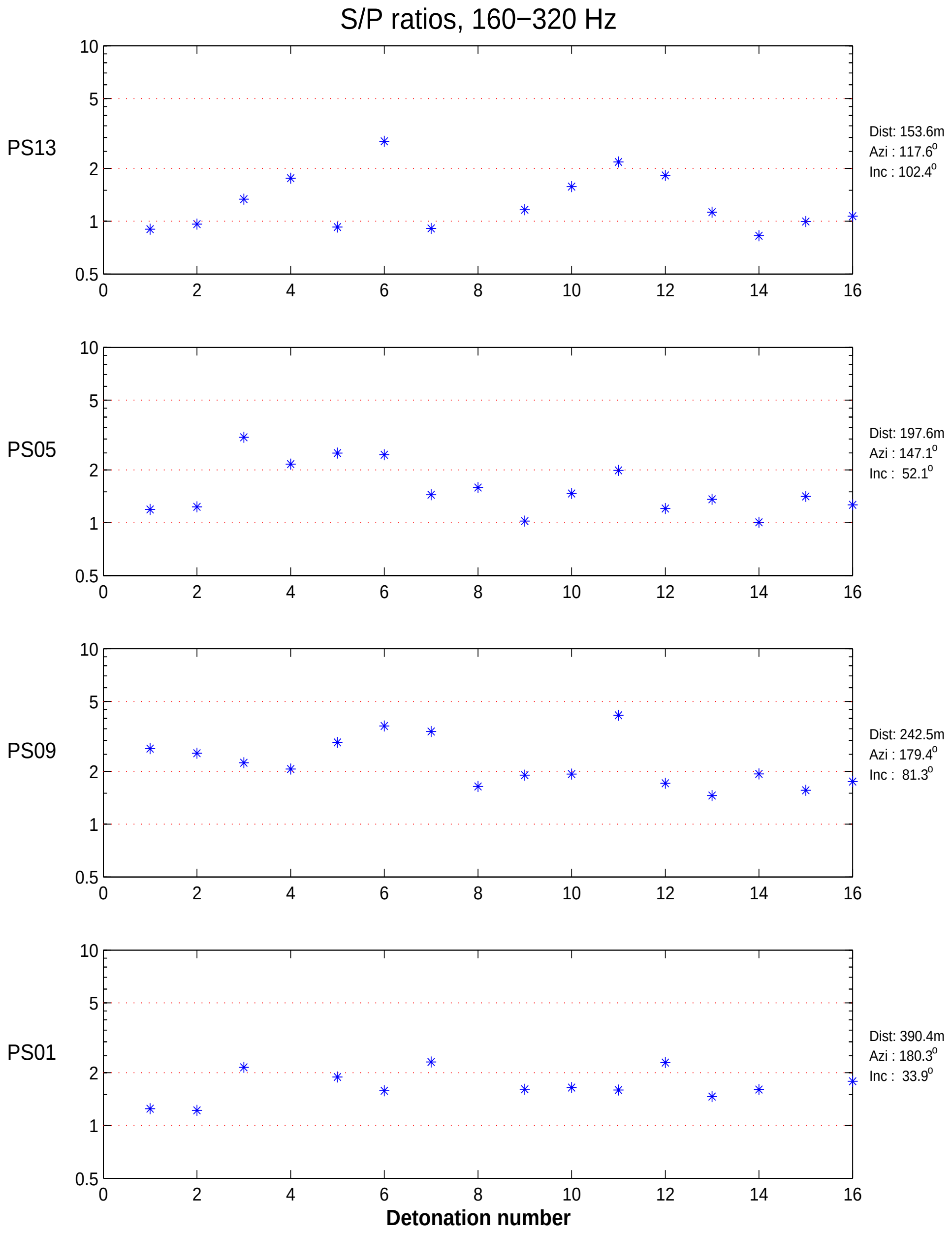

Figure 31. S/P ratios for the different events in the ripple-fired blast in the 160 to 300 Hz frequency band. Only events where the SNR of the P-phase exceeds 2.5 are plotted. The theoretical distances, azimuths and incidence angles from the estimated location to the three-component sensor are given to the right of each panel.

In order to get a better overview of the source contribution to the observed shear-wave energy, we have calculated S/P ratios for both production blasts and rockbursts, using a data set of about 2,000 well-located events with recordings at a minimum of 3 three-component stations. The quality of the automatic processing results (i.e., phase picks, polarization estimates and event location) was checked by visual inspection of the three-component data. Events with erroneous time picks, polarization angles or location estimates were in this way rejected. About 1,300 events remained after the quality control, and for these we measured the maximum P and S amplitudes in a series of 1 octave passbands, given in Table 2.

Again, the P amplitude was taken to be the maximum amplitude on the L-component. The S amplitude was taken to be the maximum of total S-wave amplitude in the orthogonal TQ plane.

The production blasting in the Pyhäsalmi mine takes place between 21:50 and 22:00 local time, so we labelled events occurring within this time interval “the explosion data set”. This data set probably also includes a few rockbursts, but these will not significantly influence the overall statistical characteristics of the explosions. In order to avoid effects like signals from rockfall and interference from previous detonations, we only considered the first detonation of ripple-fired blasts. Events occurring outside the time window 21:45 to 22:05 were denoted the “rockburst data set”.

Figure 32 shows the distribution of S/P ratios for all observations of explosions and rockbursts for three frequency bands, 50-100 Hz, 100-200 Hz and 200-400 Hz. As expected, the explosions have generally lower S/P ratios for all frequency bands, but the difference is far too small to be significant for classification purposes. The maxima for the explosion distributions are all below 2, whereas they are all above 2 for the rockbursts. The rockbursts also have a wider distribution of S/P ratios, which can be explained by the variability of the radiation patterns from the rockburst sources. In addition, the rockbursts are more widely distributed within the mine volume, whereas the explosions only occur in the active parts of the mine.

The observed S/P ratios, for both explosions and rockbursts, do not show any significant dependency on the distance to the events. However, as discussed above, there is a lower distance limit below which the P- and S-phases do not separate sufficiently in time to permit an estimation of the amplitudes. E.g., for the 200-400 Hz passband this lower distance limit is about 50 meters. We have therefore no information in the distance dependency of the S/P ratios within the first tens of meters from the source.

In order to investigate S/P ratios for similar propagation paths within the mine, we have analyzed explosions and rockbursts occurring within a 100x100x100 meter volume, recorded at sensor PS01, at a distance of about 350 meters from the events. The distributions for this subset of the data set are very similar to those shown for the full data set in Figure 32. This indicates that the observed differences in S/P ratios between explosions and rockbursts are due to differences in the source characteristics, and not due to propagation effects along paths in the mine.

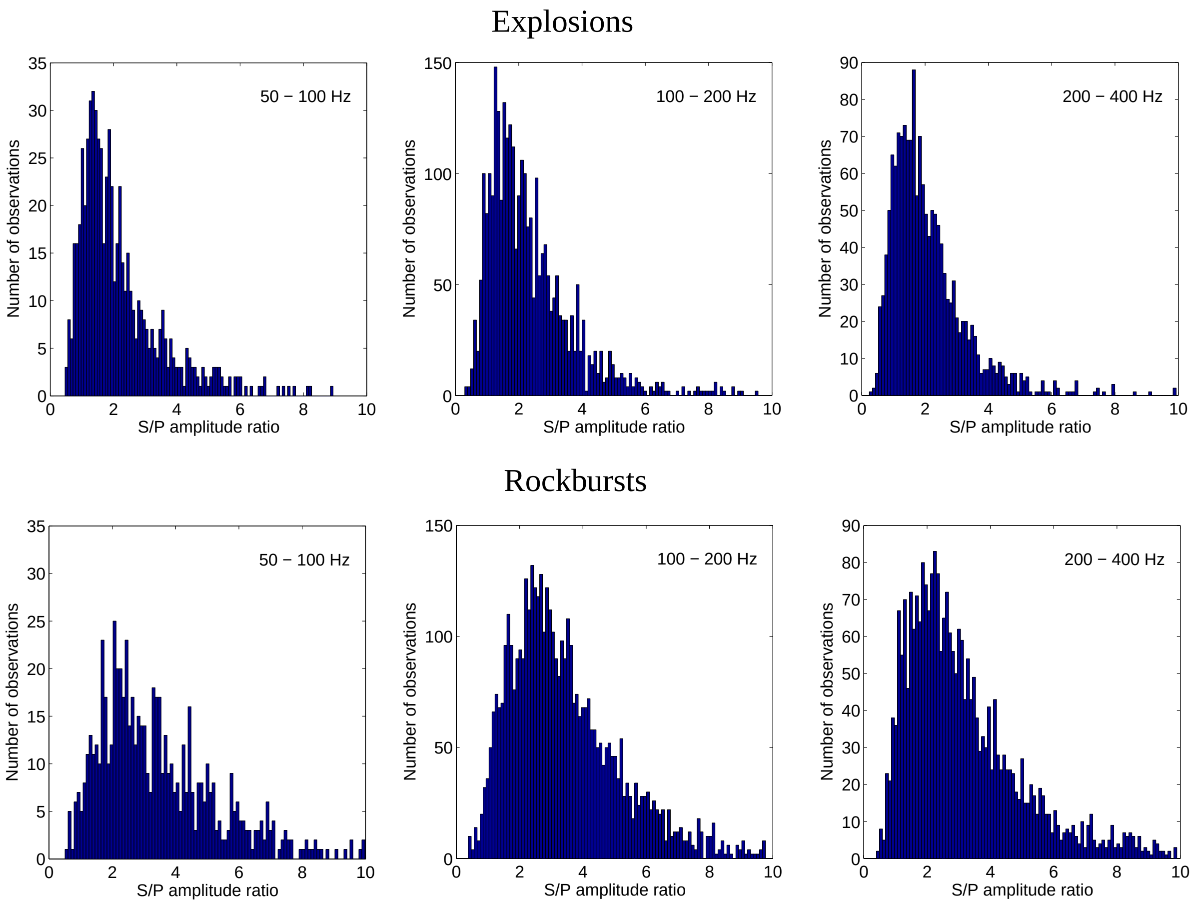

Figure 32. The three upper panels show the distribution of S/P ratios for all observations in the explosion data set for three frequency bands, 50-100 Hz, 100-200 Hz and 200-400 Hz. The three lower panels show the corresponding S/P ratios for the rockbursts.

4 Modeling of In-Mine Data

We have investigated the physical mechanisms that partition seismic energy in the near source region by conducting modeling studies of the Pyhäsalmi mine in Finland. Our efforts centered around three primary activities: 1) validation of our seismic modeling techniques in the presence of underground voids; 2) comparison of observed data from seismic events at the Pyhäsalmi mine with synthetic data generated using a 3-D finite-difference wave propagation code and a 3-D geologic model of the mine; 3) synthetic sensitivity tests to determine the cause and characteristics of shear-energy generation in the near source region. The first two activities served to demonstrate our ability to model seismic wave propagation in a mine environment. The third activity was directed at the generation mechanisms for mode converted shear-energy.

We found that we are able to acceptably model seismic events in and around underground mines at frequencies up to 100 Hz. Synthetic modeling tests demonstrated that significant shear-energy can be generated due to both the geologic and structural heterogeneities within a mine. In fact, mode-converted shear-energy can dominate the compressional energy from a purely explosive source. There is a correlation between shear-energy generation and the distance from a source to a mine heterogeneity. The ratio of shear to compressional energy is about a factor of two larger when the source is located within one wavelength of a mine heterogeneity. Because of its larger impedance contrasts, structural heterogeneity in a mine (e.g., voids) can be a stronger contributor to shear-energy generation than geologic heterogeneity. Numerical simulations suggested that the magnitude of a shear-producing source mechanism (e.g., rockburst, mine collapse) can be as large or larger than that caused by mine heterogeneity.

4.1 Modeling Techniques in the Presence of Underground Voids

The E3D finite-difference code was used for many of the seismic simulations performed for this project (Larsen and Schultz, 1995; Larsen and Grieger, 1998). In summary, this wave propagation code solves the elasto-dynamic formulation of the full wave equation on a staggered grid. As a full physics seismic simulation code, compressional, shear, and mode-converted energy is modeled. Viscoelastic attenuation capabilities are included. The code is computationally robust. It runs on a variety of high performance computing platforms, including massively parallel processors. This makes it possible to simulate large problems. The E3D code is extremely well validated (e.g, Day et al., 2003).

For this project, the E3D code utilized a 3-D geologic model of the Pyhäsalmi mine (see Figure 20). The model parameterized the different geologic and structural components of the mine on a regular grid. The geologic components included the background rock and ore bodies. The structural components included excavated regions such as tunnels, voids, and back filled material produced by mine activity. The 3-D model was 500 m in all three dimensions. The material P-wave and S-wave velocities and the material densities have been discretized onto uniformly spaced grids of two and four meter spacing. The E3D code utilized these discretized grids.

To demonstrate our modeling capabilities, we compared the simulated seismic wavefield from an explosive point source in a homogeneous model (Figure 33) to the wavefield from an explosive point source in the model of the Pyhäsalmi mine (Figure 34). These simulations demonstrate that the simulated wave field is significantly perturbed in the mine model, and that there is significant conversion of compressional energy to shear-energy in the near source region. As expected, the homogeneous model does not produce shear-energy for a simple explosive source.

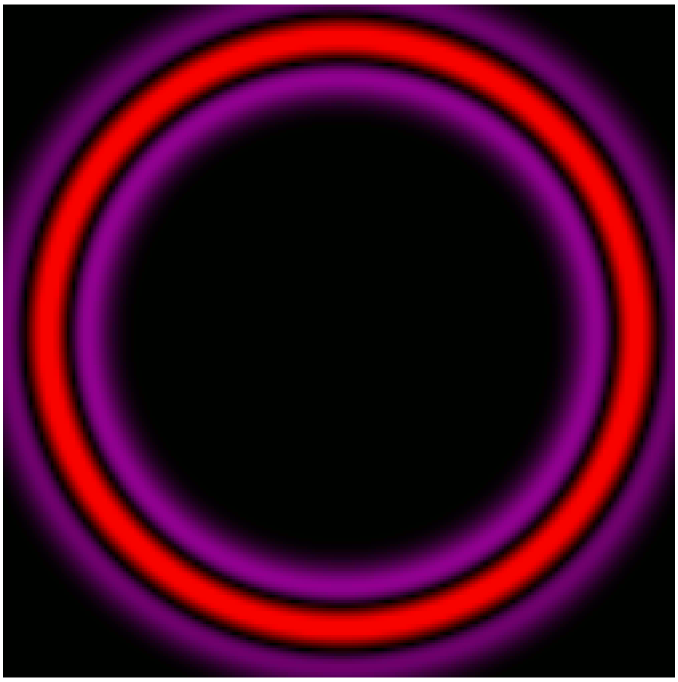

Figure. 33. The image shows a snap shot of the wave propagation in a vertical cross section cutting through the center of the model, using a homogeneous model, at a time of 0.0875 s. The red and blue-red colors represent compressional energy.

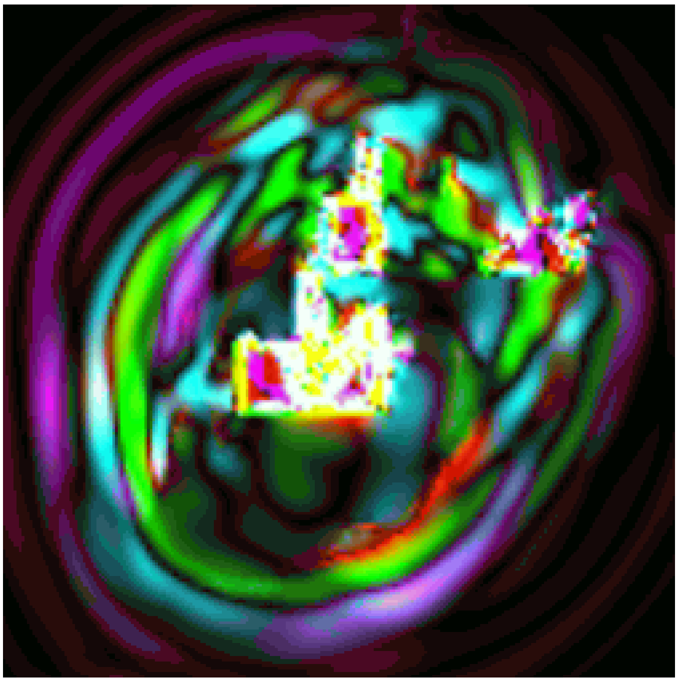

Figure 34. The image shows a snap shot of the wave propagation in the same vertical cross section as in Figure 33, but now calculated using the mine model. Again red and blue-re colors represent compressiona energy, while green and blue-green colors mean shear-energy.

This is further illustrated in Figure 35, where the vertical component of ground velocity and the shear potential for both simulations are shown for a sensor location directly above the source near the top of the model. These simple simulations illustrate how the geologic and structural heterogeneities in an underground mine can produce mode-converted shear-energy.

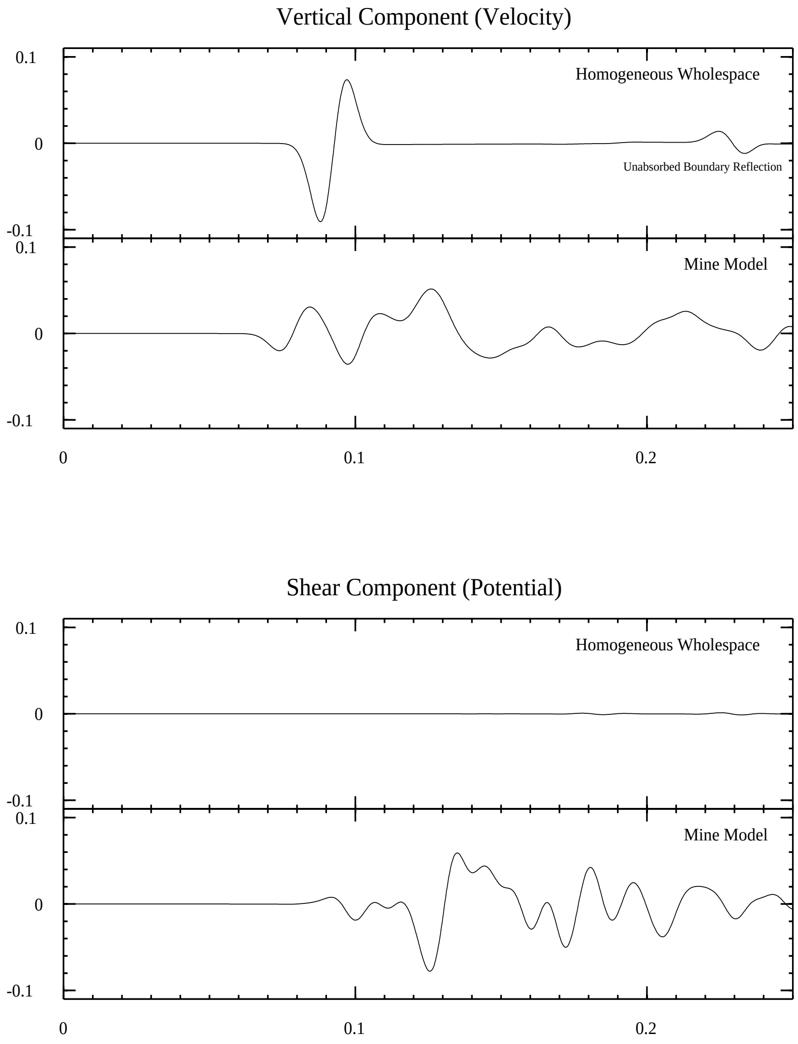

Figure 35. The top panel shows the vertical component of ground velocity for both simulations at a point near the top of the model that is directly above the source. The lower panel shows the corresponding shear potential at the same receiver point.

Of particular interest is the accuracy of our finite-difference simulation technique in the presence of tunnels and other voids (e.g., Larsen and Harris, 1993). Due to numerical constraints, it is often easier and computationally faster to represent the voids as water-filled rather than air-filled material. This is due to the low density and the low compressional velocity of air. To investigate the accuracy of this approximation, we compared the reflections from a real free-surface with the reflection from an approximate free-surface modeled using a water filled region. In addition, an air (albeit air with a density two orders of magnitude larger than its true value) filled region was also used as a boundary condition. Note that the real free-surface boundary condition is known to be accurate, as it has been compared with other techniques, including analytic methods. The geometry of the simulations are shown in Figure 36, where in all cases an explosive source buried in solid rock is used.

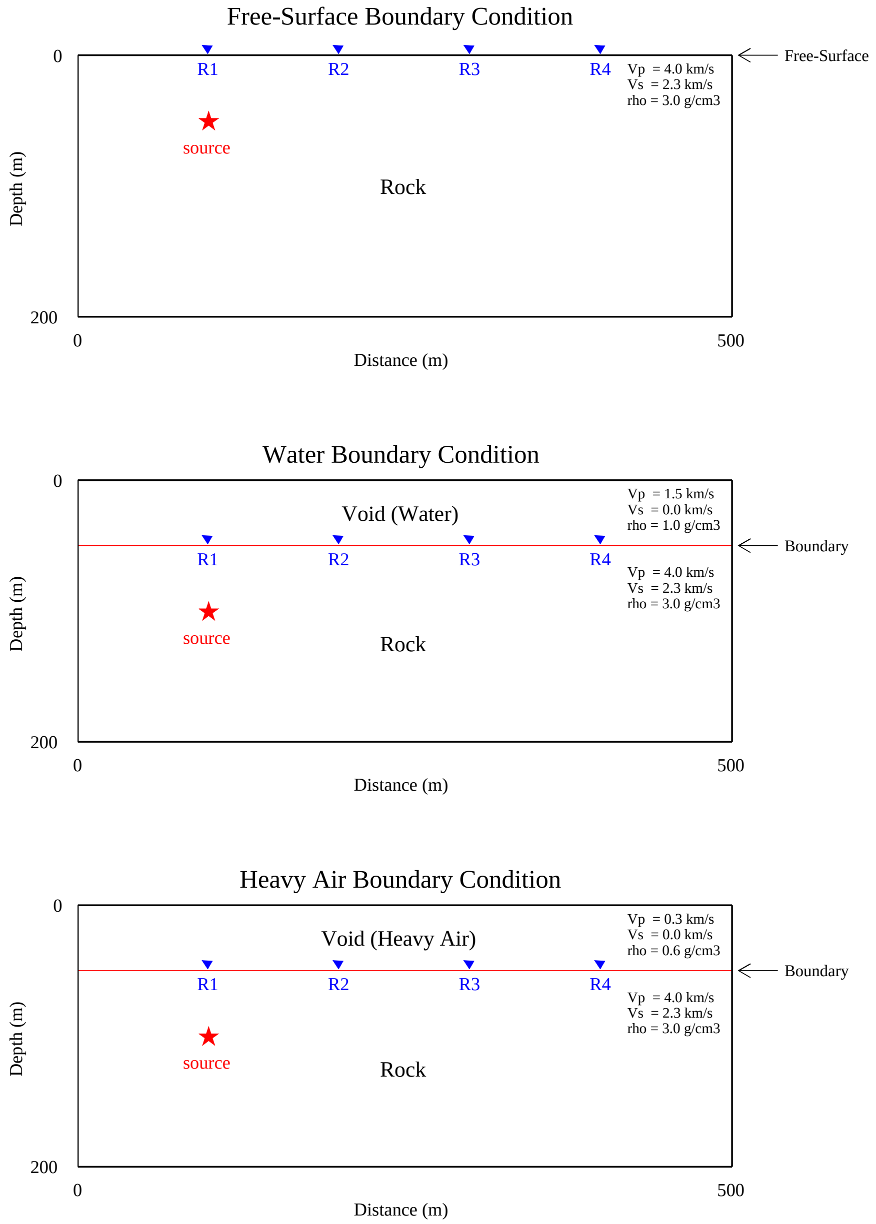

Figure 36. Geometries and parameters used for the investigation of three different boundary conditions. 1 - Free surface. 2 - Rock/Water. 3 - Rock/Heavy air.

The results from the simulations are shown in Figures 37 and 38, where the P- and S-potentials calculated for the different boundary conditions are compared at different sensor locations. As indicated, all three boundary conditions yield very similar results. The arrivals coming later in the records are artificial boundary reflections that are not related to the comparison of interest.

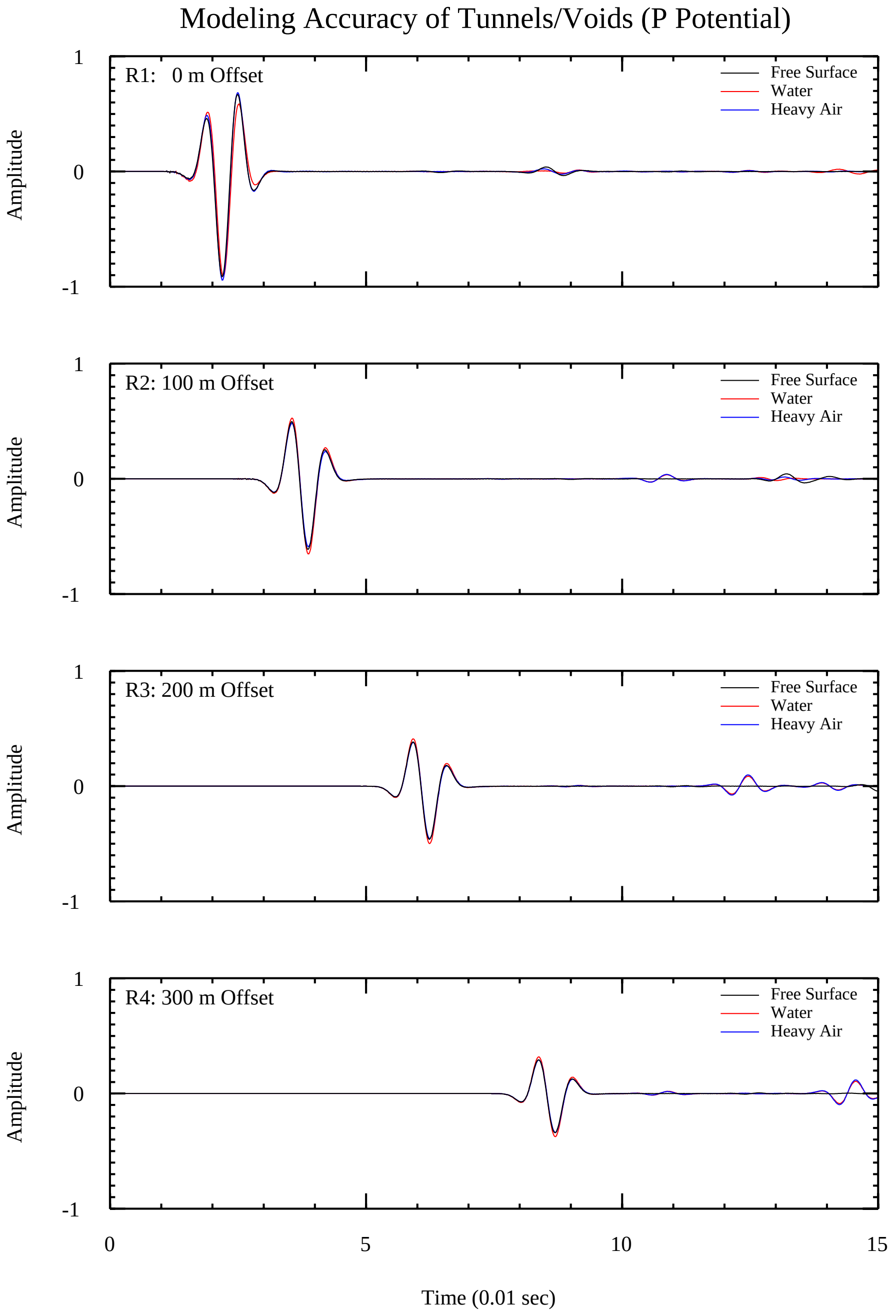

Figure 37. P-potentials for the different boundary conditions described in Figure 36. The arrivals coming later in the records are due to artificial boundary reflections.

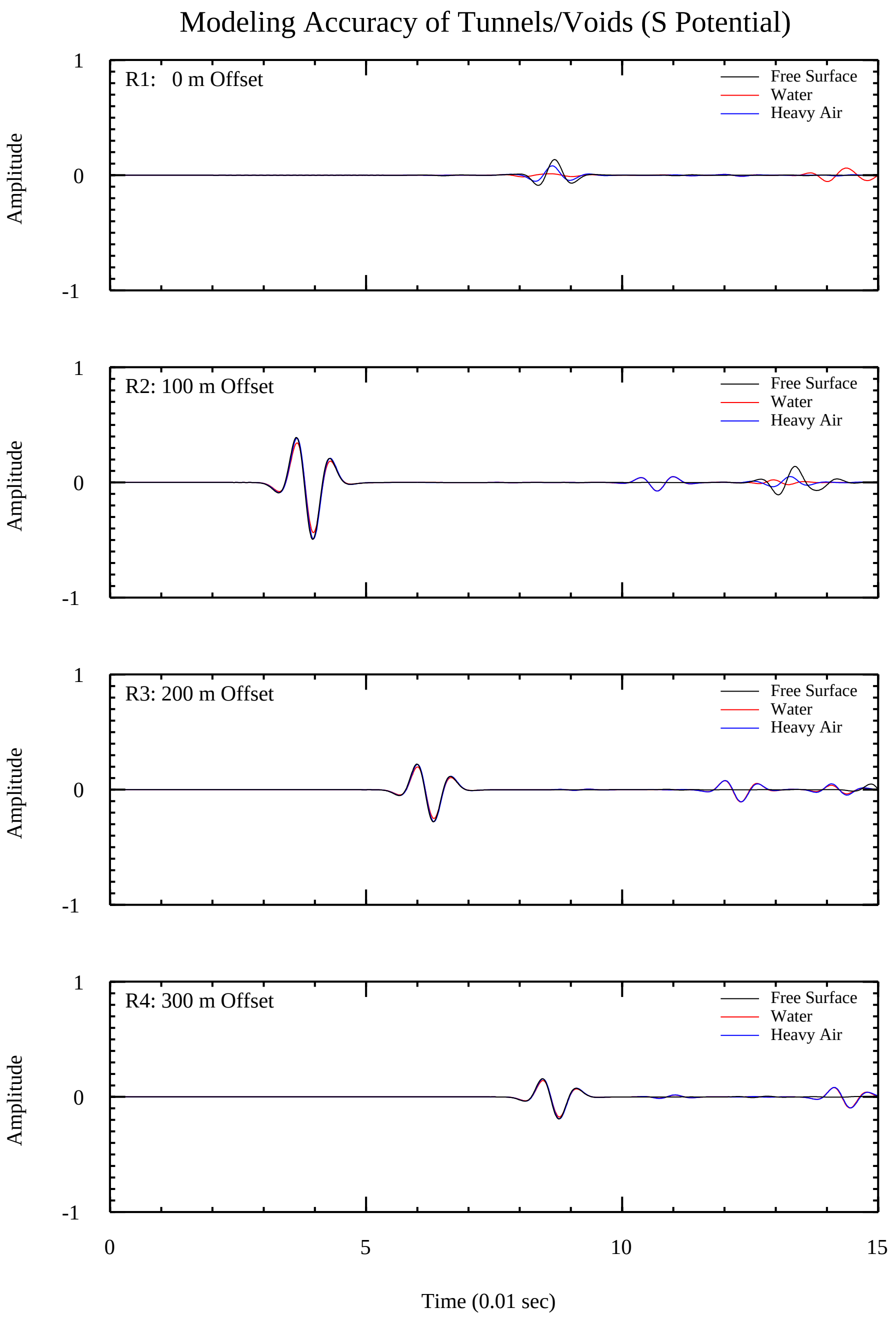

Figure 38. S-potentials for the different boundary conditions described in Figure 36. The arrivals coming later in the records are due to artificial boundary reflections

We performed a more comprehensive test that utilized the actual Pyhäsalmi mine model. In this case, we performed one simulation where the voids were filled with water and a second simulation where the voids were filled with air (with the actual compressional velocity and density for air). The air-filled void simulation was more computationally intensive. The results of this simulation are shown in Figure 39. Shown are the simulated component velocities at several locations within the mine. There is very good waveform agreement between both simulations. This strongly suggests that we can appropriately model excavated regions of a mine at appropriate levels of accuracy.

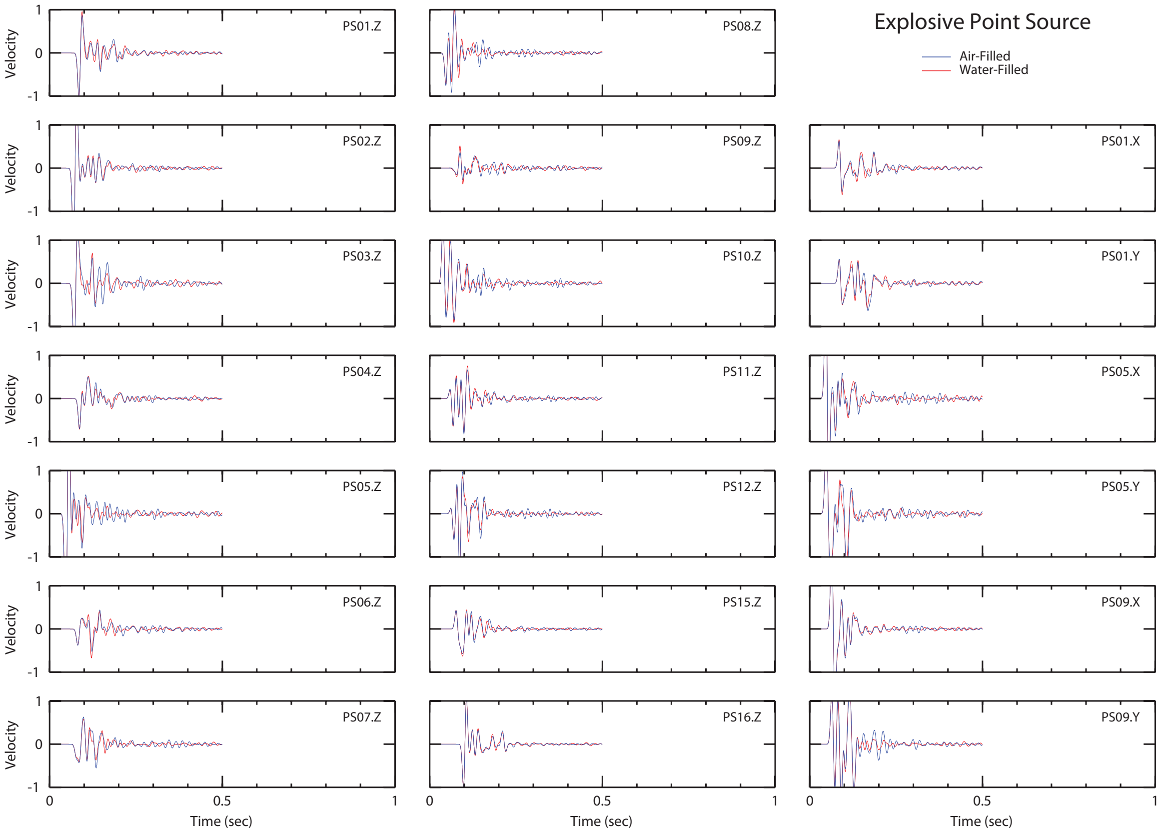

Figure 39. Comparison between waveform modeling using air-filled (blue seismograms) and water-filled voids (red seismograms).

4.2 Waveform Modeling of a Rockburst

On 26 January 2003, a rockburst occurred within the Pyhäsalmi mine. This event was felt and had a magnitude of about 1. It was caused by a pillar collapse and minor damages was observed within the mine. This event occurred along the outer boundary of the mine ore body. In addition, this rockburst was recorded on several instruments within the mine. We modeled this event using the E3D code and the 3-D geologic model of the Pyhäsalmi mine discretized on a 4 meter grid. An explosive source (diagonal moment tensor) was used for the simulation with a frequency range up to 50 Hz. A comparison between the observed and synthetic data is shown in Figure 40. For comparison, the observed data have been low-pass filtered at 50 Hz (4 pole, 2 pass).

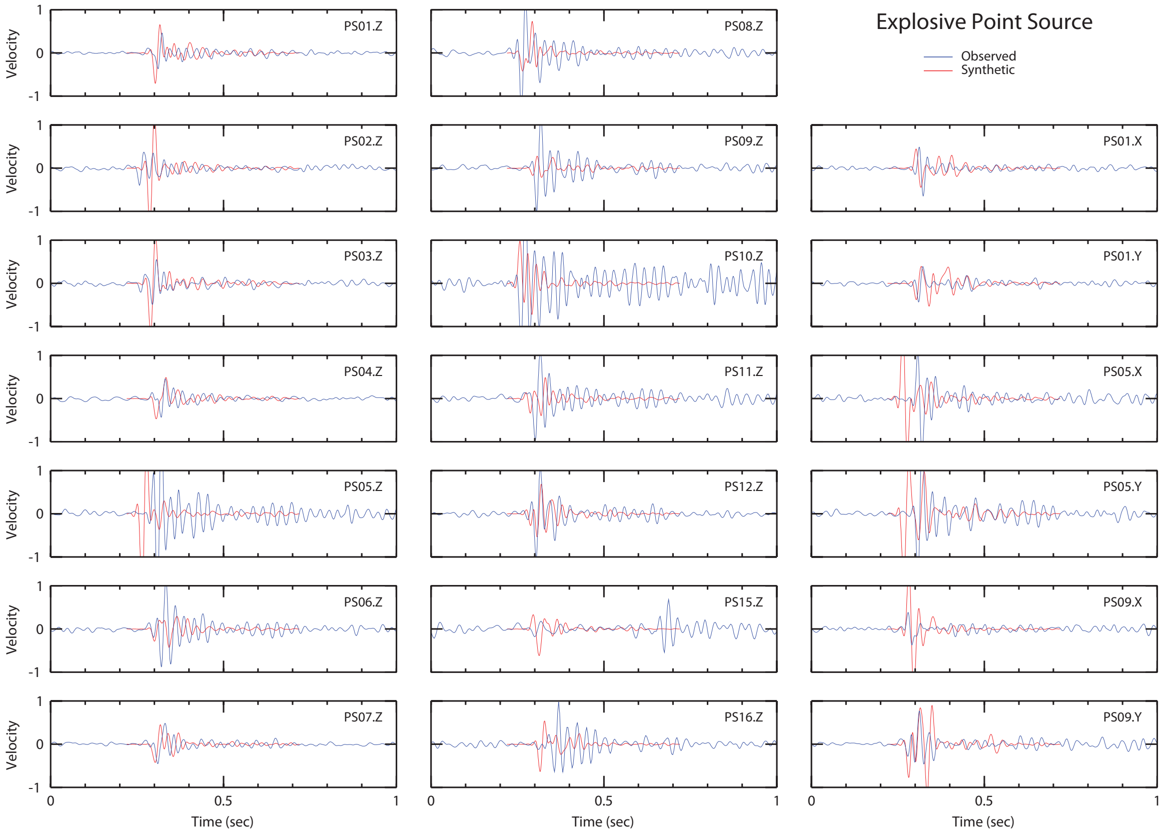

Figure 40. The blue seismograms show in-mine recordings in the Pyhäsalmi mine from a rockburst located along the outer boundary of the mine ore body. The data have been low-pass filtered at 50 hz. Synthetic seismograms from an explosive source calculated in the Pyhäsalmi geologic model (4 m grid) using the E3D code are shown in red.

There is good agreement between the synthetic and observed data. The following observations are made:

- First arrivals are well matched.
- Overall character of early arrivals are well matched.
- Relative amplitudes seem to agree to within a factor of about 2.

In addition, there are some differences between model and observation. For example, more reverberation/coda is seen in the observed data. This may be due to real earth heterogeneity or unmodelled backfill in the mine. Other differences may be due to the simplicity of the source function, inaccuracies in the geologic model, and mislocated receiver (and source) positions. Nonetheless, the agreement between data and simulation is quite good. The synthetic data match the amplitude and overall character of the observed waveforms.

A similar comparison, but one that incorporates seismic frequencies up to 100 Hz is shown in Figure 41. In this case, the two meter discretized mine model is used. The observed data are low-pass filtered at 100 Hz to be consistent with the synthetic waveforms. This simulation was performed using 32 CPU's of a massively parallel processor at Lawrence Livermore National Laboratory. Although the agreement between model and observation is not as good as with the 50 Hz simulation, the comparison is still fair, especially considering the simplicity of the model. In addition to source and site effects, it may be more difficult to accurately characterize the Pyhäsalmi mine at these higher frequencies. Still, these results suggest that we can model real seismic events at the Pyhäsalmi mine, as well as perform synthetic sensitivity tests, at reasonably high levels of confidence.

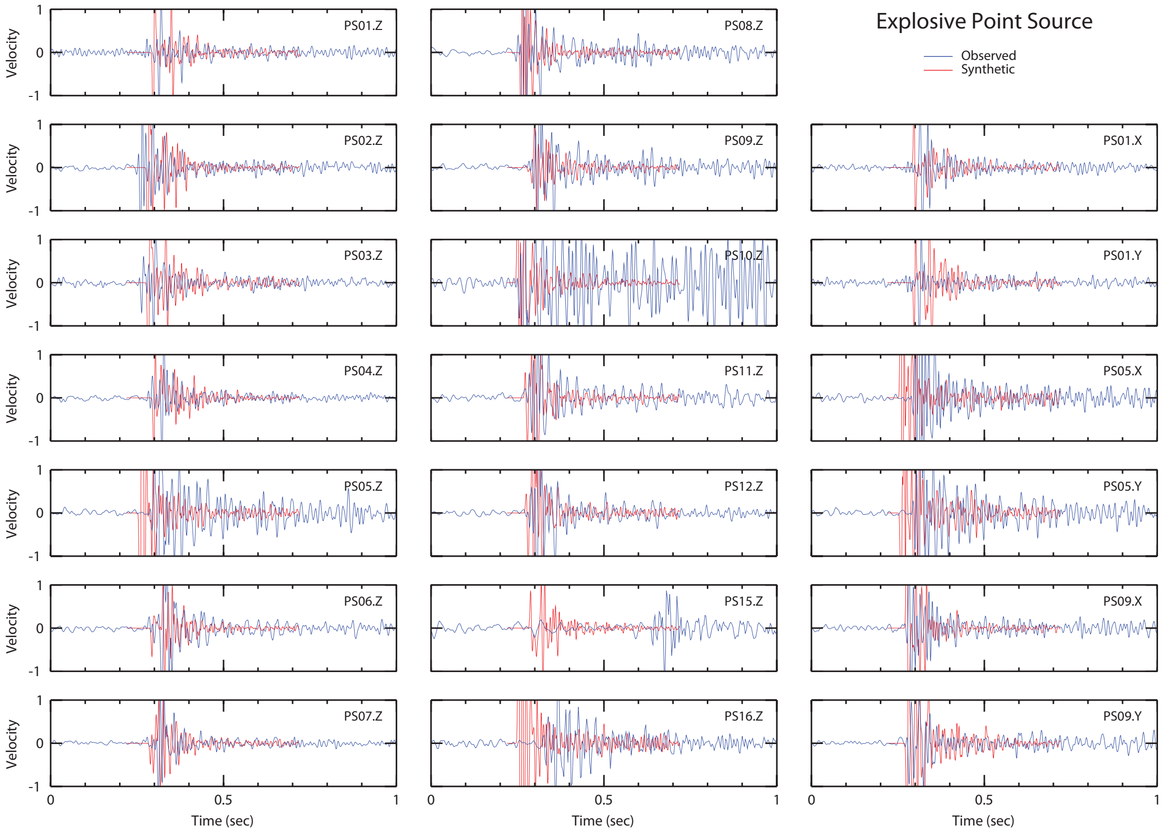

Figure 41. The blue seismograms show in-mine recordings in the Pyhäsalmi mine from the same rockburst as shown in Figure 40, but the data have now been low-pass filtered at 100 hz. Synthetic seismograms from an explosive source calculated in the Pyhäsalmi geologic model (2 m grid) using the E3D code are shown in red.

The 26 January 2003 rockburst event undoubtably has a source function more complex than a simple point explosive source. We performed other simulations where we vary the source type. These simulations use the mine model discretized on a four meter grid and comparisons with the observed data are made at frequencies up to 50 Hz. Results from these simulations using alternate source mechanisms are described in more detail, including figures, in previous quarterly and annual reports. The results are summarized here.

Considering the physics of a rockburst-induced mine collapse, we consider a vertical force and a vertical couple as driving mechanisms. Surprisingly, synthetic data from simulations using these source mechanisms do not fit the observed data better than the simple explosive point source with its diagonal moment tensor. In fact, the explosive source appears to fit the data better than the more complex mechanisms. In addition, we performed simulations where we decompose the source into the 6 components of the moment tensor. Our hope was that we could better understand and match the observed data by determining the particular components necessary to provide a good fit between data and synthetic. However, these simulations did not provide significant additional insight about the nature of the source. Better source characterization may require that we invert the observed data using these simulations as source component descriptors.

Our modeling efforts with the 26 January 2003 rockburst demonstrate that our ability to model seismic wave propagation in the Pyhäsalmi mine is quite good at frequencies up to 50 Hz and acceptable at frequencies up to 100 Hz. This provides confidence in our simulations of real mine events, and perhaps more importantly, confidence in the sensitivity tests we perform to investigate generation mechanisms of shear-energy in underground mines.

4.3 Shear-Waves from Explosions and Other Events in Underground Mines

We performed a variety of sensitivity tests to investigate the cause and characteristics of shear-energy generation in the near source region of an underground mine. In particular, we are interested in: 1) the correlation between source location and mine heterogeneity; 2) the relative influence of different components of a mine (e.g., structural vs geologic); and 3) the influence of different source mechanisms. We utilized the E3D finite-difference wave propagation code and the 3-D geologic model of the Pyhäsalmi mine discretized on a 4 meter grid. This provided simulation accuracies up to about 50 Hz. For some sensitivity tests, we performed 2-D simulations by extracting vertical slices from the 3-D mine model.

We placed an explosive source at three locations within the Pyhäsalmi mine model. One source was located at the boundary of the mine in close proximity to the ore body (in fact, this source was placed at the same location as that of the rockburst event described above). Another source was located near the center of the mine, and the third source was located relatively far from the mine boundary near the edge of our finite-difference numerical grid. The compressional nature of the explosive source (diagonal moment tensor components) means that all shear-energy must be generated by mode converted P energy interacting with either the ore body or the structural components of the mine (e.g., tunnels, excavated regions). We investigate the amplitude and the near-source proximity of generated shear-energy.

Figure 42 shows two synthetic seismic profiles across the 500 m horizontal extent of the mine model when the source is located near the outer boundary of the ore body. The source is located at a distance of 84 meters. The ore body and the structural components of the mine fall in the central parts of the profile, from about 90 to 300 meters. The top profile shows the compressional energy (P potential). The bottom profile shows the shear-energy (S potential). As illustrated, shear-energy is generated almost immediately in the very near source region. The magnitude of this shear-energy is comparable to the compressional energy. Presumably, this near-source shear-energy is caused by mode conversions at the geologic heterogeneity from the ore body.

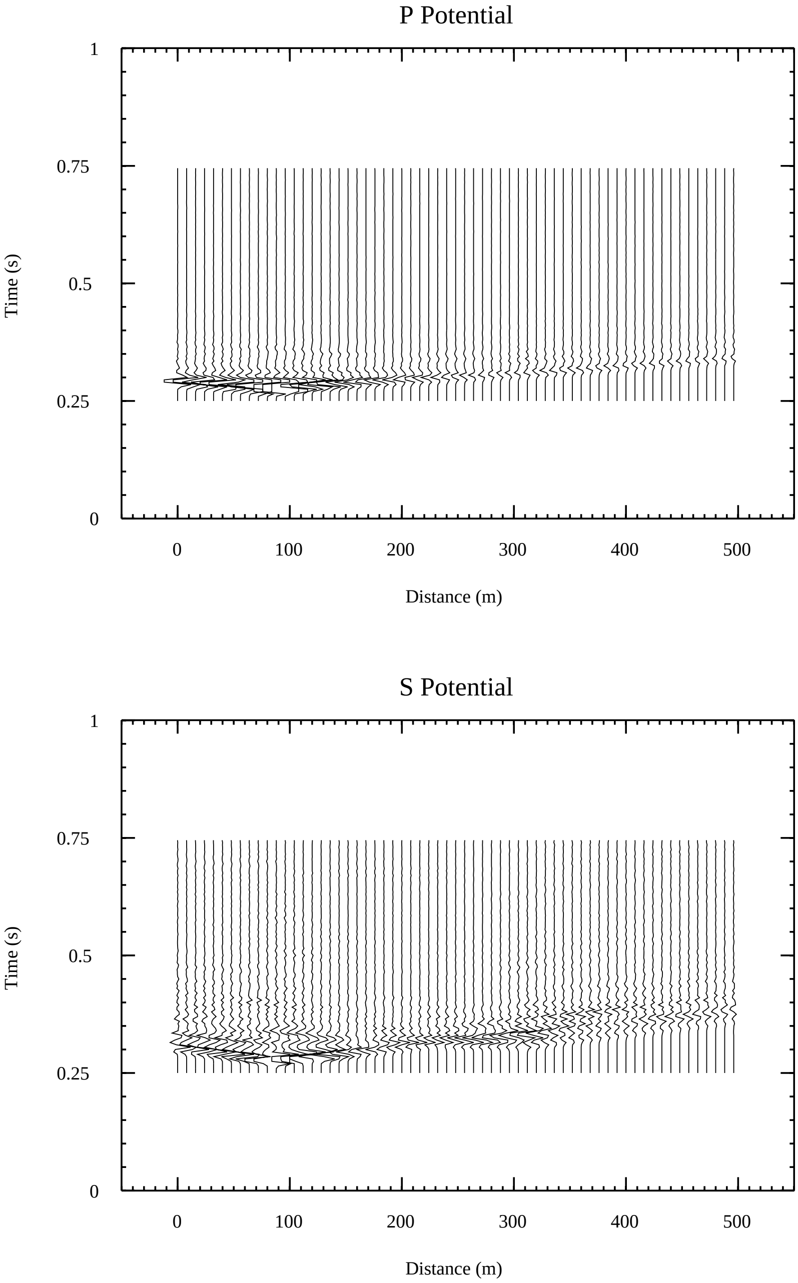

Figure 42. Synthetic seismic profiles of P and S potentials for a 500 m line across the mine model. The source is located at distance of 84 meters, near the outer boundary of the ore body.

Synthetic seismic profiles from the simulation where the source is located in the center of the mine are shown in Figure 43. In this case, the source is located at about 240 meters. As observed in the previous simulation, high amplitude shear-energy is generated in the immediate vicinity of the source. The complexity of the waveforms for both the compressional and shear profiles likely is due to the complexity of the mine (geologic heterogeneity, tunnels, voids).

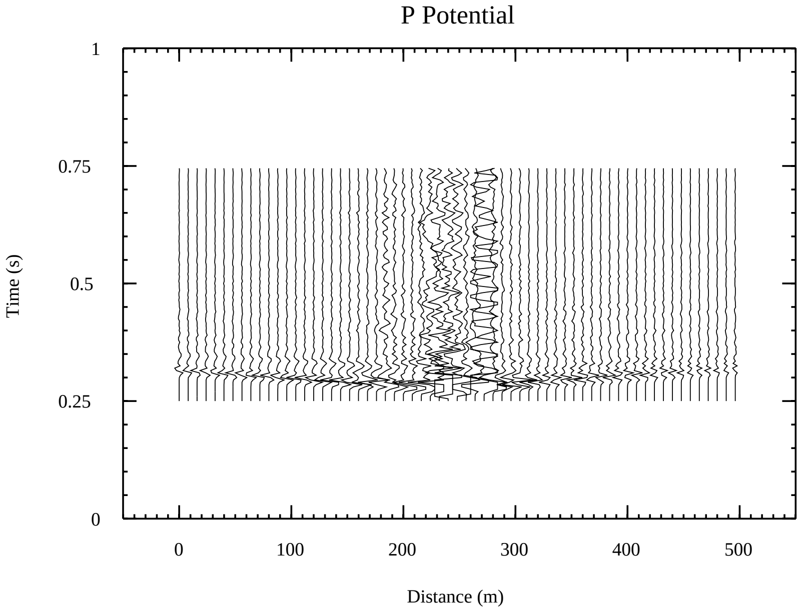

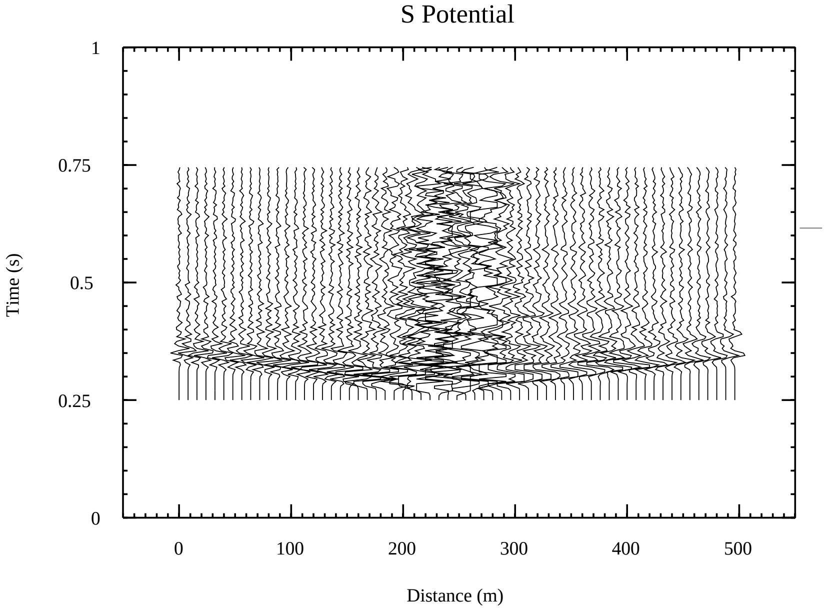

Figure 43. Synthetic seismic profiles of P and S potentials for a 500 m line across the mine model. The source is located at distance of about 240 meters, in the center of the mine.

Figure 44 shows synthetic seismic profiles when the source is located some distance (over 100 meters) from the mine. In this case, little shear-energy is generated. In fact, a good fraction of the shear-energy that is observed may be numerical artifacts caused by unabsorbed reflections from the boundary of the finite-difference grid (the source is relatively close to the grid boundary).

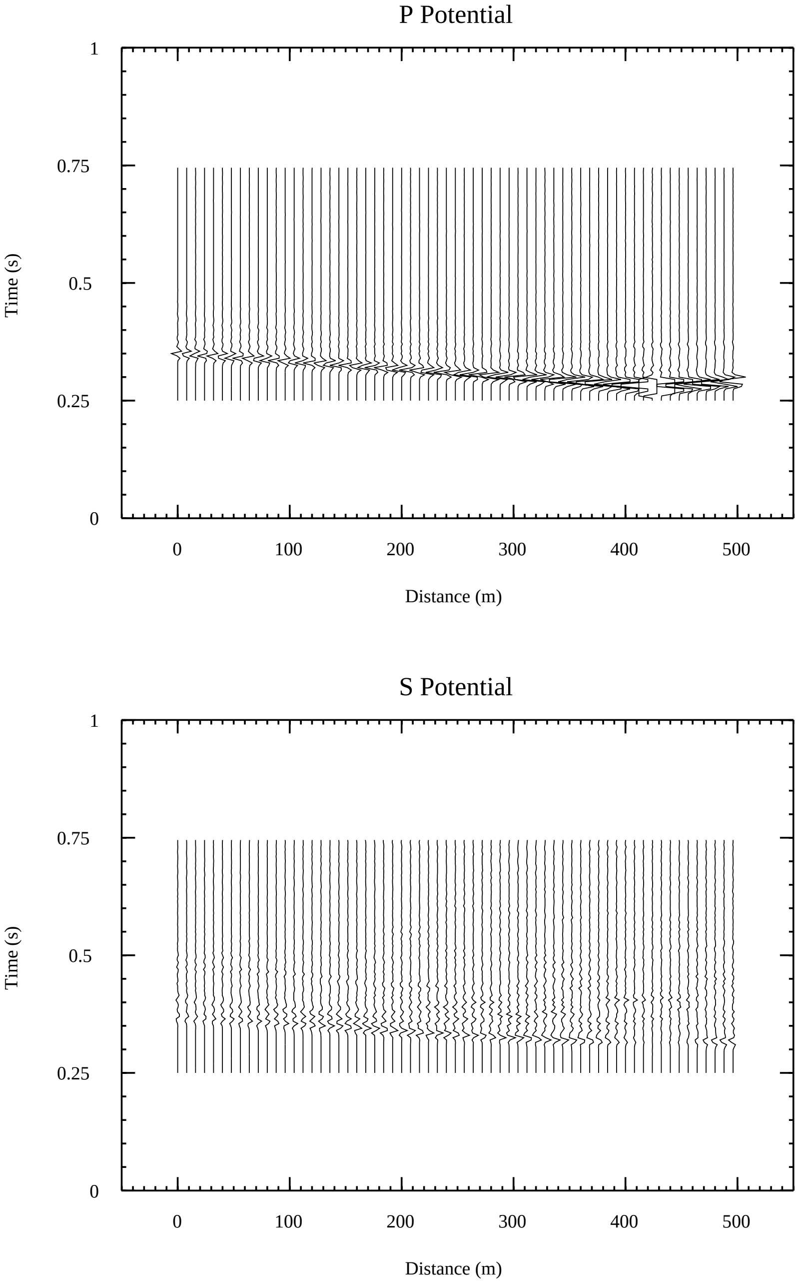

Figure 44. Synthetic seismic profiles of P and S potentials for a 500 m line across the mine model. The source is located some distance (over 100 meters) from the mine.

Figure 45 shows the P and S potential amplitudes and the P/S ratio on the four horizontal and two vertical profiles that extend outward from the source. In this case the source is located at the rockburst location near the boundary of the mine. Shear-energy is generated in the immediate vicinity of the source. Both the P and S potentials fall off with distance due to geometrical spreading. The P/S ratio indicates that most of the shear-energy is generated within about 10 meters from the source, and that the shear-energy is of comparable amplitude to the compressional energy.

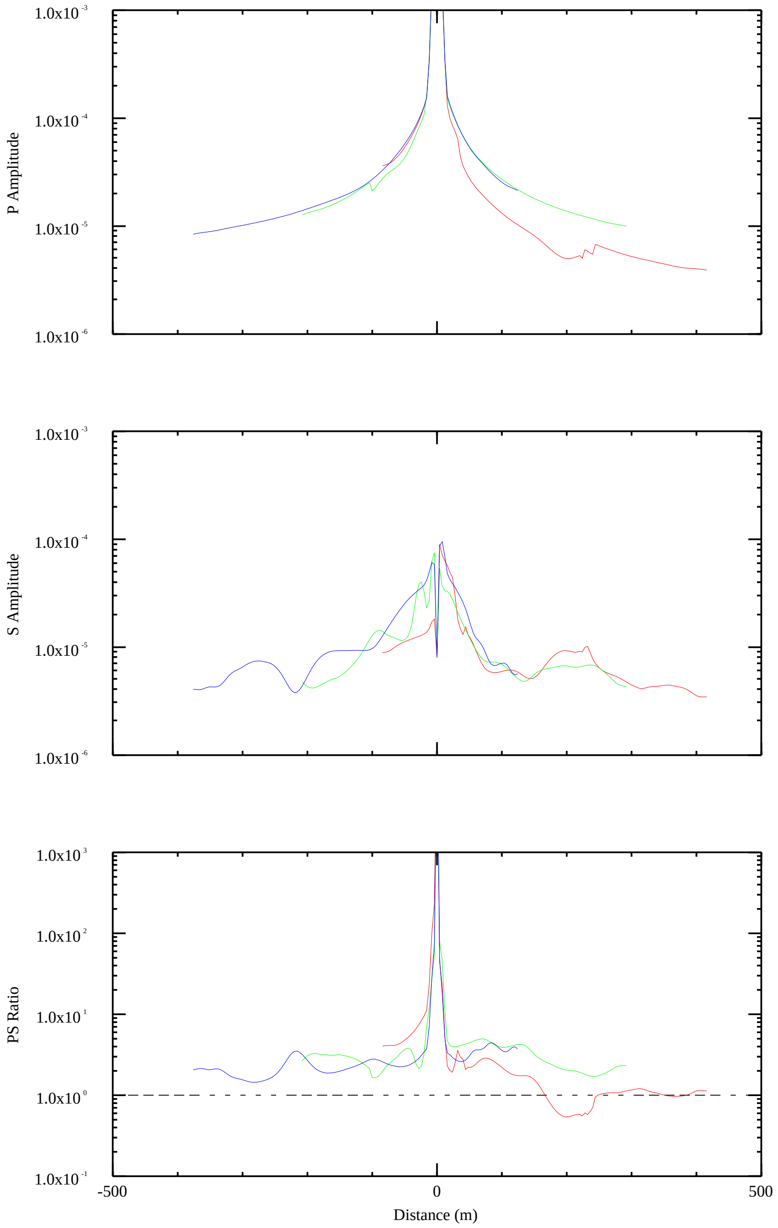

Figure 45. Modelled P amplitude (upper panel), S amplitude (middle panel) and PS ratio for a source located at the rockburst location, near the boundary of the mine. The calculations are made on the four horizontal and two vertical profiles that extend outward from the source.

It is desirable to quantify shear-energy generation as a function of source location within the Pyhäsalmi mine (e.g., Larsen et al., 2005). In particular, we performed over 15,000 2-D finite-difference wave propagation simulations of the mine using an explosive or purely compressional source positioned at different locations within the mine. We examined the generation of shear-energy as a function of source position relative to mine heterogeneities such as ore bodies and excavated regions (voids).

Figure 46 shows a 2-D model cross section through the central portion of the Pyhäsalmi mine. This 2-D representation is extracted from the 3-D discretized model of the mine. The horizontal and vertical dimensions are 500 meters. The model is discretized on a 4 meter finite-difference grid. Blue represents high velocity ore. Black represents excavated portions of the mine. White represents the background geology.

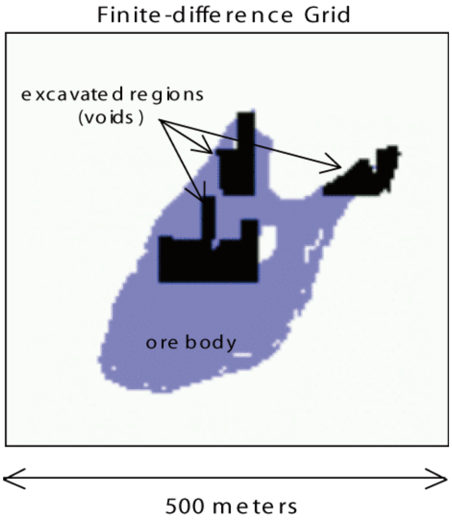

Figure 46. 2-D vertical cross section through the Pyhäsalmi mine.

Several thousand finite-difference wave propagation simulations were performed using this 2-D mine model. A 50 Hz explosive source was used to drive the simulations. An example of one such simulation is shown in Figure 47.

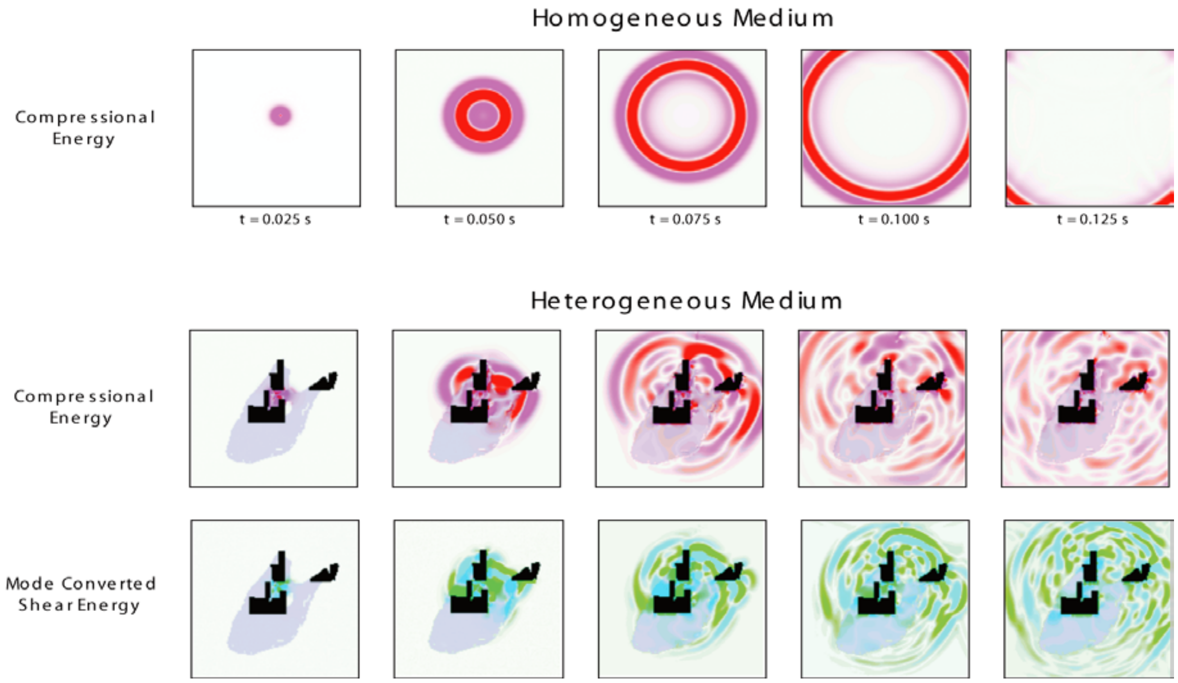

Figure 47. Simulations illustrating generation of shear-energy due to an explosive source near the center of the heterogeneous Pyhäsalmi mine.

In this case, the source was located slightly off from the center of the finite-difference grid. The figure shows the seismic wavefield at multiple time snapshots for a simulation using the heterogeneous 2-D model. For reference, an equivalent simulation was performed in a homogeneous model. Red and red-blue represent compressional energy (P potential) and green and green-blue represent shear-energy (S potential) at various time snapshots. Because the source is purely compressional and there are no heterogeneities in the model, no shear-energy is generated in the homogeneous model. However, significant shear-energy is generated in the real model. This energy is generated as the compressional waves interact with both the excavated regions of the mine (voids) and with the heterogeneity in the mine (ore body). The shear-energy amplitude is comparable to that of the compressional energy.

Figure 48 illustrates the method used here to quantify the generation of shear-energy. For any given simulation and source position, we compute the amount of shear and compressional energy that leaves the near-source region in an “energy flux box” near the edge of the finite-difference grid. Paraxial absorbing boundary conditions are applied to the grid boundaries so little energy is reflected back into the model. More precisely, we compute the maximum shear amplitude and the maximum compressional amplitude at each point along the flux box. We then determine the S/P ratio at each point and average these ratios to estimate the total shear-energy generated within the model. While this method is ad-hoc and does not include issues such as the duration of the compressional- and shear-wavefields, it does provide a first order estimate for how much shear-energy is generated for an explosive source at any given location within the model.

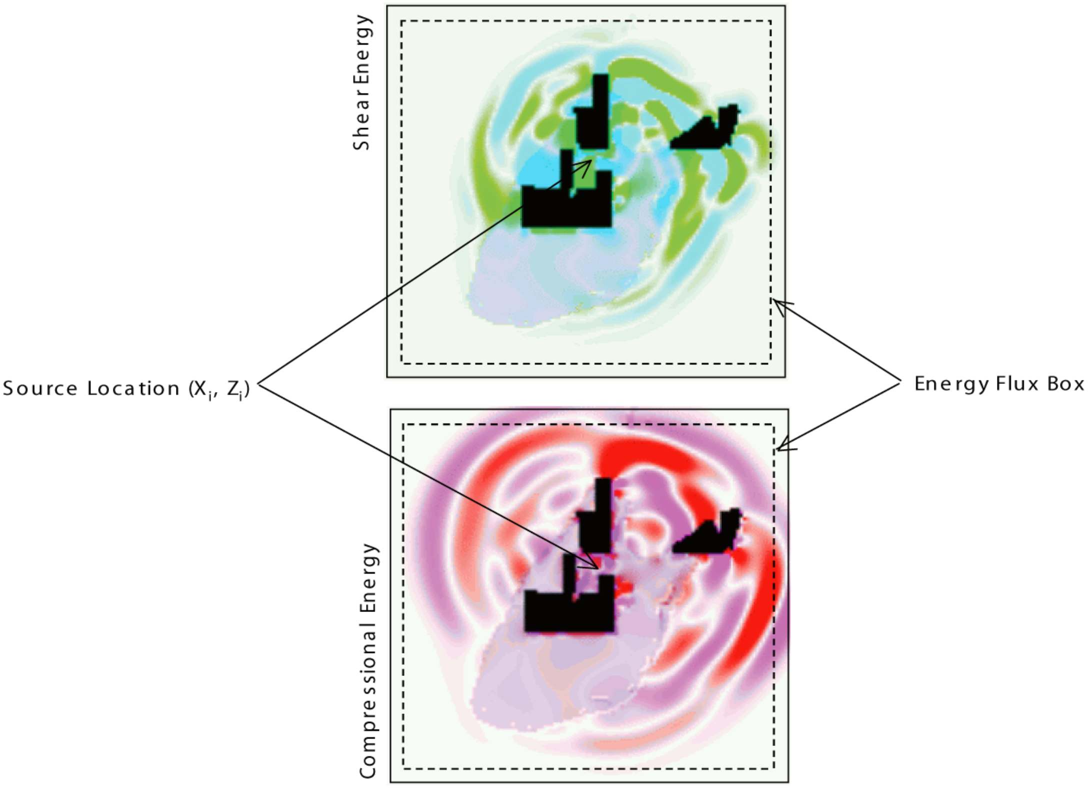

Figure 48. Figure illustrating the method used here to quantify the generation of shear-energy. P and S energy leaving the source region (flux box) can be quantified to determine how much shear-energy is generated for a source at any given location.

We performed 15,376 2-D simulations similar to the one shown in Figures 47 and 48. The source was located at a different grid point for each simulation. The combined result from these simulations is illustrated as the S/P ratio map shown in Figure 49. Each point within this map represents the amount of shear-energy that is generated from a source located at that point using the S/P ratio method described above and in Figure 48. Red indicates source locations that promote the generation of shear-energy. White indicates source locations where minimal shear-energy is generated.

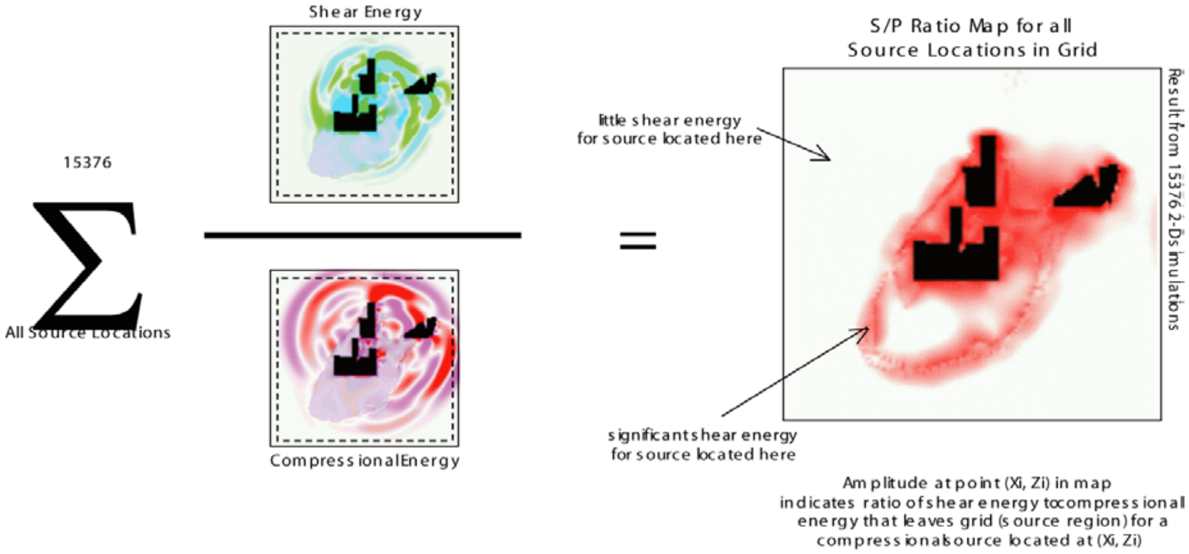

Figure 49. Figure illustrating the method used here to quantify the generation of shear-energy in the Pyhäsalmi mine. Each point within the map to the right represents the amount of shear-energy (S/P ratio) that is generated from an explosive source located at that point.

Figure 49 suggests that shear-energy is more likely to be produced when a source is located near geologic heterogeneity or a structural boundary. In fact, for these simulations, significant shear-energy is most often generated when the source is located 10-20 meters from a natural or engineered interface.

We performed two other sets of 15,376 simulations. In one case, only the excavated or mined-out portions of the mine are included in the 2-D model. In the other case, only the geologic heterogeneities (e.g., ore body) are included in the model. The S/P ratio maps for each simulation set, along with the result for the full mine model, are shown in Figure 50. For better clarity, we also scaled the two new S/P ratio maps and these are shown at the bottom of the figure.

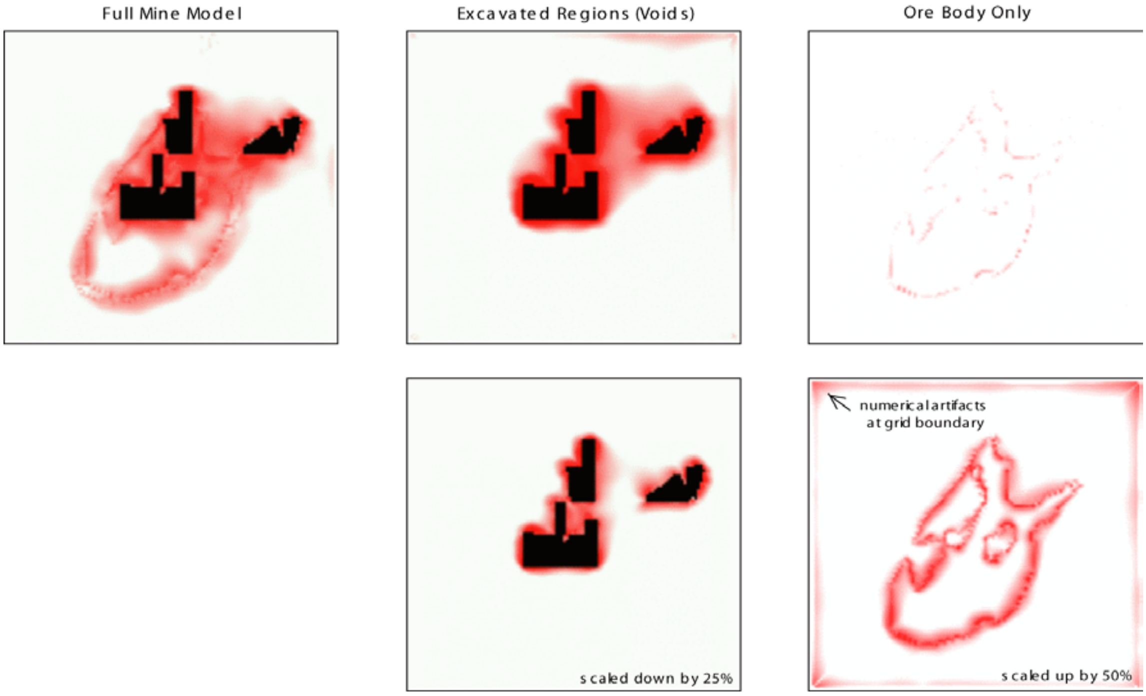

Figure 50. S/P ratio maps for different geological components of the Pyhäsalmi mine. Again, each point within the map to the right map represents the amount of shear-energy (S/P ratio) that is generated from an explosive source located at that point.

The results from Figure 50 are somewhat puzzling. When the ore body is excluded from the model, the S/P ratio map suggests that more shear-energy is generated for sources located near excavated portions of the mine. When the excavated portions of the model are excluded, the S/P ratio map suggests that the shear-energy generated for sources located near the ore boundary is smaller. We have no definitive explanation for this behavior. It may be that shear-energy generation is non-linearly coupled to the presence of both geologic and engineered heterogeneities. It also may be true that the excavated regions are responsible for the bulk of the mode converted shear-energy. This would not be too surprising since there is a stronger impedance contrast with the excavated voids than there is with geologic ore.

These results are further illustrated in Figures 51. We calculated the S/P ratio as a function of source distance from a mine heterogeneity for three cases: 1) the full mine model; 2) a model that includes only the structural components of the mine (tunnels, excavated regions, voids); and 3) a model that includes only the geologic components of the mine (ore body). We calculated the distance to the nearest heterogeneity for each of the 15,376 source positions used in the 2-D finite-difference simulations, and averaged the S/P ratios for all sources within 5 meter distance bins. In the case of the full mine model (Figure 51a), the S/P ratio drops relatively linearly over a source distance of about 50 meters to a mine heterogeneity. In the case of the model that includes only the structural components of the mine, the S/P ratio is more tightly defined by source to heterogeneity distances of about 20 meters. In the case of the model that includes only the geologic components of the mine, there is much less correlation between the S/P ratio and the distance from the source to the nearest heterogeneity.

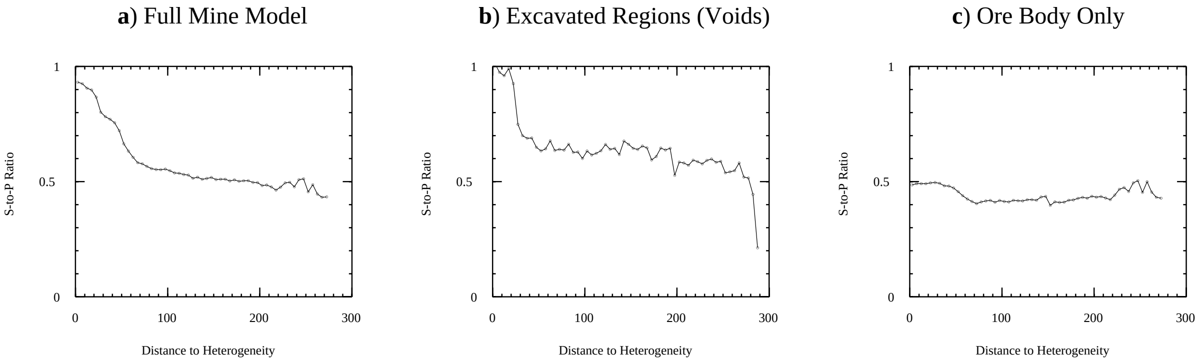

Figure 51. The correlation between shear-energy generation (S/P ratio) and the distance from the source to the nearest heterogeneity, using a) the full mine model; b) a model that includes only the structural components of the mine (tunnels, excavated regions, voids); and c) a model that includes only the geologic components of the mine (ore body)

The results of these modeling exercises suggest that significant shear-energy generation is likely to occur when a source is located within 1-2 seismic wavelengths of a natural or engineered heterogeneity. In addition, large excavated regions of a mine may be more influential for the production of mode converted shear-energy.

Although not specifically shown here, we ran other 2-D simulation suites where we use source mechanisms different than a simple explosive source with diagonal moment tensor components. For example, we performed 15,376 2-D simulations that incorporate a vertical forcing function instead of an explosive source. This source type is different in the sense that the source mechanism itself generates shear-energy. We find that the shear-energy produced by the source can dominate the shear-energy produced by mode conversions at heterogeneous boundaries. This suggests that in addition to structural and geologic heterogeneity, the source mechanism is important for investigations of energy partitioning.

4.4 Summary of Modeling Results

Below is a brief summary of our finite-difference modeling efforts. It includes the modeling of observed data from real seismic events within the Pyhäsalmi mine, as well as sensitivity studies.

Finite-Difference Modeling of Observed Data

3-D Finite-difference simulations were used to model seismic events within the Pyhäsalmi mine. In particular, a January 26, 2003 rockburst were modeled at frequencies of 50 Hz (4 meter grid) and 100 Hz (2 meter grid). We were able to match the characteristics of the observed data at 50 Hz particularly well, and the characteristics of the 100 Hz data reasonably well. These results help validate the 3-D geologic mine model and the reliability of our simulations.

Heterogeneity-Induced Shear-Energy Generation

2-D and 3-D finite-difference simulations were performed to investigate shear-energy generation within the Pyhäsalmi mine. We found that significant shear-energy can be produced due to the geologic and structural heterogeneities within the mine. In fact, mode-converted shear-energy generated from mine heterogeneity can dominate the compressional energy from an explosive source.

Correlation Between Source Location and Shear-Energy Generation

Multiple suites of over 15,000 2-D finite-difference simulations were performed to quantify and investigate the correlation between source location and the magnitude of shear-energy generated within the Pyhäsalmi mine. A strong correlation is observed between the distance of a source from a mine heterogeneity and the magnitude of generated shear-energy. The ratio of shear to compressional energy is about a factor of two larger when the source is located within 1 wavelength from a mine heterogeneity.

Mine Excavation vs Geologic Heterogeneity

Finite-difference simulations at 50 Hz suggest that mine excavation is a significantly stronger contributor to shear-energy generation than geologic heterogeneity.

Shear-Energy Generation from Non-Explosive Sources

Finite-difference simulations reveal that the magnitude of shear-energy generated as part of a shear-producing source mechanism (e.g., rockburst, mine collapse) can be as large or larger than that caused by heterogeneity within the mine.

Finite-Difference Modeling of Voids

Similar synthetic waveforms are produced when the excavated regions within the Pyhäsalmi mine are filled with air or water.

5 Conclusions and Recommendations

In this project we have addressed the problem of energy partitioning at distances ranging from very local to regional for various kinds of seismic sources. On the local and regional scale (20-220 km) we have targeted events from the region offshore Western Norway where we have both natural earthquake activity and frequent occurrence of underwater explosions carried out by the Norwegian Navy.

On the small scale we have focused on analysis of observations from an in-mine network of 16-18 sensors in the Pyhäsalmi mine in central Finland. This analysis has been supplemented with 3-D finite difference wave propagation simulations in a realistic mine model to investigate the physical mechanisms that partition seismic energy in the near source region in and around the underground mine.

The results from modeling and analysis of local and regional data show that mean S/P amplitude ratios for explosions and natural events differ at individual stations and are in general higher for natural events and frequency bands above 3 Hz. However, the distributions of S/P ratios for explosions and natural events overlap in all analyzed frequency bands. Thus, for individual events in our study area, S/P amplitude ratios can only assist the discrimination between an explosion and a natural event.

This observation is supported by synthetic seismograms calculated for simple 1-D models which demonstrate that explosions also generate shear-wave energy if they are fired close to an interface with a strong material contrast (as is the case for most explosions), e.g., free surface, the ocean bottom. The larger difference in S/P ratios between earthquakes and explosions for higher frequencies can be explained by the fact that at low frequencies (larger wavelengths), discontinuities and structural heterogeneities in the explosion source region are stronger generators of converted S energy. The S*-phase, for example, is most efficiently generated whenever an explosion source is located close (within one wavelength) to a strong discontinuity.

Source parameters of mining induced events in the Pyhäsalmi mine follow generally the $M_0 \sim f_c^{-3}$ source scaling relation. Stress drops related to the Brune source model range from about 0.01 to 1.0 MPa. Q estimates from the data vary between about 200 and 800, what is most likely related to the complexity of the mine (voids and tunnels). Analyzing the data with the Multiple Empirical Greens Function (MEGF) approach, attenuation corrections suggest increasing Q with increasing frequency. Energy-to-moment ratios based on the MEGF approach seem constant compared to slightly increasing energy-to-moment ratios based on constant Q models. Comparing our results with results from other studies, covering seismic moments over 11 orders of magnitude, the energy-to-moment ratios seem to increase with increasing magnitudes, i.e. following a modified $M_0 \sim f_c^{-(3+\varepsilon)}$ scaling relation with ε about 0.5.

The Pyhäsalmi explosions have generally lower S/P ratios than the rockbursts for all frequencies, but the difference is far too small to be significant for classification purposes. The maxima for the explosion distributions are all below 2, whereas they are all above 2 for the rockbursts. The rockbursts also have a wider distribution of S/P ratios, which can be explained by the variability of the radiation patterns from the rockburst sources. S/P ratios for explosions and rockbursts located in the same small area of the mine show results very similar to those for the full data set. This indicates that the observed differences in S/P ratios between explosions and rockbursts are due to differences in the source characteristics, and not due to propagation effects along paths in the mine.

3-D Finite-difference simulations were used to model seismic events within the Pyhäsalmi mine. In particular, a January 26, 2003 rockburst was modeled at frequencies of 50 Hz (4 meter grid) and 100 Hz (2 meter grid). We were able to match the characteristics of the observed data at 50 Hz particularly well, and the characteristics of the 100 Hz data reasonably well. These results help validate the 3-D geologic mine model and the reliability of our simulations.

The simulations showed that significant shear-energy can be produced due to the geologic and structural heterogeneities within the mine. In fact, mode-converted shear-energy generated from mine heterogeneity can dominate the compressional energy from an explosive source. A strong correlation is observed between the distance of a source from a mine heterogeneity and the magnitude of generated shear-energy. The ratio of shear to compressional energy is about a factor of two larger when the source is located within one wavelength from a mine heterogeneity. The simulations also suggest that mine excavation is a significantly stronger contributor to shear-energy generation than geologic heterogeneity. However, the simulations reveal that the magnitude of shear-energy generated as part of a shear-producing source mechanism (e.g., rockburst, mine collapse) can be as large or larger than that caused by heterogeneity within the mine.

It is also interesting to notice that analysis and modeling at the local/regional scale provide results that are in accordance with the results obtained from analysis and modeling of in-mine data. Both studies show that strong discontinuities in the source region are efficient generators of P-to-S converted energy, although at very different frequencies for the different scales investigated. The large overlap in the populations of S/P ratios for explosions and natural seismic events at both scales supports this interpretation.

In order to get further insight into the problem of energy partitioning between P- and S-waves from different types of seismic sources, we recommend to conduct further studies that include controlled explosion field experiments with near-source recording. Specifically, fully-coupled, contained explosions could be conducted in proximity to production-style shots, such as in the Pyhäsalmi mine. In this way the physical processes comprising small-scale explosions could be decomposed in order to enable prediction of the observables from larger and more complex explosions. Such observations should be supplemented with numerical simulations of shear wave energy generated directly by nonlinear source effects, as well as by linear propagation effects like scattering from the free interfaces of the mine.

The populations of S/P ratios for explosions and natural seismic events of the data sets analyzed in this study show a large overlap, and therefore cannot be used as a unique discriminant. The possibility of integrating S/P ratios with existing or new measurements should therefore be further investigated, aimed at improving the discrimination potentials.

6 References

Bonner, J.L, B. Stump, M. Leidig, X Yang, R. Zhou, T.S. Kim W.R. Walter, A. Velasco, C. Hayward, D. Baker, C.L. Edwards, S. Harder, H. Hooper, T. Glenn, C. Zeiler, R. Gok, J. Britton and J.F. Lewkowicz (2005). Source phenomenology experiments in Arizona, in P*roceedings of the 27th Seismic Research Review, Ground-based Nuclear Explosion Monitoring Technologies*, LA-UR-05-6407, 519-528.

Day, S., J. Bielak, D. Dreger, A. Fernandez, R. Graves, E. J. Kim, S. Larsen, K. Olsen, A. Pitarka (2003). Validation of 3-D ground motion simulations for the SCEC community velocity model, *SCEC Annual Meeting*, UCRL-JC-155549-ABS, 2003.

Fertig, J. (1984). Shear waves by an explosive point-source: The Earth surface as a generator of converted P-S waves, *Geophysical Prospecting*, 32, 1-17.

Hong, T.-K. and J. Xie (2005). Source array analysis on the composition of regional waves from Balapan explosions in the near-source region, in P*roceedings of the 27th Seismic Research Review, Ground-based Nuclear Explosion Monitoring Technologies*, LA-UR-05-6407, 561-569.

Kanamori, H. and L. Rivera (2004). Static and dynamic scaling relations for earthquakes and their implications for rupture speed and stress drop. *Bull. Seism. Soc. Am.*, Vol. 94, 314-319.

Larsen, S. C., and D. B. Harris (1993). Seismic wave propagation through a low velocity nuclear rubble zone, *Lawrence Livermore National Laboratory Technical Report*, UCRL-ID-115729, 22 p.

Larsen, S. C., and C. A. Schultz (1995). ELAS3D: 2D/3D elastic finite-difference wave propagation code, UCRL-MA-121792, 18 p.

Larsen, S. and J. Grieger, Elastic Modeling Initiative, Part III: 3-D Computational Modeling (1998). *Soc. Expl. Geophys. Confer. Proceed.*, 68, 1803-1806, and *Lawrence Livermore National Laboratory Technical Report* UCRL-JC-130224.

Larsen, S., T. Kvaerna, M. Roth, K. Aastebol, and D. Harris (2005). Simulations of energy partioning from seismic events in underground mines, *SSA Spring meeting and Lawrence Livermore National Laboratory Technical Report* UCRL-ABS-209001.

Ledger, A. (1999). Stress measurement in the 1125 m level, *Outokumpu Mining Pyhäsalmi Mine Oy, Rock Mechanics Technology Ltd. Pyhäsalmi Mine Oy,* Internal report. 7 p.

Müller, G. (1985). The reflectivity method: a tutorial. *J. Geophys.*, 58, 153-174.

Murphy, J.R., B.W. Barker and J. Sultanov (2005). A scaling analysis of frequency dependent energy partitioning for local and regional seismic phases from explosions, in P*roceedings of the 27th Seismic Research Review, Ground-based Nuclear Explosion Monitoring Technologies*, LA-UR-05-6407, 597-605.

Myers, S.C, J. Wagoner, L. Preston, K. Smith and S. Larsen (2005). The effect of realistic geologic heterogeneity on local and regional P/S amplitude ratios based on numerical simulations, in P*roceedings of the 27th Seismic Research Review, Ground-based Nuclear Explosion Monitoring Technologies*, LA-UR-05-6407, 123-132.

Puustjärvi, H., (1999). Pyhäsalmi Modeling Project, Section B. Geology, *Technical Report, Geological Survey of Finland, and Outokumpu Mining Oy*, 66 pp.

Reinecker, J., O. Heidbach, M. Tingay, P. Connolly, and B. Müller (2004). The 2004 release of the World Stress Map (available online at *www.world-stress-map.org*).

Robertsson, J. O. A. and Blanch, J. O. and Symes, W. W. (1994). Viscoelastic finite--difference modeling, *Geophysics*, 59, 1444-1456.

Roth, M. and K. Holliger (2000): The non-geometric $\bar{P}S$ wave in high-resolution seismic data: observations and modelling. *Geophys. J. Int.*, 140, F5-F11.

Stevens, J.L., G.E. Barker, H. Xu, T.J. Bennett, N. Rimer and S.M. Day (2003). The physical basis of Lg generation by explosion sources, in P*roceedings of the 25th Seismic Research Review, Nuclear Explosion Monitoring: Building the Knowledge Base*, LA-UR-03-6029, 456-465.

Toksöz, M.N., S. Chi, Y. Zhang, E. Sze and R. Lu (2005). Characterization of an explosion source in a complex medium by modeling and wavelet domain inversion, in P*roceedings of the 27th Seismic Research Review, Ground-based Nuclear Explosion Monitoring Technologies*, LA-UR-05-6407, 683-692.

Wang, R. (1999). A simple orthonormalization method for stable and efficient computation of Green’s functions. *Bull. Seism. Soc. Am.*, Vol. 89, 733-741.

Xie, X-B, T. Lay and R-S Wu (2005). Near-source energy partitioning for regional waves in 2D and 3D models, contributions of S*-to-Lg and P-to-Lg scattering, in P*roceedings of the 27th Seismic Research Review, Ground-based Nuclear Explosion Monitoring Technologies*, LA-UR-05-6407, 249-258.

Appendix 1

List of Western Norway events: E- explosion, N-Natural event

Number	Date	Origin Time	Latitude	Longitude	Depth (km)	M_C	Type
3048	28.04.1997	21:20:29.3	59.984	4.769	21.3	1.2	N
3060	15.05.1997	16:03:04.0	60.186	5.114	4.1	1.2	N
3095	08.08.1997	17:46:42.8	59.997	5.176	12.1	1.9	N
3096	11.08.1997	09:29:44.4	60.179	4.978	20.7	1.4	N
3099	15.08.1997	12:23:41.9	59.719	5.430	0.1	1.7	N
4335	15.09.1997	15:58:48.4	60.188	5.145	9.0	2.6	N
3168	03.12.1997	23:34:22.3	59.918	5.006	8.8	1.7	N
1038	31.03.1998	10:23:18.4	60.245	5.130	0.0	1.6	E
3248	14.04.1998	20:35:11.7	59.723	4.275	14.4	1.7	N
3253	15.04.1998	19:03:49.8	59.764	4.489	3.6	1.6	N
4337	19.05.1998	07:26:02.0	60.019	4.646	10.0	1.8	N
3320	26.07.1998	22:37:32.2	59.859	5.388	8.6	1.3	N
3390	26.01.1999	12:16:39.1	60.158	5.229	8.9	1.3	N
3447	18.05.1999	23:38:01.4	59.942	5.229	9.7	1.1	N
3466	31.07.1999	05:00:03.9	60.187	5.056	0.1	1.1	N
3467	31.07.1999	15:39:06.6	60.026	5.155	15.0	1.6	N
1073	03.05.2000	12:37:11.5	60.045	4.742	0.0	1.9	E
1074	03.05.2000	13:55:56.8	59.891	4.896	0.0	2.0	E
1075	03.05.2000	14:35:02.0	59.842	4.756	0.0	1.9	E
3572	16.05.2000	10:26:26.6	60.134	5.166	16.0	1.3	N
3607	12.08.2000	14:37:43.6	59.750	5.349	0.0	2.0	N
3610	12.08.2000	14:52:41.4	59.757	5.413	8.5	1.4	N
3611	12.08.2000	14:56:44.7	59.760	5.413	6.0	1.0	N
3612	12.08.2000	14:58:30.3	59.744	5.362	0.1	1.9	N
3615	12.08.2000	15:06:27.0	59.749	5.377	4.7	1.1	N
3616	12.08.2000	15:08:01.5	59.743	5.364	8.3	0.8	N
3617	12.08.2000	15:12:18.9	59.752	5.475	20.5	1.5	N
3618	12.08.2000	15:16:33.2	59.744	5.232	9.2	1.2	N
3619	12.08.2000	15:18:25.8	59.745	5.433	0.1	0.8	N
3620	12.08.2000	16:23:44.3	59.738	5.320	0.5	2.2	N
3621	12.08.2000	18:02:52.9	59.739	5.378	4.1	1.0	N
3623	12.08.2000	19:16:36.3	59.717	5.378	11.9	1.0	N
3624	12.08.2000	20:58:25.9	59.743	5.449	0.0	1.4	N
3625	12.08.2000	21:36:49.3	59.738	5.324	0.1	1.1	N
3626	12.08.2000	22:10:41.0	59.700	5.393	15.0	1.9	N

Number	Date	Origin Time	Latitude	Longitude	Depth (km)	M_C	Type
3627	12.08.2000	22:16:01.0	59.710	5.415	0.3	1.5	N
3628	12.08.2000	22:27:49.7	59.730	5.318	0.0	1.3	N
3629	12.08.2000	23:26:36.1	59.750	5.455	15.0	1.9	N
3630	13.08.2000	05:48:24.9	59.723	5.383	0.0	1.0	N
3631	13.08.2000	13:22:55.4	59.723	5.409	0.0	1.1	N
3638	28.08.2000	08:33:19.6	59.719	5.384	6.9	1.6	N
3644	12.09.2000	17:25:35.7	60.140	5.318	8.2	2.3	N
3667	05.12.2000	05:37:27.6	59.914	5.404	0.1	1.2	N
3673	08.12.2000	17:31:50.0	60.150	4.773	9.4	1.7	N
1107	01.02.2001	10:37:08.9	60.095	4.859	0.0	1.4	E
1108	01.02.2001	10:38:48.2	60.116	4.865	0.0	1.8	E
1110	07.02.2001	13:34:16.7	60.144	4.770	0.0	1.0	E
1111	07.02.2001	13:34:54.4	60.101	4.709	0.0	1.6	E
1112	07.02.2001	14:16:43.8	60.154	4.854	0.0	1.9	E
4342	13.02.2001	11:59:40.6	60.086	4.751	7.0	1.5	N
3749	16.05.2001	17:36:52.6	60.040	4.824	15.0	1.1	N
1139	04.12.2001	08:26:45.7	60.085	4.872	0.0	1.8	E
1140	04.12.2001	08:52:33.0	60.158	4.775	0.0	1.8	E
3880	29.04.2002	09:43:58.5	60.048	4.980	5.1	1.6	N
3882	30.04.2002	16:49:01.5	59.827	5.062	0.0	1.3	N
1160	23.05.2002	20:14:29.6	60.143	4.661	0.0	1.6	E
1170	27.08.2002	15:01:59.8	59.986	4.798	0.0	1.7	E
1171	27.08.2002	15:12:28.6	59.976	4.687	0.0	1.8	E
1172	27.08.2002	15:21:21.1	59.932	4.666	0.0	2.0	E
4343	24.09.2002	10:12:43.8	60.095	4.878	15.0	1.8	N
1190	18.02.2003	10:12:09.9	60.069	4.489	0.0	2.2	E
1191	18.02.2003	10:28:30.1	60.099	4.637	0.0	2.0	E
1192	18.02.2003	11:52:37.8	60.130	4.546	0.0	2.1	E
1194	25.02.2003	09:34:57.7	60.102	4.477	0.0	2.1	E
4077	26.02.2003	12:27:06.5	60.028	4.977	0.1	1.9	E
1203	03.04.2003	10:13:04.0	60.122	4.836	0.0	2.0	E
4198	09.10.2003	01:08:00.9	60.163	5.314	0.1	1.2	N
1238	27.11.2003	13:50:38.2	59.813	4.556	0.0	1.9	E
4246	06.05.2004	20:18:43.2	59.816	5.379	0.0	1.5	N
4248	11.05.2004	00:50:47.7	60.014	5.302	7.0	1.7	N
1251	16.06.2004	12:23:36.1	60.077	4.779	0.0	1.6	E
1252	16.06.2004	13:02:47.2	60.014	4.799	0.0	1.4	E
4286	22.06.2004	20:32:14.3	60.148	4.885	15.0	1.1	N

Appendix 2

Oye, V., H. Bungum and M. Roth (2005). Source parameters and scaling relations for mining-related seismicity within the Pyhäsalmi ore mine, Finland. *Bull. Seism. Soc. Am.*, Vol. 95, pp. 1011-1026.